



POLITECNICO DI TORINO

MASTER THESIS IN NANOTECHNOLOGIES FOR ICTs

---

# Spiral plasmonic lens for new generation photoemitters

---

*Accelerator Technology and Applied Physics Division  
Lawrence Berkeley National Laboratory*

*Author:*  
Kostas Kanellopoulos,  
250247

*Supervisors:*  
Prof. Fabrizio Giorgis  
Prof. Carlo Ricciardi

*Co-Supervisors:*  
Dr. Stefano Cabrini,  
Dr. Daniele Filippetto

Academic Year 2018/2019

# ACKNOWLEDGMENTS

This work could not be possible without the help of a lot people, both from an education and human growth point of view. I want to thank first of all Stefano Cabrini and Daniele Filippetto for the opportunity to live this amazing experience at the Berkeley Lab. I want to thank Prof. Fabrizio Giorgis who agreed to be my supervisors.

I met a lot of people on my way, and I send a huge hug to all of them, with the hope to see all of them again.

I want to say thanks to my parents, Menuccia and Demetrio, to be always supporting me during these years, so as all my relatives, and my cousin Rosabianca.

Finally, I want to say thanks to one of the fundamental parts of my life, my friends.

## ABSTRACT

For decades, metal photocathodes were used in the UV-regime by up-converting the fundamental harmonic of the excitation laser to reach the required energy for single-photon photoemission process. The main problems in this experimental approach are represented by low quantum efficiency at these frequencies, the high power required together with the efficiency for the third harmonic generation. Nowadays, the photocathode technology is paying great attention on a new generation of photoemitters, able to directly exploit the fundamental harmonic, showing the ability to simultaneously enhance and focus the electric field in a sub-wavelength focal spot, leading to non-linear optical processes as the multiphoton photoemission of the 3rd and 4th order. Behind this new technology, the field of plasmonics plays the role of protagonist.

Nanometric emission areas are of fundamental importance in the physics of electron accelerators. Indeed, modern science is asking for even brighter electron beams able to detect matter with incredibly high spatial resolution, reaching at the same time high imaging quality. The requirement of a small emission area is due to the fact that the smaller the electron extraction source is, the higher the brightness will be.

The final aim of this project consists in the development of a new photoemitter with all the characteristics mentioned until now, following the way paved by different researches conducted on this field at the Molecular Foundry, part of the Lawrence Berkeley National Laboratory. In particular, the project will focus on the simulation, fabrication and characterization of a new photoemitter to be implemented for the ultrafast electron diffraction technique.

Ultrafast electron diffraction and microscopy are new promising techniques, able to guarantee high spatial- and temporal-resolved analysis of organic, so as inorganic materials, from amorphous to crystalline samples, where a laser triggers the whole process. Together with the requirement of high-brightness, the electron bunches used as probes in these types of characterizations must show high temporal resolution. This can be obtained with the acceleration of electron pulses up to MeV, where the electron source is positioned inside an RF-gun. One could think to extract electrons from tip-like sources to reach the sub-wavelength dimensions required for the emission area. The main problem of tip-emitters is that it becomes too difficult to control the desired emission for performing ultrafast analysis, since the high electric field will cause field emission at every cycle in addition to the emission caused by the laser triggering.

The main goal of this project, entirely developed at Molecular Foundry, will be to exploit the physics behind the collective oscillations of conduction band electrons in a metal photocathode. If well designed, the structure will be able to enhance and focus the electromagnetic energy arriving from a pulsed laser toward a sub-wavelength region where electron extraction can occur. At the basis of this process, surface plasmon polaritons will represent the main carrier by means of which light can be focused beyond the diffraction limit, making this nanostructure a real plasmonic lens. An archimedean spiral plasmonic lens is designed and optimized through the use of FDTD simulations; the optimized structure is fabricated with the nowadays consolidate template stripping process, which satisfies all the requirements for photoemission applications. All the fabrication steps are performed in a cleanroom class 100, present at the NanoFabrication Division at the Molecular Foundry. Finally, the fabricated plasmonic lens is characterized by means of the cathodoluminescence technique, offering a complex but performant way to detect its plasmonic characteristics.

## Contents

<b>List of Figures</b>	<b>II</b>
<b>1 Toward Ultrafast Electron Diffraction</b>	<b>1</b>
1.1 Introduction . . . . .	1
1.2 HiRES beamline . . . . .	2
1.3 Nanoscale Photocathode for UED . . . . .	3
<b>2 Theoretical Background</b>	<b>6</b>
2.1 Multiphoton Photoemission . . . . .	6
2.2 Plasmonics: a review . . . . .	7
2.2.1 Dielectric function of metals: Plasma model . . . . .	8
2.2.2 Surface Plasmon Polaritons . . . . .	9
2.3 The Archimedean Spiral . . . . .	13
<b>3 Toward a new plasmonic photocathode</b>	<b>16</b>
3.1 PLasmonic Lens Design and Electromagnetic Simulations . . . . .	16
3.1.1 Reflection configuration . . . . .	17
3.1.2 Transmission configuration . . . . .	27
3.1.3 Field Enhancement vs $\theta$ . . . . .	30
<b>4 Nanofabrication</b>	<b>31</b>
4.1 Template stripping method . . . . .	31
4.1.1 Electron beam lithography . . . . .	32
4.1.2 Gold film . . . . .	34
4.1.3 Epoxy resin deposition . . . . .	35
4.1.4 Peel-off process . . . . .	35
4.2 Spiral nanostructure . . . . .	38
<b>5 Cathodoluminescence Spectromicroscopy: the reverse process</b>	<b>41</b>
5.1 Theoretical background . . . . .	41
5.2 Cathodoluminescence Characterization . . . . .	42
5.2.1 CL spectroscopy of the plasmonic interference . . . . .	42
5.2.2 Angle-resolved CL imaging polarimetry . . . . .	46
<b>6 Conclusions</b>	<b>60</b>
6.1 Future perspectives . . . . .	60
<b>A Experimental set-up: DC-gun beamline</b>	<b>I</b>
A.1 Vacuum chamber . . . . .	II
A.2 DC electron gun . . . . .	II
A.3 Laser system . . . . .	III
A.4 Focusing and deflection: the solenoid and the steering magnets . . . . .	III
<b>B Lumerical</b>	<b>VI</b>
B.1 Spiral Script . . . . .	VI

## List of Figures

1	HiRES beamline layout [14]. . . . .	2
2	Schematic of a pump-probed experiment. Here, the result is the temporal evolution of the Bragg peaks, extracted by detecting different diffraction patterns in different times, enabled by the use of electron bunch pulses. . . . .	3
3	Schematic representation of the three-step model [10]. . . . .	6
4	Dispersion curve of a SPP at the metal-dielectric interface. . . . .	12
5	Dispersion relation of SPP at a real metal-dielectric interface [30]. . . . .	13
6	Top: working principle of the spiral plasmonic lens. The central and right figures show how the propagation of the SPPs is affected by the chirality of the circular polarization [20]. Bottom: working principle of the bull's eye. The center of the lens and of the radial polarization must match perfectly to fully exploit it as plasmonic lens [12]. . . . .	14
7	Magnitude of the electric field of the incident source. . . . .	16
8	Geometrical parameters for the archimedean spiral pattern: grating period $p$ , grooves width $w$ , starting radius $r_0$ , grooves depth $d$ and the number of turns $N$ . . . . .	17
9	Reflection set-up for FDTD simulations. . . . .	18
10	Spectrum of the input illumination. . . . .	18
11	Optimization of the grooves depth. . . . .	19
12	Optimization of the grating period. . . . .	19
13	2D distribution of the Field Enhancement along an X-cut. . . . .	20
14	Optimization of the starting radius $r_0$ . . . . .	20
15	Magnitude of the electric field under circular polarization illumination, in a plane perpendicular to the surface . . . . .	21
16	Magnitude of the electric field under circular polarization illumination, in a plane parallel to the surface . . . . .	21
17	Spatial distribution of $E_x$ , $E_z$ and the relative ratio. It is visible how in the center of the structure, for $x = 0$ , the perpendicular component is highly enhanced, while the parallel is practically made null. . . . .	22
18	Superposition of the Field Enhancement and the relative 4-photon photocurrent density enhancement. . . . .	23
19	Spectral distribution of the field enhancement at the center of the spiral for different number of turns. . . . .	23
20	Top: temporal response of the optimized structure, with $d = 90 \text{ nm}$ , $p = 750 \text{ nm}$ , $w = p/2$ and $r_0 = 900 \text{ nm}$ with $N = 5$ turns. In black, the 3-fs at FWHM incident circular polarized laser pulse, in red the response of the lens. Bottom: modulus (top) and phase (bottom) of the transfer function, computed by Fourier transform of the temporal response. The modulus of $T(\omega)$ coincides with the frequency-dependent field enhancement. . . . .	24
21	Temporal FWHM of the intensity (left) and of the photocurrent density (right) at the center of the spiral. . . . .	25
22	Peak field enhancement (top) and photocurrent density $J_4$ (bottom) at the spiral center as a function of the incident pulse duration. . . . .	26
23	Transmission set-up for the FDTD simulations . . . . .	27
24	Optimization of the grating period. . . . .	28
25	Optimization of the grooves depth. . . . .	28

26	Magnitude of the electric field in a plane perpendicular to the surface (left) and parallel to the surface (right), for the optimized spiral plasmonic lens for $\lambda_{exc} = 1030 \text{ nm}$ . . . . .	29
27	Top: temporal response of the spiral in transmission. Bottom: modulus of the transfer function $ T(\omega) $ , i.e. the field enhancement (up) and phase of $T(\omega)$ (down). . . . .	29
28	Spectral distribution of the field enhancement as a function of the tilting angle $\theta$ . . . . .	30
29	Schematic workflow of the Template Stripping process [12]. 1) Deposition of the resist (HSQ, 6%). 2) Exposition with EBL and development of the resist. 3) Deposition of Au with electron evaporation. 4) Deposition of the epoxy resin and of the new support, followed by the curing process of the resin. 5) Peel-off to detouch the new support and the Au film from the template. . . . .	32
30	KLayout pattern for the plasmonic lens mask. . . . .	33
31	HSQ template made with EBL process. The images are taken with SEM system, exploiting the in-lens mode, enabling the detection of secondary electrons of type SE1. These electrons are emitted from the first layer of the surface, due to the interaction of the primary e-beam with the sample. Therefore, they contains important information about the surface of the template, enhanced by the use of low energy primary electron (3 kV in this case). . . . .	34
32	Gold film evaporated onto the template. . . . .	34
33	Cross section of the final structure. The deposition is performed here by hand. On top the gold film; in the middle the epoxy resin layer with a measured thickness of $45 \mu\text{m}$ ; on the bottom the new support made of prime silicon. . . . .	36
34	Cross section of the sandwich structure, with the deposition performed through the hydraulic press. The final thickness results to be close to $10 \mu\text{m}$ . . . . .	36
35	SEM image of the interface between the gold film and the cured epoxy. The deposition of the resin performed manually (top) shows less adhesion at this interface than the deposition performed with the press (bottom). . . . .	37
36	Template and gold film after the peel-off process. . . . .	38
37	Final structure after the whole process fabrication. . . . .	39
38	Depth profile of the spiral structure after the peel-off process. . . . .	39
39	3D depth profile of the final spiral structure. . . . .	40
40	Schematic CL set-up, exploiting the SEM system. . . . .	42
41	Instrument response of the CCD. The blue line is the response processed with MATLAB software. The red line is the corresponding fitting, made to avoid the introduction of spurious peaks in the final spatially averaged CL spectrum. . . . .	43
42	Corrected data for the spatially averaged CL emission spectrum, relative to region within $65 \text{ nm}$ of the central plateau of the spiral plasmonic lens. . . . .	43
43	CL spatial maps of the lens. The maps are obtained from the spectromicroscopy dataset by intergrating over Gaussian wavelength bands with $2\sigma = 10 \text{ nm}$ . Each map is labeled with its corresponding center wavelength. . . . .	45
44	CL spatial map for $\lambda = 800 \text{ nm}$ . The map shows an almost cylindrical spatial profile of the emission, with the intensity at the center comparable with the emission concentric rings. This can be attributed to the small role played by the resonances in this kind of plasmonic lens. . . . .	45
45	CL spectrum relative to the pixel labeled by the orange point. A mask is applied on the dataset in order to compute the average spectrum with respect the region indicated by the point. . . . .	46
46	Schematic plot of the far field CL set-up [12]. To perform CL imaging polarimetry, the integration of rotating-plate polarimeter in the detection path is required. . . . .	47

47	CL imaging polarimetry set-up [36]. The intergation of a QWP and a linear polarizer is shown. In the current experimental set-up, the sample is tilted of $26^\circ$ . The bandpass filter centered at $800\text{ nm}$ is not depicted here. . . . .	48
48	Left: far field CL emission with linear polarizer at $0^\circ$ . Right: far field CL emission with linear polarizer at $90^\circ$ . The orthogonality is visible looking at the shape of the CL emission. . . . .	49
49	Left: far field CL emission with linear polarizer at $45^\circ$ . Right: far field CL emission with linear polarizer at $135^\circ$ . . . . .	50
50	Schematic image of the detection of circularly polarized CL emission. . . . .	51
51	Left: far field CL emission with QWP having the fast axis oriented at $45^\circ$ respect to the horizontal line of the parabolic mirror, coupled with a LP at $90^\circ$ . Right: far field CL emission obtained with the same QWP coupled with a LP at $0^\circ$ . . . . .	51
52	Comparison of the different total intensities. . . . .	52
53	Intensity comparison with LP at $0^\circ$ and $90^\circ$ for two spiral plasmonic lenses fabricated in the same way. . . . .	53
54	Intensity comparison with LP at $45^\circ$ and $135^\circ$ for two spiral plasmonic lenses fabricated in the same way. . . . .	54
55	Intensity comparison with QWP at $45^\circ$ plus LP at $0^\circ$ and $90^\circ$ for two spiral plasmonic lenses fabricated in the same way. . . . .	54
56	FDTD simulated emitted CL power per degree vs the zenithal angle $\theta$ . . . . .	56
57	Experimental emitted CL power per degree vs the zenithal angle $\theta$ . . . . .	56
58	Average CL emission intensity simulated with FDTD Lumerical solver. . . . .	57
59	Average CL emission intensity measured with the CL set-up. . . . .	57
60	Left: FDTD simulated CL emission distribution. Right: Experimental CL emission distribution, obtained with only the bandpass filter along the detection path. . . . .	58
61	Left: DOCP of the FDTD simulated CL emission. Right: DOCP of the experimental CL emission. . . . .	58
62	DC electron gun beamline in Building 2 at the ALS Facility. . . . .	I
63	The photocathode is positioned inside this vacuum chamber. In blue, the electrical connection for the ion gauge pump, used to maintain UHV conditions. . . . .	II
64	Top: Laser and optical table of the set-up. Bottom: spectrum of the femtosecond pulsed laser. . . . .	III
65	Left: section of the entrance of the solenoid [41]. Right: entrance of the solenoid and possible trajectories of the electron [24]. . . . .	IV
66	Steering magnets for the deflection of the electron trajectory. . . . .	V
67	Example of Lumerical structure. The simulation box is defined by the orange perimeter, inside which boundary conditions are applied. The guassian-shaped object represents the electromagnetic wave impinging on the nanostructure. The yellow square represents the a monitor. . . . .	VI
68	Spiral created with Lumerical script language. . . . .	VIII

# 1 Toward Ultrafast Electron Diffraction

## 1.1 Introduction

Step by step, science and technology are trying to push further the limits of our knowledge and understanding of nature. Nowadays, matter can be studied with a wide variety of characterization techniques, carrying out the analysis in very different conditions.

But what we do not know is more than what we know. A simple, in principle, phenomenon like the atomic motion still remains a great open challenge in modern science if we think about a real-time resolution analysis. Thinking about a chemical reaction, it is generally possible to know just the initial and final state of this phenomenon, losing the info about the time-scale at which the processes occur. For sure, a time-resolved characterization promises the possibility to understand at the most basic levels various processes in the study of molecules, materials, and biological systems. In the last years, great attention has been paid to improve the state-of-art techniques for time-resolved studies. We could mainly summarize them in terms of the probes are involved in: electrons and photons.

On one hand, photons represented the first approach for the studies. The progress in laser technology has enabled the generation of optical pulses of time duration comparable to the time-scale of atomic and molecular motion ( $< 100fs$ ). But ultrafast optical laser pulses can only give indirect spectroscopic info on the structural dynamics of the sample. This is why high-energy x-ray photons (or fast electrons) are required to resolve spatially atomic motion. On the other hand, as quantum mechanics teaches us, electrons show the dual nature of particle and wave. If they are accelerated with high enough energy to have a corresponding wavelength of the orders of the sample features, information regarding the space arrangement of atomic nuclei can be obtained. At the typical energies of  $30-300keV$ , electrons have subatomic De Broglie wavelengths ( $0.07-0.02\text{\AA}$ ). Developing the ability to generate electron bunch pulses, there is now the possibility to take snapshots of the sample under study at different times after the excitation of the sample itself through pump-probe system. Here, the possibility to carry out both time-resolved and spatially resolved analysis.

Ultrafast Electron Diffraction (UED) and Femtosecond X-Ray Scattering are among the designated techniques for the analysis of the physical and chemical dynamics.

While x-ray based structural analyses require huge and complex set-ups represented by the synchrotron sources, UED offers a relatively cheap, compact and effective solution, particularly suited for smaller size laboratories. Furthermore, due to the large difference between the Rutherford (charge particles) and Thompson (photons) cross sections, probing for example with  $10^6-10^7$  electrons yields the same number of scattered particles of a probe pulse made of  $10^{12}$  x-ray photons. Therefore electrons represents the preferred choice to study thin layers, surface effects, or gas phase samples.

The present work follows the way paved by previous researches developed at Lawrence Berkeley National Laboratory (LBNL) on ultrafast electron diffraction.

In a typical UED experiment, an ultrashort laser pulse deposits energy in a sample, exciting the phenomenon under investigation, while the electrons strobe at variable delays the relaxation pathways of the system. These snapshots will contain information on the structural evolution due to scattering interactions between electrons and sample, and therefore are recorded by a CCD camera. The final data are composed of different diffraction patterns containing the evolution of the system. This introduces two main requirements on the electron bunch probe: it must be short enough compared to the time-scale of the phenomenon we are interested in, and it must present a high brightness for obtaining clear and distinguishable patterns. Conventional UED were based at the beginning on DC photoguns, producing electron bunches in the range of tens of  $keV$ . Due to the their fermionic nature and the strength of the repulsive space charge forces at these low

energies, the electron bunch experiences a weakening in transverse coherence. For this reason, it results impossible to obtain sub-picosecond pulses with a huge number of electrons. The use of a radio frequency photogun demonstrated a minimization of the space charge expansion and recompression of the beam [33], where electron energies are of the orders of  $MeV$ . But also here, space charge effects arise, increasing the emittance. Indeed, the electrons extracted from the cathode could be so huge that a Coulomb screening of the rf field can occur, pushing back the electrons extracted during the successive pulse.

Different solutions were proposed until now to reduce the beam emittance for the improvement of the electron bunch brightness. Among them, the reduction of the emission area on the photocathode results one of the most promising ways on which to invest, paving the way to direct observation of ultrafast dynamics in complex samples.

The present work follows this direction, as it will be shown and clarified in the following.

## 1.2 HiRES beamline

The characterization of the structural evolution in time and space of the sample under investigation requires pulsed, high-density electron probes. The electron pulses must be as shorter as possible to resolve the dynamics of the experiment, presenting at the same time small transverse sizes and narrow angle spreads ensuring atomic spatial resolution. The High-Repetition rate Electron Scattering beamline (HiRES) at Lawrence Berkeley National Laboratory represents a new tool for high-flux, ultrafast electron diffraction. It is installed in the Advanced Photo-injector Experiment (APEX) area, located inside the ALS storage ring, and provides at the same time high peak field typical of RF-based electron sources, and electron flux comparable to static electron microscopes.

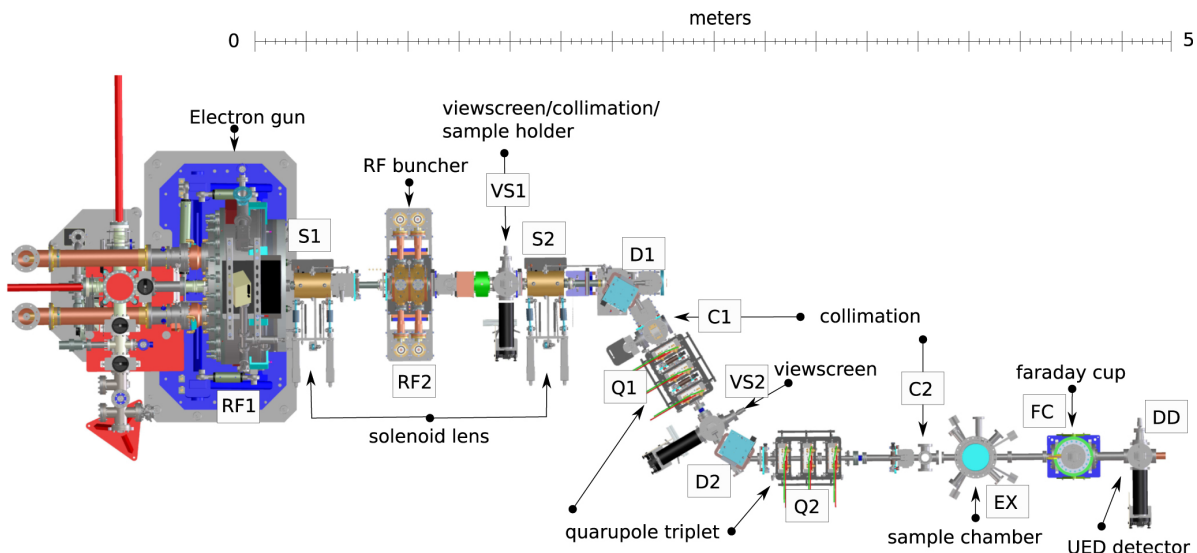


Figure 1: HiRES beamline layout [14].

As it is shown in fig.1, the beamline is about 5 m long, along where a series of elements are installed for different purposes, such as the transverse and longitudinal beam collimation and compression, together with the coherence length manipulation at the sample.

HiRES uses the APEX gun in the Very High Frequency (VHF) range to obtain the required short electron bunches. The aim of this part of the whole set-up is the extraction of electrons by means

of a pulsed laser working at  $\lambda = 1030 \text{ nm}$  in mode-locking to produce  $10 \text{ fs}$  long light pulses. The resulting light impinges on the photocathode to carry to multiphoton photoemission process for the final extraction. Then, these electrons are accelerated by the RF gun, able to guarantee a gradient of  $21.5 \text{ MV/m}$  to reach the nominal electron energy of  $800 \text{ keV}$ . Following, an RF buncher is positioned after the gun to compress longitudinally the exiting electron beam, reducing from  $100\text{s}$  of  $ps$  to  $100\text{s}$  of  $fs$  the pulse-lengths. The following components are composed of a series of magnets that serve to accelerate and collimate the beam. Once electrons reach the sample chamber, they interact with it and a diffraction pattern is recorded on a UED detector. Summarizing, the sample is excited with ultra-short laser pulses in the femtosecond regime, and then probed with the electron bunches which will contain the structural information, as it is shown in fig.2.

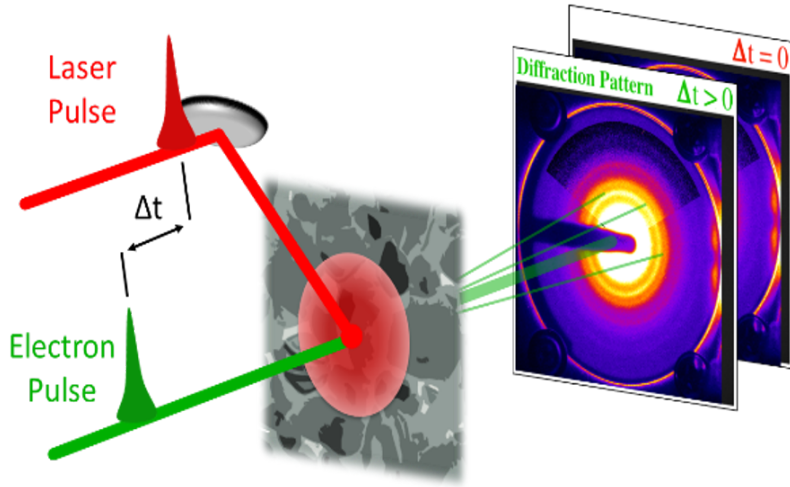


Figure 2: Schematic of a pump-probed experiment. Here, the result is the temporal evolution of the Bragg peaks, extracted by detecting different diffraction patterns in different times, enabled by the use of electron bunch pulses.

One of the main problems relative to these techniques is to obtain highly bright electron beam probe. On one and, the brightness is improved through the RF-gun, allowing to reach higher values of the maximum electric field. Such high fields rapidly accelerate the extracted electrons to relativistic energies, simultaneously minimizing the effects of the collective forces on the resulting beam, like the space charge or intrabeam scattering, which are the main mechanisms at the basis of the lateral coherence degradation. On the other hand, the reduction of the active emission area from the photocathode results to be a promising way to achieve high brightness. Essentially, the basic idea is to go beyond the light diffraction limit, exploiting the coupling between the laser and surface plasmon polaritons, and constituting a new generation of photoemitters [10].

### 1.3 Nanoscale Photocathode for UED

The Ultrafast Electron Diffraction technique is highly dependent on the generation process of the probes. Essentially, the electron bunch must satisfy three main requirements. On one hand, it must be characterized by a small transverse size together with a small transverse momentum, i.e. it needs to present high-brightness to guarantee high spatial resolution. On the other and, it must be ultra-short to guarantee high temporal resolution. For this reason, metal photocathodes are

required to guarantee an ultrafast response to the pulsed laser.

Asking for high-brightness beam means to ask for low emittance beam. These quantities are among the most important figures of merit to establish the quality of an electron beam for ultrafast electron diffraction and imaging. In a simple description, they are linked together by the definition of time-averaged brightness

$$B = \frac{I}{4\pi^2\epsilon^2} \quad (1)$$

where  $I$  represents the total beam current and  $\epsilon$  the emittance. Specifically,  $\epsilon$  describes the distribution in the phase space of the beam, i.e. the area occupied in the position and momentum spaces. In diffraction, the brightness sets the limit for the maximum beam lateral coherence  $L_c$ , given a specific transverse sample dimension [14]. The lateral coherence length can be defined as

$$L_c = \frac{\lambda_c}{4\pi\sigma_{p,u}/mc} \quad (2)$$

where  $\sigma_{p,u}$  is the uncorrelated electron beam transverse momentum spread, being  $u = x, y$ , and  $\lambda_c$  is the Compton wavelength. Essentially, this parameter is an experimental requirement, since it determines the largest detail that can be resolved.

The state-of-the-art photocathodes for new electron sources can be summarized in two main categories: tip emitters and ultraflat surfaces. The former are able to emit few electrons with the application of a DC voltage in the range of hundreds of  $V$ . For the reason, they presents high extraction efficiency, but the amount of photoemitted electrons is too small to acquire a clear diffraction pattern. The emission area is quite reduced thanks to the tip dimensions ( $< 10nm$ ), but the geometry increases drastically the angular spread for the extraction, with a consequent increase of the emittance. The emission timescale is of the order of  $100s$  of  $fs$ , not fully exploiting the new developments on femtosecond laser technology. These are the main reasons that pushed researches in UED analysis to ultraflat bare surface metal cathodes. Usually, a UV-light pulsed laser extracts electrons in a time  $< 100fs$ , which are afterwards accelerated by a RF voltage. The main problem of these bare surfaces is that the emission area is of the orders  $100s$  of  $\mu m$ . Essentially, there is a gain in the terms of fast response, but a loss in terms of emittance.

A new generation of photocathode exploits the plasmonic nanopatterns to achieve nanoscale, femtosecond and high-energy electrons not satisfied by the previous emitters. Lasers are coupled with collective oscillations of conduction band electrons closed to the surface, called surface plasmon polaritons (SPPs), in the near-IR range to stimulate multiphoton photoemission processes. The use of near-IR light reduces the problem of high reflectivity of metals photocathode in UV regime, while the light-SPPs coupling allows the reduction of the effective emission area thanks to periodic nanopatterns. Moreover, due to the closest distance to the surface, electron-electron scattering is drastically reduced, increasing the efficiency of extraction.

Some of these plasmonic structures have been already studied and characterized in terms of absorption and field enhancement. Among them, it is worth to mention the nanoarray of periodic rectangular nanoholes or nanotrenches made on a gold or copper substrate [38, 39]. The main problem of this type of nanostructure is the spatial distribution of the electric field coupled with the SPPs. Essentially, the field is drastically enhanced at the edges of the grooves while the plasmons are propagating inside the features, therefore acting as tip-emitters.

Another interesting candidate for UED analysis is the bullseye structure [43]. Here, the electromagnetic energy is enhanced and focus in a tiny spot at the center of the structure thanks to

coupling of a radially polarized laser with the surface plasmon polaritons. These 2D standing waves propagating inward the bullseye and coming from all the directions interfere constructively in the central plateau, acting as a resonant cavity. Due to the reflections of the plasmon with the edges of the central portion, a resonance condition can be observed and characterized. The main problem is the huge difficulties in the alignment of the center of the radial polarization with the center of the bullseye: a small off-axis displacement can reduce the coupling efficiency of the grating since the symmetry will not be anymore exploited.

An alternative nanopattern formed by archimedean spiral grooves paves the way to overcome the difficulties concerning the laser-plasmonic lens alignment. The chirality of the structure enables the excitation of SPPs through a circular polarization. For this reason, no matter the position of the center of this polarization, the corresponding electric field will result always perpendicular to the features, guaranteeing the coupling with the grooves. The working principle is essentially the same as for the bullseye: the inward propagating SPPs will interfere constructively in a small spot at the center of the spiral, giving rise to a field enhancement able to stimulate multiphoton photoemission. This non-linear optical process is of fundamental importance in metal photocathode, since the absorption of more than one photon per electron enable to overcome the high working function.

At the end, also the spiral configuration will be able to overcome the diffraction limit, with important improvement on the extracted beam emittance.

## 2 Theoretical Background

### 2.1 Multiphoton Photoemission

The photoemission is a threshold process consisting in the extraction of an electron from a metal due to the absorption of a photon impinging on the surface. The photon energy must be higher enough than the metal work-function to guarantee the emission. Indeed, once the photon is absorbed and the electron is promoted to higher energy levels, it must reach the surface where it can be extracted. During this travel, the electron will be subjected with a certain probability to electron-electron scattering mechanisms, reducing its kinetic energy. If the electron energy is still higher than the metal work-function, the photoemission can occur.

A rigorous theoretical approach to the photoemission process requires a full quantum-mechanical treatment of the complete coherent process in which an electron is removed from an occupied state within the solid [29]. Theoretical approaches of this type treat the photoeffect as a *one – step process*. The less accurate but simpler and more instructive approach is the so-called *three – step model*, introduced by Berglund and Spicer [2], and revisited specifically for photocathode by Dowell and Schmerge [10]. Here, the process is artificially separated into three independent parts:

- Optical excitation of an electron from an initial into a final electron state within the metal.
- Propagation of the excited electron to the surface.
- Emission of the electron from the solid into the vacuum. The electron traverses the surface.

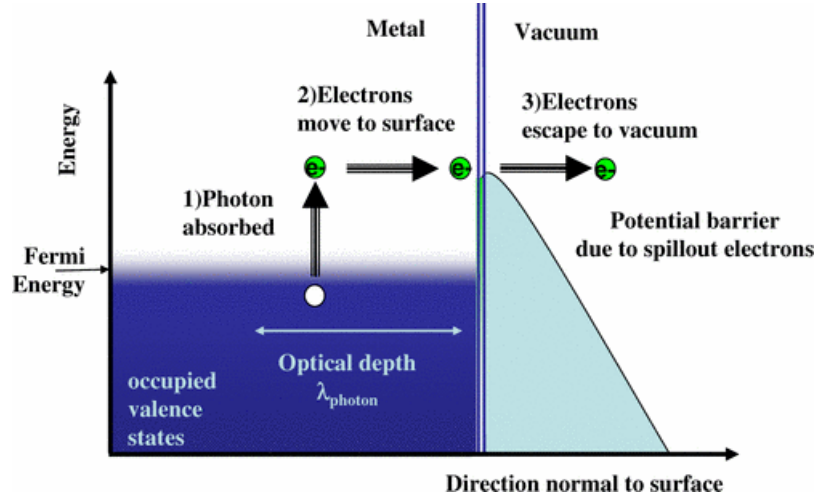


Figure 3: Schematic representation of the three-step model [10].

In the linear intensity regime, where the electron is absorbing a single photon, a linear relationship between the number of extracted electrons and the number of incident photons can be defined. The proportionality factor is called *quantum efficiency (QE)* [10] and is given by the product of probabilities of all the three steps to occur in this simple picture. The first step is dependent mainly on the photon absorption length and the reflectivity of the metal. Here, energy is conserved from the photon to the electron. The second step depends on the electron mean free path, which can be approximately determined by the electron-electron scattering in metals. In the last step, the electrons must be able to overcome the Schottky potential, given by the sum of the applied potential to the cathode and the image charge potential, taking into account the work-function.

In the case of high intensity regime, simultaneous absorption of  $n$  photons by a single electron can occur, promoting it to an unbound state. The current density extracted by the cathode in these conditions is described by the Fowler-Dubridge theory [11, 15], where the total  $J$  can be seen as the sum of all the partial  $J_n$  where  $n$  is the number of photons involved:

$$J = \sum_n J_n \quad (3)$$

The essential characteristics of a multiphoton photoemission is that the current density  $J_n$  scales as the  $n$ -th power of the intensity:

$$J_n = a_n A \left( \frac{e}{h\nu} \right)^n (1 - R)^n I^n T^2 F \left( \frac{nh\nu - e\phi}{k_B T} \right) \quad (4)$$

where  $a_n$  is an empirical constant, which varies strongly depending on the number of photons involved [37] and  $F$  is the Fowler function [15]. It is worth to notice that this expression corresponds to the well-known Richardson equation for the thermoionic photoemission for  $n = 0$ , i.e. only hot electrons are able to escape the metal.

The huge advantage offered by multiphoton photoemission is to increase the overall  $QE$  for metal photocathodes. Indeed, UV light is usually exploited in order to overcome directly the metal work-function, but with a very low  $QE$ . Being able to reach higher intensities, a multiphoton process can occur with higher probabilities than a single-photon photoemission [34], producing an electron bunch. It is worth to mention that in the case of a  $n$ -photon process, emission can occur also with sub-work-function photon excitation. The new generation of photocathodes exploit red and infrared laser to excite *surface plasmon polaritons (SPPs)* enabling the confinement of electromagnetic energy beyond the diffraction limit, enhancing the overall electric field in a sub-micrometer spot where multiphoton photoemission can take place.

To guarantee high time-resolution for UED characterizations, ultrafast electron pulses must be obtained. Therefore, the choice must fall on metal photocathode, where the main scattering phenomenon is the electron-electron scattering, for which excitations are on the timescale of attoseconds ( $1 \text{ as} = 10^{-18} \text{ s}$ ) [7]. The electron bunches are driven by femtosecond laser pulses, bringing the electron population far from being at thermodynamic equilibrium with the metal lattice. The time needed to reach such an equilibrium is quite longer than the laser pulse duration, with the consequent decoupling of the electron and lattice temperature [37]. A two-temperature model must be used in order to describe what happens to the electron population during the pulsed photoemission process. Furthermore, due to the increased difference in temperature, a non-thermal electron distribution must be considered for a more accurate theoretical description of the physics behind the photocathode emission. In other words, Fermi-Dirac distribution can not be invoked anymore so as the Fowler-Dubridge formula introduced so far must taken into account the temperature of hot electrons.

## 2.2 Plasmonics: a review

The underlying physics behind the new generation of photocathodes for UED is essentially composed by the field of *plasmonics*. It describes the interaction between electromagnetic radiation and conduction band electrons at metal-dielectric interfaces or metallic nanostructures, leading to an enhanced optical near field of sub-wavelength dimensions [30]. The results of this interaction are fundamental excitations of the conduction electron sea, called *plasmons*. In other words, a

plasmon is the quantum of plasma oscillation in a metal, i.e. a quasiparticle describing the collective oscillation of free electrons.

A classical framework based on Maxwell's equations results to be enough to catch the interaction physics of metals with electromagnetic fields. The main reason is the high electron density of metals, for which the energy levels spacing results to be insignificant compared to the thermal energy  $k_B T$  even at room temperature. Together with the Maxwell's equations, the so called *complex dielectric function*  $\epsilon(\omega)$  must be exploited, in order to understand the behaviour of metals for different frequencies of the applied electromagnetic fields.

### 2.2.1 Dielectric function of metals: Plasma model

For the purpose of our analysis, a simplified *plasma model* can be adopted to describe the metal response in the optical regime. Here, electrons are depicted as a gas of free particles of number density  $n$  moving against a fixed background of positive ion cores. It is worth to mention that this approach finds its limits of validity in the ultraviolet frequency range for alkali metals, due to their free-electron-like response, while in the visible range for noble metals like silver or gold, where interband transition can occur.

Taking into account the electron band structure by means of the effective mass approximation  $m$ , a simple equation of motion can be written for an electron of the plasma sea:

$$m \frac{d^2 x}{dt^2} + m\gamma \frac{dx}{dt} = -eE \quad (5)$$

The  $\gamma$  factor represents a characteristic collision frequency  $\gamma = 1/\tau$ , with  $\tau$  being the relaxation time of the free electron gas. In other words, eq.(5) takes into account the damping process occurring via collisions. Assuming a harmonic time dependence  $E(t) = E_0 e^{-i\omega t}$ , a possible solution could be  $x(t) = x_0 e^{-i\omega t}$ , where  $x_0$  takes into account any possible phase shift between the electron motion and the driving electric field,

$$x(t) = \frac{e}{m(\omega^2 + i\gamma\omega)} E(t) \quad (6)$$

This displacement for each carrier contributes to the total macroscopic polarization  $P = -nex$ ,

$$P = -\frac{ne^2}{m(\omega^2 + i\gamma\omega)} E \quad (7)$$

and dielectric displacement  $D = \epsilon_0 E + P$ ,

$$D = \epsilon_0 \left(1 - \frac{\omega_p^2}{\omega^2 + i\gamma\omega}\right) E \quad (8)$$

where  $\omega_p^2 = \frac{ne^2}{\epsilon_0 m}$  is the *plasma frequency* of the free electron gas. Therefore, we have now an explicit expression for the complex dielectric function  $\epsilon(\omega)$  for the free electron gas:

$$\epsilon(\omega) = 1 - \frac{\omega_p^2}{\omega^2 + i\gamma\omega} \quad (9)$$

Another interesting way to visualize the dielectric function is to split it in real and imaginary parts,  $\epsilon(\omega) = \epsilon_1(\omega) + i\epsilon_2(\omega)$ :

$$\epsilon_1(\omega) = 1 - \frac{\omega_p^2 \tau^2}{1 + \omega^2 \tau^2} \quad (10)$$

$$\epsilon_2(\omega) = \frac{\omega_p^2 \tau}{\omega(1 + \omega^2 \tau^2)} \quad (11)$$

It is worth to notice the important frequency dependence of the metal response. Depending on the range in which we are working, the metal can behave like a perfect conductor (far-INFRARED) so as a dielectric material (ultraviolet regime), with some possible light attenuation dependent of the details of the bandstructures. For the wavelengths considered in this project (800 and 1030 nm), it is observed that  $\omega < \omega_p$  where the metal is still characterized by a metallic behaviour. On the other hand, for frequencies close to  $\omega_p$ ,  $\epsilon(\omega)$  is mainly real,

$$\epsilon(\omega) = 1 - \frac{\omega_p^2}{\omega^2} \quad (12)$$

and can be seen as the dielectric function of the undamped free electron plasma. Exactly the same cannot be said for noble metals due to the role played by the interband transitions, which lead to an increase of  $\epsilon_2$  (for gold, see [35]).

## 2.2.2 Surface Plasmon Polaritons

Among the different plasmonic phenomena present in nature, *surface plasmon polaritons* (SPPs) result to guarantee in principle a photoemission able to satisfy all the requirements on the electron bunch probe for UED.

The surface plasmon polaritons are collective oscillations of conduction band electrons in a metal coupled with photons, propagating along the metal-dielectric interface with a certain in-plane wave-vector  $k_{SPP}$ . They present a characteristic exponential decay perpendicular to the surface, with a characteristic decay-length of the order of 100s of nm in the dielectric, and 10s of nm in the metal. For this reason, it is easy to understand the potentiality offered by SPPs to confine in sub-wavelength dimensions the electromagnetic energy close to the metal surface with two fundamental effects: enhancement of the field leading to multiphoton photoemission, confined in a nm size spot on the surface, leading to a reduction of the probability of electron-electron scattering mechanisms, therefore increasing drastically the efficiency of photoemission.

The SPPs can be easily derived from classical Maxwell's equations applied to a flat interface between a metal and a dielectric. This will give us a glance on the physical properties of these propagating waves. In the hypothesis of non-magnetic media, absence of external charge and current densities, the Maxwell's equation lead the *wave equation* for the electric field:

$$\nabla^2 \vec{E} - \frac{\epsilon}{c^2} \frac{\partial^2 \vec{E}}{\partial t^2} = 0 \quad (13)$$

For sake of simplicity, this equation can be solved separately in the two regions of the interface, applying after the appropriate boundary conditions to find the solutions. To further simplify the treatment, we assume a harmonic time dependence of the electric field  $\vec{E}(\vec{r}, t) = \vec{E}(\vec{r})e^{-i\omega t}$ , giving rise to the *Helmholtz equation*:

$$\nabla^2 \vec{E} + k_0^2 \epsilon \vec{E} = 0 \quad (14)$$

The geometrical frame is defined by an interface parallel to the XY plane and coincident to  $z = 0$ . The problem result to be therefore one-dimensional, with  $\epsilon$  depending only on the  $z$  coordinate,  $\epsilon = \epsilon(z)$ . The dielectric space is defined  $z > 0$ , with a positive real dielectric constant  $\epsilon_d$ , while the metal occupies the region for  $z < 0$ , characterized by a dielectric function  $\epsilon_m(\omega)$ . The metallic behaviour required for the metal implies that  $Re[\epsilon_m(\omega)] < 0$ , satisfied if  $\omega < \omega_p$ .

To further reduce the complexity of the problem, we get ride of the  $y$ -direction, imposing therefore  $\partial/\partial y = 0$ . This allows to split the solutions in two different electromagnetic fields:

- $(E_y, H_z, H_x)$ ,  $s$  – polarized wave
- $(H_y, E_z, E_x)$ ,  $p$  – polarized wave

Let us start with the  $s$ -polarized plane wave. It reads in both the two spaces (1) and (2):

$$\vec{E}^{(1)} = A^{(1)} e^{-jk_x x} e^{-\alpha_z^{(1)} z} \hat{y}_0 \quad (15)$$

$$\vec{H}^{(1)} = (B^{(1)} \hat{x}_0 + C^{(1)} \hat{z}_0) e^{-jk_x x} e^{-\alpha_z^{(1)} z} \quad (16)$$

$$\vec{E}^{(2)} = A^{(2)} e^{-jk_x x} e^{-\alpha_z^{(2)} z} \hat{y}_0 \quad (17)$$

$$\vec{H}^{(2)} = (B^{(2)} \hat{x}_0 + C^{(2)} \hat{z}_0) e^{-jk_x x} e^{-\alpha_z^{(2)} z} \quad (18)$$

The quantities  $\alpha_z^{(i)}$ , with  $i = 1, 2$ , represent the component of the wave-vector perpendicular to the interface in the two media. Taking the reciprocal values,  $\hat{z}^{(i)} = 1/|\alpha_z^{(i)}|$ , we have info on the evanescent decay-length of the fields orthogonal to the interface. In other words, the solution is here a wave propagating along the  $x$ -direction, with attenuation along the  $z$ -direction.

Enforcing the boundary conditions is mandatory to satisfy properly the wave equation. In particular, the continuity of  $E_y$  and  $H_x$  at the interface must be imposed, leading to the condition respectively:

$$\left\{ \begin{array}{l} A^{(1)} = A^{(2)} \\ -\frac{E_y^{(1)}(z=0)}{\omega \mu} \alpha_z^{(1)} = \frac{E_y^{(2)}(z=0)}{\omega \mu} \alpha_z^{(2)} \end{array} \right. \quad (19)$$

Using these results, we obtain

$$A(\alpha_z^{(1)} + \alpha_z^{(2)}) = 0 \quad (20)$$

Since the two decay-lengths are real positive values, the only acceptable solution is the trivial one. On the other hand, taking into account the  $p$ -polarization wave,

$$\vec{E}^{(1)} = (A^{(1)} \hat{x}_0 + B^{(1)} \hat{z}_0) e^{-\alpha_z^{(1)} z} e^{-jk_x x} \quad (21)$$

$$\vec{H}^{(1)} = C^{(1)} e^{-\alpha_z^{(1)} z} e^{-jk_x x} \hat{y}_0 \quad (22)$$

$$\vec{E}^{(2)} = (A^{(2)} \hat{x}_0 + B^{(2)} \hat{z}_0) e^{\alpha_z^{(1)} z} e^{-jk_x x} \quad (23)$$

$$\vec{H}^{(2)} = C^{(2)} e^{\alpha_z^{(2)} z} e^{-jk_x x} \hat{y}_0 \quad (24)$$

and imposing the continuity of  $H_y$  and  $\epsilon_i E_z$  at the interface

$$\begin{cases} A^{(1)} = A^{(2)} \\ \frac{\alpha_z^{(1)}}{\omega\epsilon_0\epsilon_d} A^{(1)} = \frac{\alpha_z^{(2)}}{\omega\epsilon_0\epsilon_m} A^{(2)} \end{cases} \quad (25)$$

we obtain the characteristic equation of the TM modes,

$$\frac{\alpha_z^{(1)}}{\alpha_z^{(2)}} = -\frac{\epsilon_d}{\epsilon_m} \quad (26)$$

Attention must be paid for the sign: it requires that  $Re[\epsilon_m(\omega)] < 0$ , if  $\epsilon_d > 0$ . In other words, this propagating wave can exist only at the interface between a conductor and an insulator. Again, this can be possible if we are able to work with  $\omega < \omega_p$ .

The last equation, eq.(26), enables to define the dispersion relation of the SPPs for a simple flat interface, i.e. how the *propagation constant*  $k_{SPP}$  varies at different wavelength.  $k_{SPP}$  is the wave-vector along the direction of propagation of the SPP. Starting from the wave equation, it is possible to demonstrate that

$$(\alpha_z^{(1)})^2 = k_{SPP}^2 - k_0^2\epsilon_d \quad (27)$$

$$(\alpha_z^{(2)})^2 = k_{SPP}^2 - k_0^2\epsilon_m(\omega) \quad (28)$$

Substituting these expressions in eq.(26) gives the following dispersion relation:

$$k_{SPP}(\omega) = \frac{\omega}{c} \sqrt{\frac{\epsilon_d\epsilon_m(\omega)}{\epsilon_d + \epsilon_m(\omega)}} \quad (29)$$

Due to the complex nature of the dielectric function describing the metal, also  $k_{SPP}$  will result to be complex. At a first glance, forgetting about possible attenuations in the metal, it is worth to notice that eq.(29) shows the bound nature of SPPs, due to the photon-electron coupling. Indeed, the dispersion curve lies on the right side of the respective light line computed for the dielectric considered.

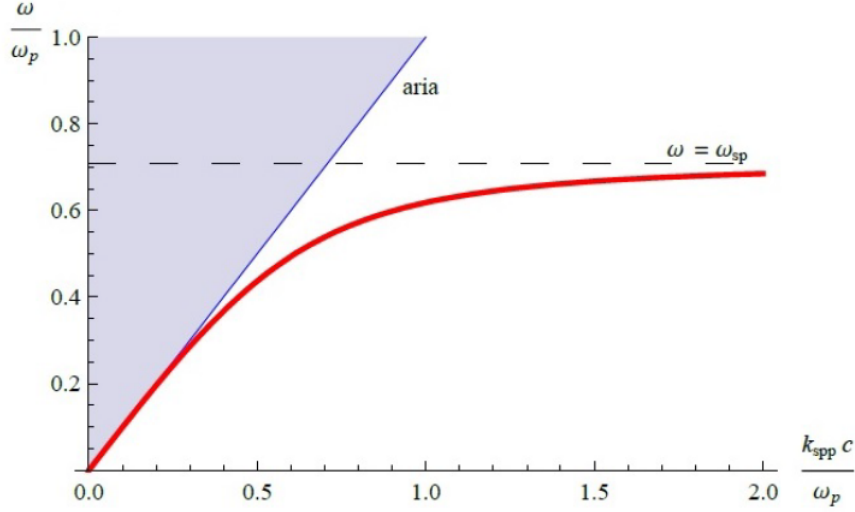


Figure 4: Dispersion curve of a SPP at the metal-dielectric interface.

It is visible from the plot above that for high values of  $k_{SPP}$ , the dispersion curve assumes an asymptotic behaviour. The corresponding value of frequency for this asymptote can be easily found imposing  $k_{SPP} \rightarrow \infty$ . Therefore, it results that

$$\epsilon_d + \epsilon_m(\omega) = 0 \quad (30)$$

that reads for high frequencies as

$$\epsilon_d + 1 - \frac{\omega_p^2}{\omega^2} = 0 \quad (31)$$

From eq.(31) it is possible to derive the so called *surface plasmon frequency*:

$$\omega_{SP} = \frac{\omega_p}{\sqrt{\epsilon_d + 1}} \quad (32)$$

It is worth to notice that for  $\omega \rightarrow \omega_{SP}$ , the wave-vector of the propagating SPP becomes greater than the corresponding wave-vector of the impinging light. This means that photons cannot be directly coupled into surface plasmon polaritons, but an extra momentum must be supplied to the plasmons in order to be excited. Different phase-matching techniques exist, required to excite SPPs via three-dimensional beams. The nanostructures fabricated and analyzed in this project are currently based on coupling via grating.

For the reason above, an additional momentum  $\Delta k$  must be supplied to the photons such that

$$k = \sqrt{\epsilon_d} \frac{\omega}{c} \sin\theta_0 + \Delta k = k_{SPP} \quad (33)$$

where  $\theta_0$  is the angle of incidence of the laser beam, and  $\sqrt{\epsilon_d} = n$  the refraction index of the dielectric medium where light is travelling. A grating composed of grooves hollowed in a flat metal surface with periodicity  $g$  can offer the required momentum, expressed as

$$\Delta k = \nu \frac{2\pi}{g} \quad (34)$$

The pre-factor  $\nu$  is an integer number, representing the order of diffraction of the grating. Last observations about the properties of the surface plasmon polaritons concerns the dispersion curve in the range of frequencies  $[\omega_{SP}; \omega_p]$ . This range represent a forbidden gap, where SPPs cannot be excited, but the corresponding  $k_{SPP}$  is purely imaginary and the plasmons cannot propagate.

Finally, it is worth to notice that the previous dispersion curve is for undamped SPPs. For real metal-dielectric interfaces, the  $k_{SPP}$  reaches a maximum imposing a lower bound both on the wavelength  $\lambda_{SPP} = 2\pi/Re[k_{SPP}]$  and on the amount of mode confinement perpendicular to the interface.

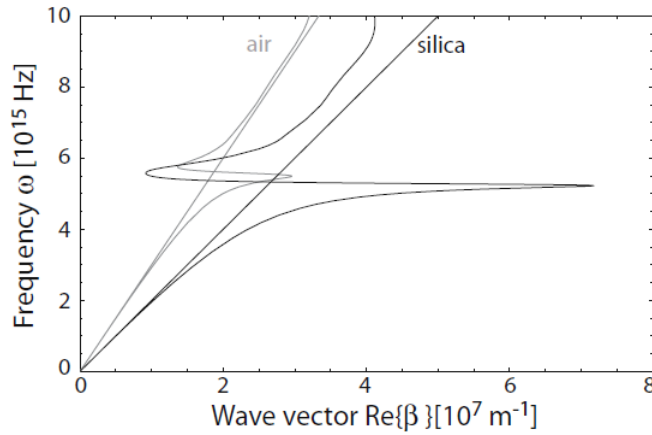


Figure 5: Dispersion relation of SPP at a real metal-dielectric interface [30].

The main difference between the ideal and real case is that a *quasibound* state for SPP is now allowed for frequencies in the range of  $[\omega_{SP}; \omega_p]$ .

### 2.3 The Archimedean Spiral

The project developed here at the Molecular Foundry concerns the optimization, fabrication and characterization of a specific pattern for a new generation of photoemitters: an archimedean spiral pattern on a gold surface.

Different spiral geometries are proposed in literature, for a wide range of plasmonic applications. Among the different examples, logarithmic spiral patterns are exploited as nanoantennas for pulsed light generation [3]. Archimedean spiral patterns, with one or more arms starting from the same center, are used both as nanoantennas and for nanofocusing applications, going beyond the diffraction limit [19, 25, 28, 49]. Another interesting application consists in using the archimedean spiral lenses as miniature circular polarization analyzer [8].

In this project, the archimedean spiral pattern represents a development and improvement of what was already done at the Molecular Foundry for the new generation of photoemitters for UED [40, 44, 45]. In particular, the choice of this structure represents a solution to experimental problems concerning the work done on the bull's eye plasmonic lens [43]. Both the two plasmonic lenses exploit the coupling of a pulsed laser beam via grating to SPPs, which in turn will propagate toward

the corresponding geometrical center. The excited SPPs propagating inward and coming from all the possible directions will in principle interfere constructively in the central plateau leading to a huge enhancement of the field in a sub-wavelength spot, where multiphoton photoemission can occur. The two structures differ in the type of polarization used for the SPP excitation. Recalling that only TM modes are able to stimulate SPPs, i.e. the electric field must be always perpendicular to the grating grooves, it can be understood that the bull's eye lens is designed to be excited by *radial polarization*, while the electric field pointing outward (see also [26, 48]). In order to fully exploit the nanofocusing capability, the center of the laser must coincide exactly with the geometrical center of the structure. In other words, it is of fundamental importance the quality of the laser alignment, made difficult by the need to maintain the sample inside the vacuum chamber of a DC-gun.

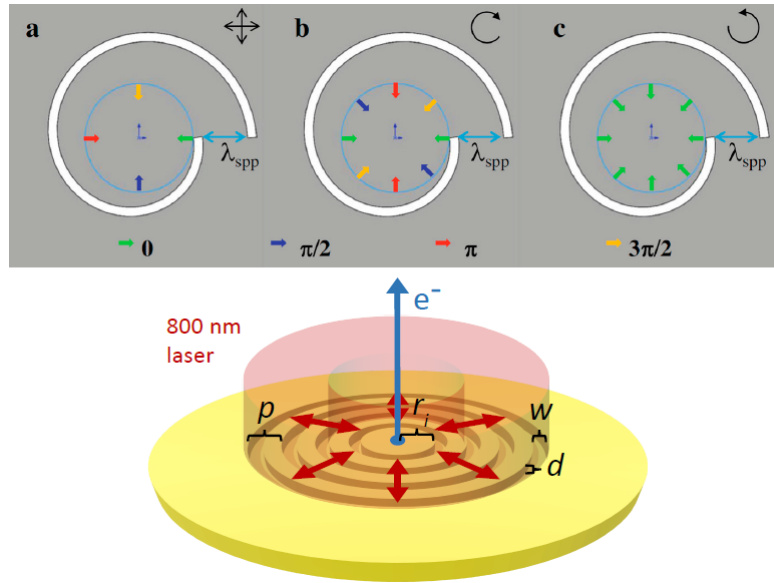


Figure 6: Top: working principle of the spiral plasmonic lens. The central and right figures show how the propagation of the SPPs is affected by the chirality of the circular polarization [20]. Bottom: working principle of the bull's eye. The center of the lens and of the radial polarization must match perfectly to fully exploit it as plasmonic lens [12].

The archimedean spiral can overcome these difficulties concerning the laser alignment since the pattern in principle can be coupled with a *circularly polarized* laser beam, whose chirality is always the opposite of the hollowed pattern [32].

A circular polarized light does not present any center, since the electric field changes phase in time in any point of the space. In order to exploit the constructive interference of SPPs in a sub-wavelength central spot, the grating must be able to compensate the time delay introduced in the excitation of the SPPs coming from different directions. The key idea at the basis of the choice for the archimedean spiral pattern is to compensate spatially the time delays affecting the different plasmonic propagations.

The working principle can be easily understood focusing on one-turn archimedean spiral, along with the polarization rotation of the incoming wave. The spiral can be represented in cartesian and polar coordinates in the following way:

$$\begin{cases} x(\theta) = r(\theta)\cos\theta \\ y(\theta) = r(\theta)\sin\theta \end{cases} \quad (35)$$

being  $r(\theta)$  a linear function of the azimuthal angle

$$r(\theta) = r_0 + b\theta \quad (36)$$

where  $b = 2\pi p$ , with  $p$  being the pitch (period) of the plasmonic pattern.

Let us consider two arbitrary opposite points on the spiral and the relative surface plasmon polaritons generated in that points and travelling towards the center. The first generated plasmon will require some time to reach the focal point. The same will occur for the second plasmon, coming from the opposite direction, to which the time delay of the polarization rotation must be added. For simplicity, let us consider  $\theta_1 = 0$  and  $\theta_2 = \pi$ . Considering propagating plane-wave plasmons having the same amplitude,

$$\begin{cases} e^{-ik(r_0+b\theta_1)} = e^{-ikr_0} \\ e^{-ik(r_0+b\theta_2)}e^{-i\pi} = e^{-ik(r_0+b\pi)}e^{-i\pi} \end{cases} \quad (37)$$

the relation of constructive interference in the center can be expressed by the phase-matching equality:

$$e^{-ikr_0} = e^{-ik(r_0+b\pi)}e^{-i\pi} \quad \implies \quad e^{-i(kb\pi-\pi)} = 1 \quad (38)$$

$$kb\pi = \pi \quad \implies \quad kb = \frac{2\pi}{\lambda_{spp}} \frac{p}{2\pi} = 1 \quad (39)$$

$$p = \lambda_{spp} \quad (40)$$

This equality gives a simple but important result: the right design of the period enables the constructive interference in the geometrical center of the pattern. While, in a first approximation we could say that the interference is totally independent on the starting radius  $r_0$ . These results pave the way to the next chapter, where the fundamental relation between structural design and plasmonic performances is analyzed.

### 3 Toward a new plasmonic photocathode

#### 3.1 Plasmonic Lens Design and Electromagnetic Simulations

In this chapter, the design and optimization of the archimedean spiral plasmonic lens for the new generation of laser-triggered, ultrafast electron sources are described. The design is completely based on the electromagnetic CAD Lumerical [22]. This powerful software tool solves the electromagnetic problems in the time domain using the Finite Difference Time Domain (FDTD) solver, enabling to perform detailed spatial- and time-resolved electromagnetic simulations to better clarify how the interplay between light-plasmon coupling, plasmonic propagation and dispersion in these lenses governs their spatiotemporal response.

The wavelength of choice for the design is  $\lambda_{exc} = 800 \text{ nm}$  in order to perform the characterization of the structure (chapter 4) with a cathodoluminescence set-up. As it can be shown, adaptation results to be easy for to the case of  $\lambda_{exc} = 1030 \text{ nm}$ , which is the wavelength of the APEX laser. The material of choice is gold (Au) because of its plasmonic properties. It enables 4-photon photoemission using 800 nm wavelength laser [38]; it is oxidation resistant providing effective photoemission surfaces. Au also provides long SPP propagation length in the RED and near-INFRARED range, reaching also values greater than  $60 \mu\text{m}$  for thermally evaporated, template-stripped Au films [31, 35].

The simulations are performed for the *reflection* and *transmission configuration*. For both the configurations, a normally incident gaussian beam with a waist radius  $w_0 = 8 \mu\text{m}$  is used. It presents a circular polarization, given by the superposition of two linear polarized lasers with a phase-delay of  $\pi$ .

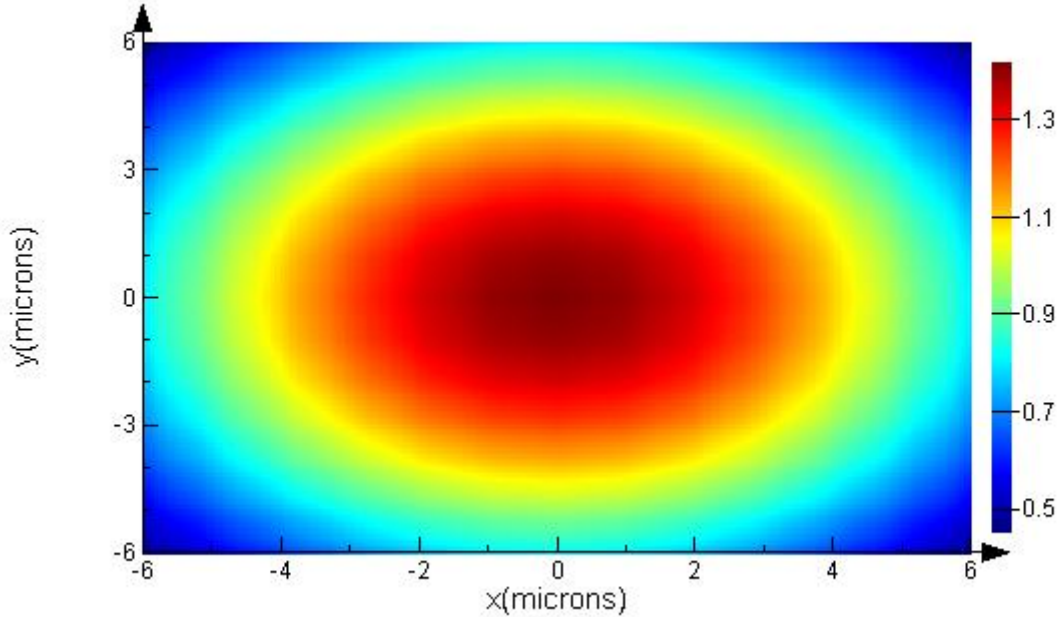


Figure 7: Magnitude of the electric field of the incident source.

The archimedean spiral plasmonic lens studied here consists of periodic annular grooves patterned

in the cathode-surface, forming a unique trench. The lens geometry is defined by five parameters (Fig.2): number of turns  $N$ , grating period  $p$ , the grooves width  $w$  and depth  $d$ , the starting radius  $r_0$ .

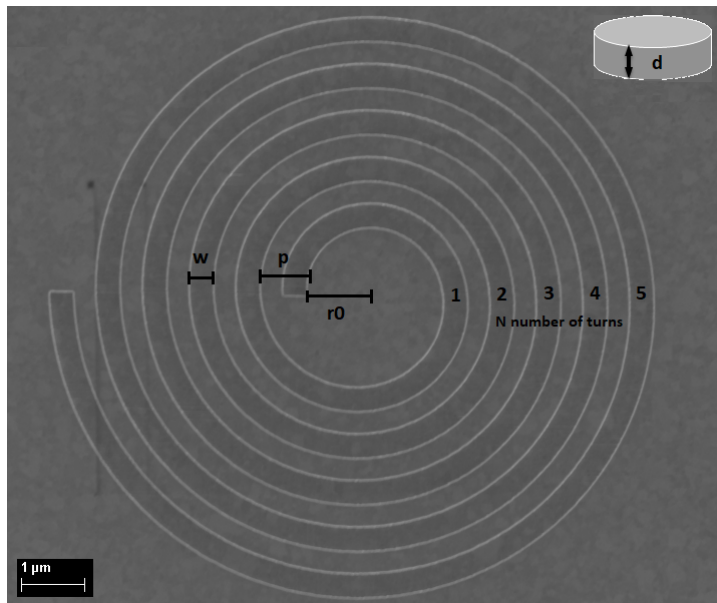


Figure 8: Geometrical parameters for the archimedean spiral pattern: grating period  $p$ , grooves width  $w$ , starting radius  $r_0$ , grooves depth  $d$  and the number of turns  $N$ .

The circular polarization is in principle able to generate 2D standing waves propagating toward the geometrical center of the lens, constructively interfering in a small focal point and increasing drastically the field enhancement.

The plasmonic lens ability to focus electromagnetic energy can be exploited both in reflection and transmission configurations, where some differences arise.

The most important thing to keep in mind is that such a pattern requires to be excited by a circular polarization to fully exploit its potentials [19, 20, 32, 49]. Indeed, it can be also excited under linearly polarized illumination [27], but this will lead to the excitations of couples of surface plasmon polaritons only along the direction of polarization, therefore losing the possibility to excite different plasmons from all the remaining radial directions.

### 3.1.1 Reflection configuration

In the reflection configuration, the field enhancement and the consequent photoemission are directed toward the position of the laser source: the field is enhanced in the same surface where the illumination occurs, as shown in fig.9.

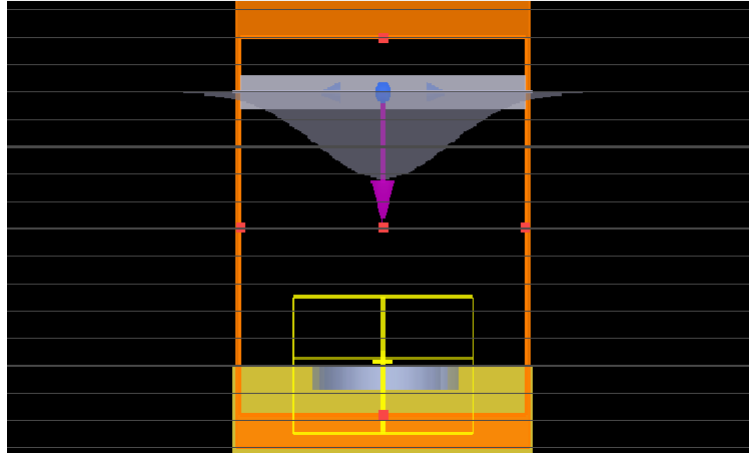


Figure 9: Reflection set-up for FDTD simulations.

The design of the spiral plasmonic lens is guided to optimize the geometrical parameters for maximum field enhancement at the center, for a range of wavelengths centered in  $800\text{ nm}$ . Indeed, the lens is illuminated with a  $3\text{ fs}$ -pulse laser, characterized by a bandwidth of  $600\text{ nm}$ . Each frequency component will excite different a plasmonic mode, contributing to the whole process of photoemission.

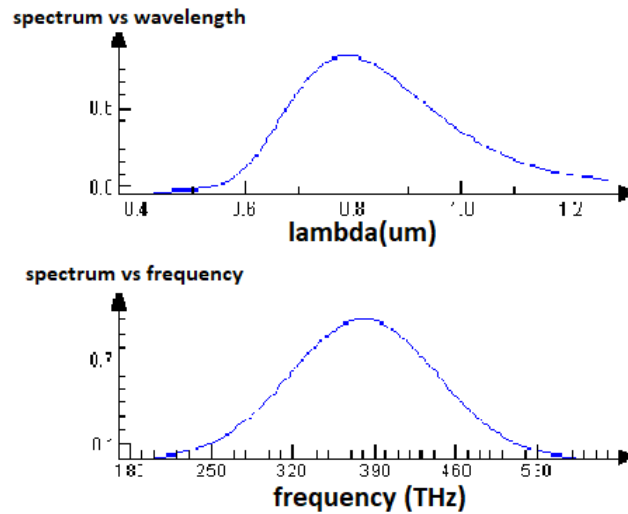


Figure 10: Spectrum of the input illumination.

The optimization is performed fixing some geometrical and physical parameters: the number of turns  $N$  is fixed to 5; the pitch is fixed to  $783\text{ nm}$ , from the result introduced in the previous chapter (eq.(40)); the width is imposed equal to half of the pitch; the starting radius is fixed to  $783\text{ nm}$ .

The depth of the grooves is the first parameter to be swept and optimized. It has been increased starting from  $40\text{ nm}$  up to  $110\text{ nm}$ .

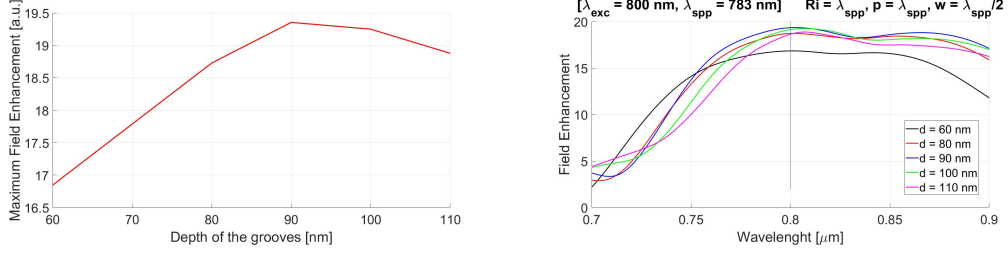


Figure 11: Optimization of the grooves depth.

As it can be seen above, the best value in terms of maximum enhancement is  $90\text{ nm}$ . Anyway, the field enhancement results to be close to 20 for a wide range of depth values. This is an important aspect from a fabrication point of view, due to difficulties concerning the aspect ratio of the grooves. Focusing on the plot on the right of fig.11, it is worth to notice that changing the depth corresponds to a vertical shift of the spectrum of the enhancement.

The same sweep procedure is performed for the period of the grooves, where the criterion of choice remains always the maximum enhancement in the center of the plasmonic lens.

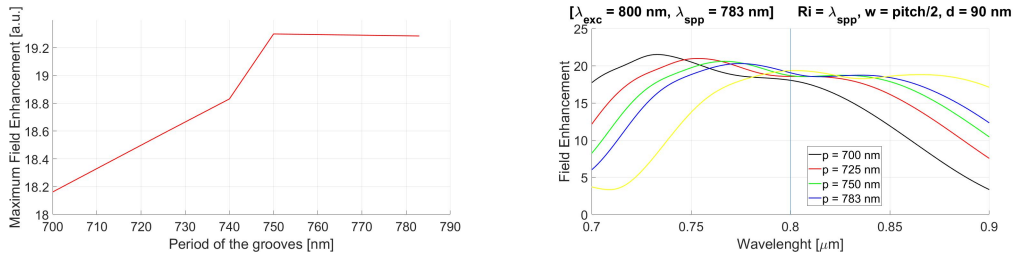


Figure 12: Optimization of the grating period.

The optimization is performed changing the pitch from  $700\text{ nm}$  up to  $800\text{ nm}$ . It is visible from the plot of the spectra of the field enhancement that a peak starts to arise toward  $\lambda_{exc} = 700\text{ nm}$ . As it will be clearer in the cathodoluminescence measurements, this strong enhancement is linked to the localized surface plasmons excited at the edges of the grooves. Anyway, the optimized value is  $p = 750\text{ nm}$ , guaranteeing the maximum enhancement at the center.

It is interesting to notice how varying the pitch leads to a horizontal shift of the spectrum. This relation together with the effect of the depth define the first two design rules for this type of plasmonic lens.

A further sweep procedure is performed on the grooves depth with the new value of the optimized pitch.

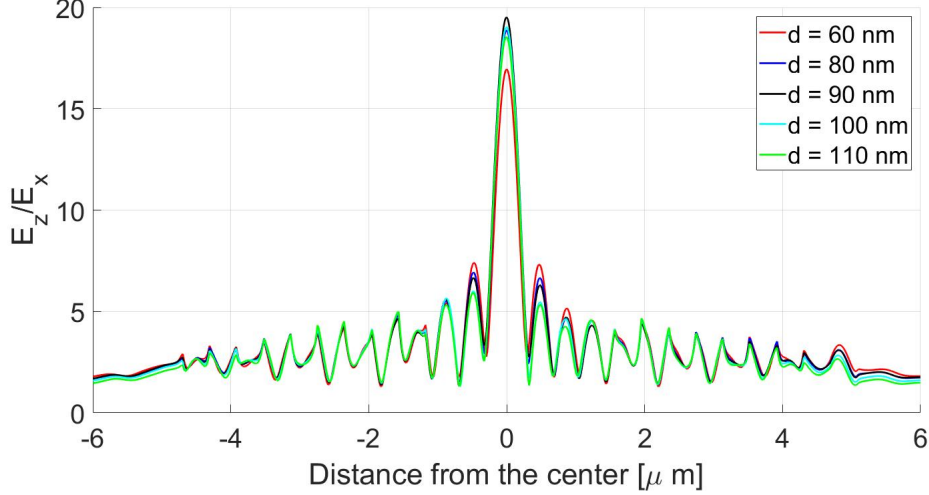


Figure 13: 2D distribution of the Field Enhancement along an X-cut.

Fig.13 shows how the different values of depth change softly the spatial distribution of the ratio between the component perpendicular and parallel to the surface. The main differences are visible for the central and first secondary lobes, affecting only the peak but not the shape. This comparison confirm to consider the field enhancement at the center as the main quantity to take into account for the optimization of the lens.

The sweep concerning the starting radius  $r_0$  does not show great changes for different values.

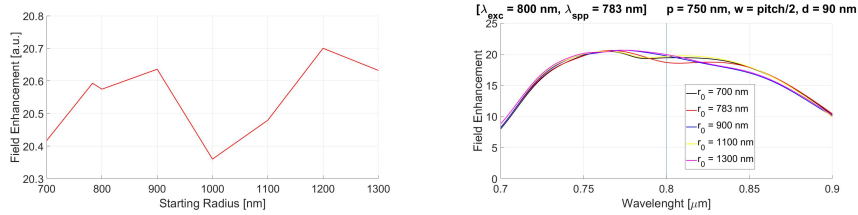


Figure 14: Optimization of the starting radius  $r_0$ .

It was already shown that the field enhancement is not affect by this parameter, in a first approximation (chapter 2). The plot on the left of fig.14 shows small variation of the maximum field enhancement at the center, confirming the theoretical result.

The final geometrical parameters chosen for the archimedean spiral plasmonic lens are:

- depth = 90 nm ;
- pitch = 750 nm ;
- width = pitch/2 ;
- starting radius = 900 nm.

The final aim of the structure is to enable the extraction of electrons through a multiphoton photoemission process that must occur in a sub-wavelength region of the Au flat surface. This need is directly related to the Liouville theorem for the emittance:  $\epsilon_{xy}$  can only be conserved during the propagation of the electron bunch, in case this will satisfy the canonical equation of motion. Therefore, reducing the phase-space area of the emitted electron beam requires to start directly from the source.

As for the bull's eye structure [44], also the spiral plasmonic lens has the ability to focus the electromagnetic energy in a central focal spot, where the component of the electric field perpendicular to the surface is highly enhanced, while the component parallel to the surface is made null exactly in the center.

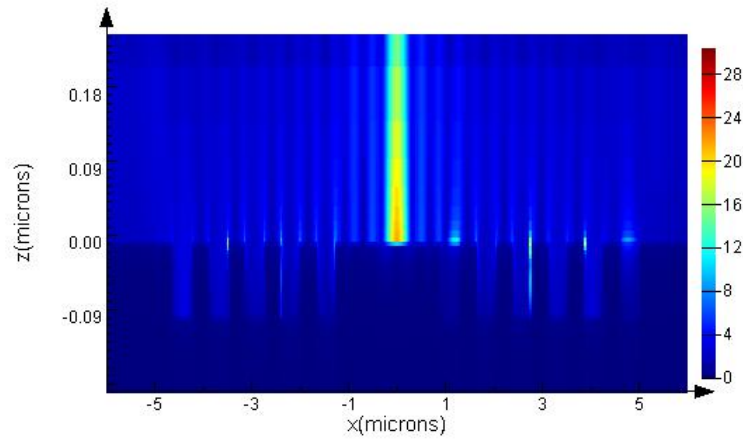


Figure 15: Magnitude of the electric field under circular polarization illumination, in a plane perpendicular to the surface

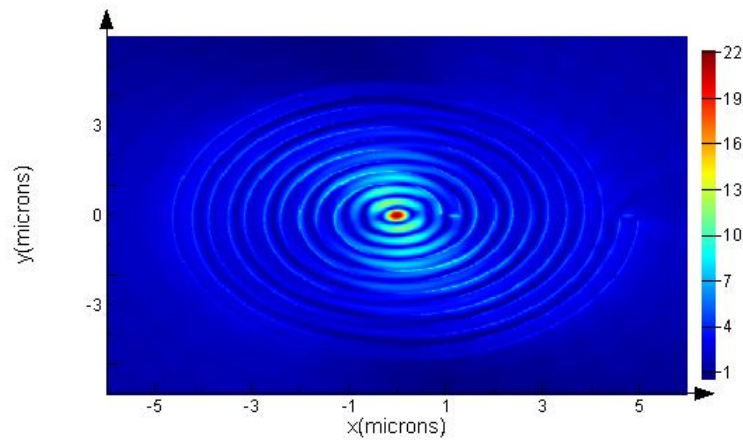


Figure 16: Magnitude of the electric field under circular polarization illumination, in a plane parallel to the surface

With respect to the bull's eye structure, the spiral pattern does not present the radial symmetry, which in turn is reflected in the asymmetric distribution of all the components of the electric field. Fig.13,17 show clearly how the perpendicular component of the electric field  $E_z$  is maximized in the center of the structure, while the parallel component  $E_x$  is zero for  $x = 0$ .

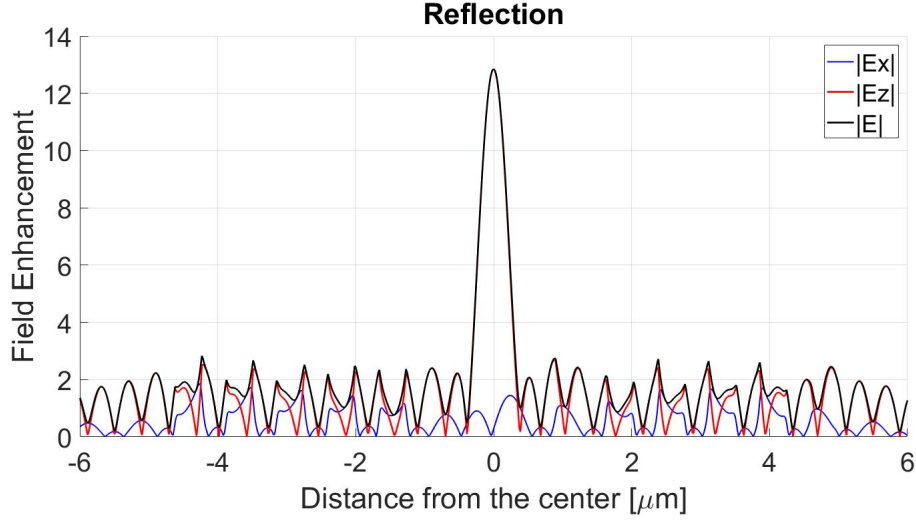


Figure 17: Spatial distribution of  $E_x$ ,  $E_z$  and the relative ratio. It is visible how in the center of the structure, for  $x = 0$ , the perpendicular component is highly enhanced, while the parallel is practically made null.

Furthermore, two secondary lobes appear at a distance of  $0.3 \mu\text{m}$  from the center (fig.13 and 17). In principle, they could contribute the photoemission process, increasing the emission area and therefore the source emittance. The importance is drastically reduced since the plasmonic lens is built in order to lead to multiphoton processes, in this case a *fourth order* photoemission. From the Fowler-Dubridge theory, this means that the current densities of the photoemitted electrons coming from the different points of the emission area go as the fourth power of the intensities:

$$\frac{J_{4,center}}{J_{4,lateral\ lobe}} \propto \frac{I_{center}^4}{I_{lateral\ lobe}^4} \quad (41)$$

The current density can be rewritten directly as a function of the electric field, enabling a better understanding from where the electrons will be extracted at the surface of the plasmonic lens,

$$J_4 \propto |E|^8 \quad (42)$$

In other words, the current density is subjected to a drastic shrinkage, leading essentially to emission only from a small focal spot with low transverse field. This is shown in the plot below, fig.18.

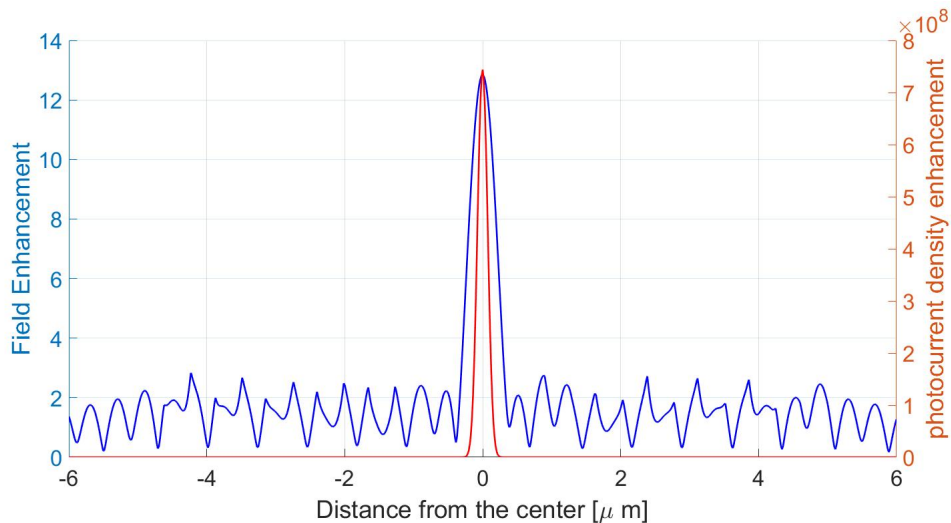


Figure 18: Superposition of the Field Enhancement and the relative 4-photon photocurrent density enhancement.

Another possible improvement of the maximum field enhancement is to increase the number of turns of the spiral pattern.

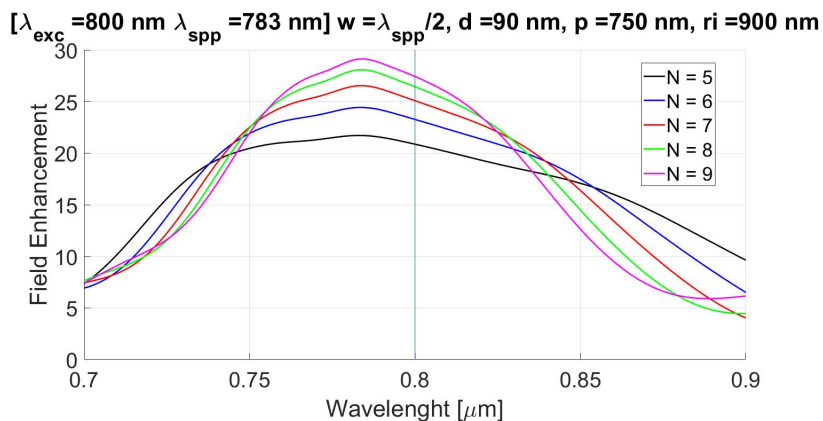


Figure 19: Spectral distribution of the field enhancement at the center of the spiral for different number of turns.

The spectral distribution of the field enhancement shrinks as the number of turns increases. This effect is due to the fact that a lower number of frequencies is able to couple with the grating. At the same time, fig.19 shows an increment of the maximum field enhancement. Indeed, more turns will couple more light, therefore more electromagnetic energy will be focused at the center of the spiral. The enhancement will not increase indefinitely with the number of turns, but it will reach a saturation when the distance of the last from the center of the spiral will start to be longer than the propagation length  $L_{prop}$  of corresponding SPPs.

Summarizing, the FDTD simulations showed the ability of the nanostructure to act as a lens, focusing the impinging electromagnetic energy in a focal spot, beyond the diffraction limit of light.

For ultrafast applications, it is also crucial to determine the temporal response of the emitter and its dependence on the lens geometry. The FDTD simulations are performed again considering a laser characterized by a pulse-length of  $3\text{ fs}$  full width at half maximum (FWHM). The aim is to obtain detailed impulse-response results about the lens.

Time and frequency are conjugate variables. Knowing the behaviour in one domain, it is possible to know how the lens will act in the other one. In the conditions of linear intensity regime, the laser-lens system can be described by a transfer function  $T(\omega)$ :

$$E_{center}(\omega) = T(\omega)E_{incident}(\omega) \quad (43)$$

$E$  being the complex electric field amplitude. The transfer function describes the whole behavior of the plasmonic lens. It is computed by dividing the Fourier transform of the time-resolved electric field at the center of the spiral pattern by that of the incident pulse. This calculation is performed directly through the FDTD Lumerical solver, able to work both in time and frequency domain. With a pulse-length of  $3\text{ fs}$ , Lumerical computes the transfer function on a wide range of frequency  $[500; 1900]\text{ nm}$ . The field enhancement introduced so far results to be exactly the modulus of the transfer function,  $|T(\omega)|$ . Once  $T(\omega)$  is determined, any behavior of the lens for longer pulse-lengths will be known.

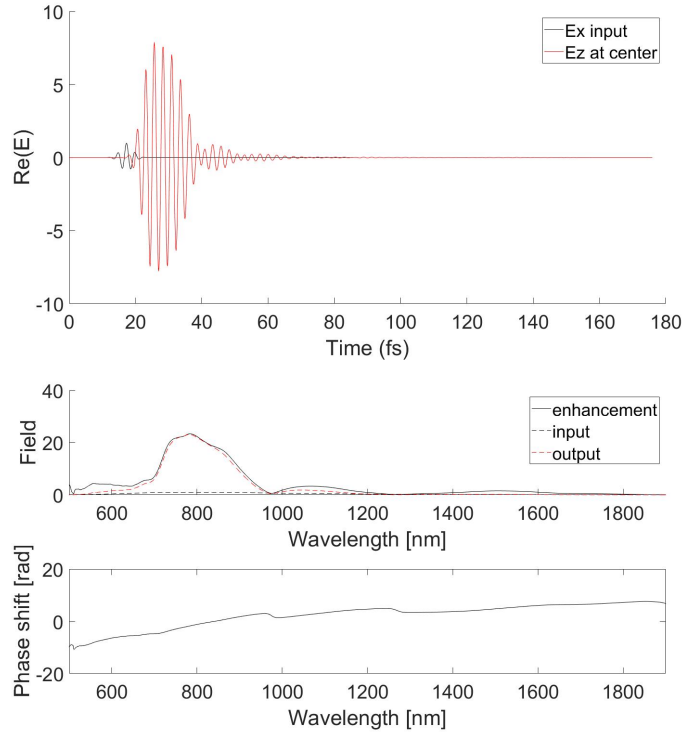


Figure 20: Top: temporal response of the optimized structure, with  $d = 90\text{ nm}$ ,  $p = 750\text{ nm}$ ,  $w = p/2$  and  $r_0 = 900\text{ nm}$  with  $N = 5$  turns. In black, the  $3\text{ fs}$  at FWHM incident circular polarized laser pulse, in red the response of the lens. Bottom: modulus (top) and phase (bottom) of the transfer function, computed by Fourier transform of the temporal response. The modulus of  $T(\omega)$  coincides with the frequency-dependent field enhancement.

Fig.20 (left) shows the superposition of  $E_{x,inc}$  and  $E_{z,center}$ , where the former is the maximum lateral electric field of the incident pulse, while the latter the normal electric field at the center of the spiral. For a  $3 - fs$  FWHM circular polarized laser pulse, the plasmonic lens produces a huge enhancement of the normal component  $E_{z,center}$ , with a temporal duration of  $10 fs$  FWHM. Fourier transforming these two quantities and dividing them,  $T(\omega)$  is obtained. It is interesting to notice the finite bandwidth that characterizes  $|T(\omega)|$ , which in turn defines a lower limit for the plasmonic duration. This lower bound is essentially due to the time needed for the SPPs generated at the outermost turns to reach the center and interfere constructively.

It is worth to notice that the bandwidth of this pattern results to be wider with respect to what observed for the bull's eye structure, where  $N = 4$  rings were analyzed [12, 44]. This indicates that the spiral pattern is faster than the bull's eye in focusing the electromagnetic energy. Therefore, it enables in principle the use of shorter pulse-length for the input laser, leading in this case to a possible improvement in terms of temporal resolution for UED applications. This can be better understood looking at fig.21

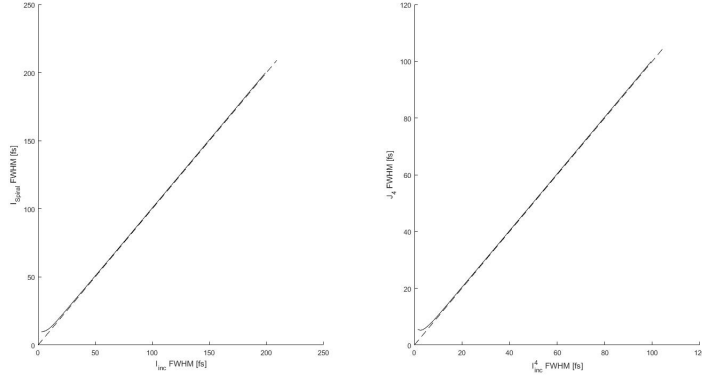


Figure 21: Temporal FWHM of the intensity (left) and of the photocurrent density (right) at the center of the spiral.

where the reduction of the FWHM for both intensity and generated photocurrent density. Simultaneously, a reduction of the pulse-length leads to a reduction of the maximum field enhancement at the center of the spiral, together with a reduction of the current density, as show in fig.22.

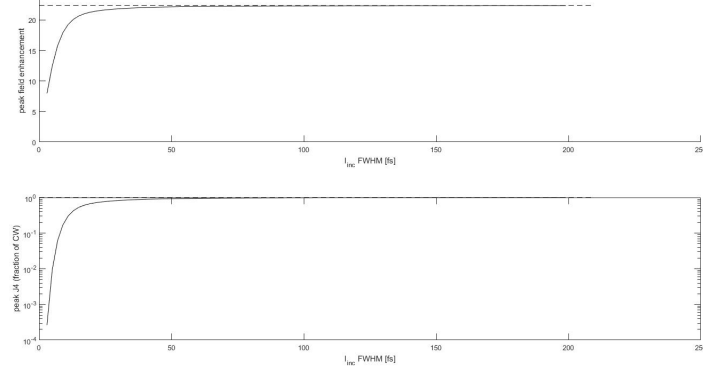


Figure 22: Peak field enhancement (top) and photocurrent density  $J_4$  (bottom) at the spiral center as a function of the incident pulse duration.

In other words, the reduction of the pulse-length  $I_{inc}FWHM$  can improve the speed of photoemission, therefore the temporal response, but at the same time with a decrease of the number of emitted electrons. Essentially, a trade-off exists between duration and charge of the photoelectron pulses.

### 3.1.2 Transmission configuration

The transmission configuration can constitute a real improvement for of the DC-gun set-up (appendix A). In particular, the laser alignment will not represent any more a problem, as it is in the reflection configuration.

The photocathode requires a ultra-high vacuum chamber in order to be operative. High levels of contaminants and random particles will act as scattering centers for the extracted photoelectrons, inhibiting first of all any kind of possible detection. For this reason, a series of FDTD simulations are conducted in transmission for a central wavelength of  $1030\text{ nm}$ , with the hope one day to work in this modality.

The design and optimization procedure is the same as for the reflection configuration. The transmission is characterized by the fact that now the main field enhancement and the photoemission will occur in the opposite surface to that one where the source illuminates the lens.

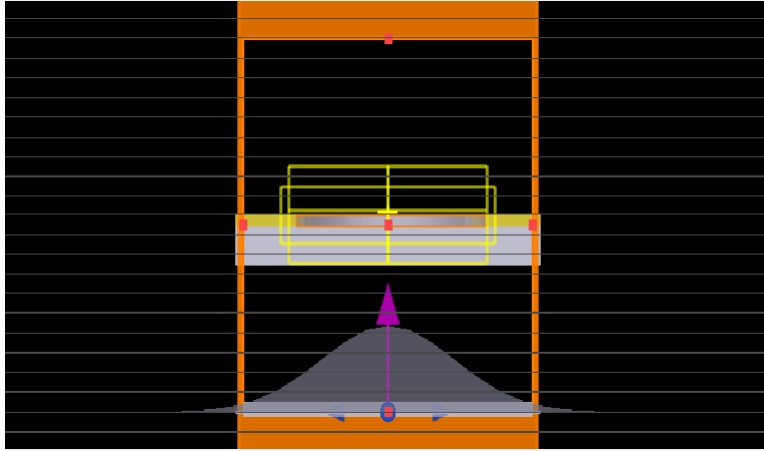


Figure 23: Transmission set-up for the FDTD simulations

The simulations are performed inserting  $200\text{ nm}$  of  $\text{SiO}_2$  as a support for the Au substrate of the spiral plasmonic lens. The source is again a circularly polarized gaussian beam, presenting a chirality opposite to that one of the spiral pattern, positioned at a distance of  $1.05\text{ }\mu\text{m}$  (more than one wavelength) from the Au- $\text{SiO}_2$  interface.

In this structure, the bottom of the grooves is not made of gold, as for the reflection, but is directly in contact with  $\text{SiO}_2$  and filled of the 'etch' material, characterized by a refractive index  $n = 1$  in the FDTD Lumerical solver.

The optimization is performed fixing the depth  $d = 30\text{ nm}$ , the starting radius  $r_0 = p$ , coinciding at the beginning with the wavelength of the SPPs propagating at the interface between Au and air (eq.(29)), and  $N = 5$  turns. The first sweep is performed on the grating period. The width is fixed equal to the half of the SPPs wavelength.

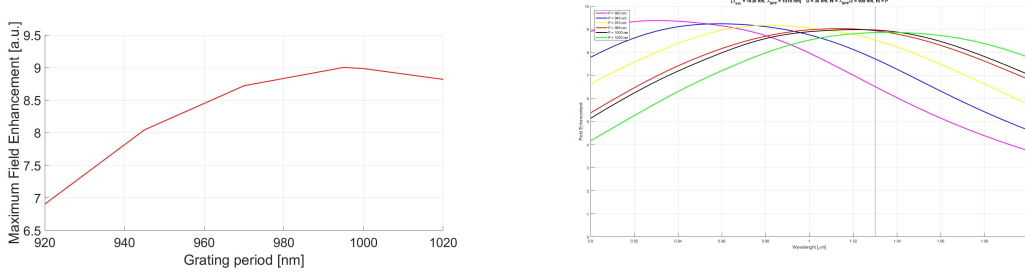


Figure 24: Optimization of the grating period.

The maximum field enhancement centered in  $1030 \text{ nm}$  is obtained for a grating period of  $1 \mu\text{m}$ . Again, the variation of the period leads to the horizontal shift of the frequency-dependent field enhancement.

The optimization continues with the sweep of the grooves depth.

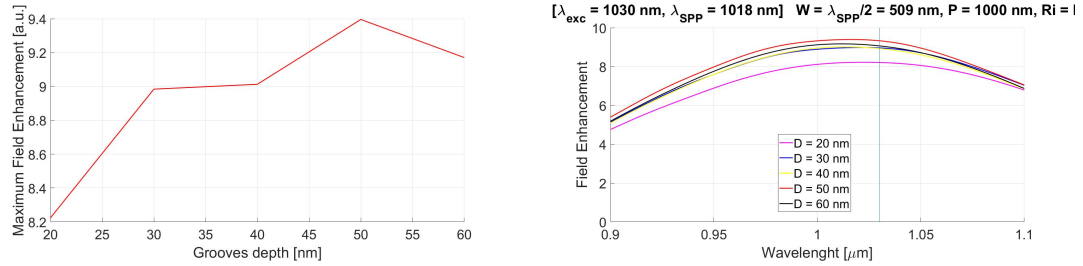


Figure 25: Optimization of the grooves depth.

The plot of fig.25 (left) shows how the maximum field enhancement reaches its maximum value for a grooves depth of  $50 \text{ nm}$ . Again, varying the grooves depth implies a vertical shift of the spectrum of the field enhancement. The starting radius does not affect consistently the spectral distribution of the field enhancement. Therefore, it is maintained equal to wavelength of the SPPs ( $1018 \text{ nm}$ ). The optimized values for the geometrical parameters for the transmission configuration are:

- pitch =  $100 \text{ nm}$  ;
- width =  $509 \text{ nm}$  ;
- depth =  $50 \text{ nm}$  ;
- starting radius =  $1018 \text{ nm}$ .

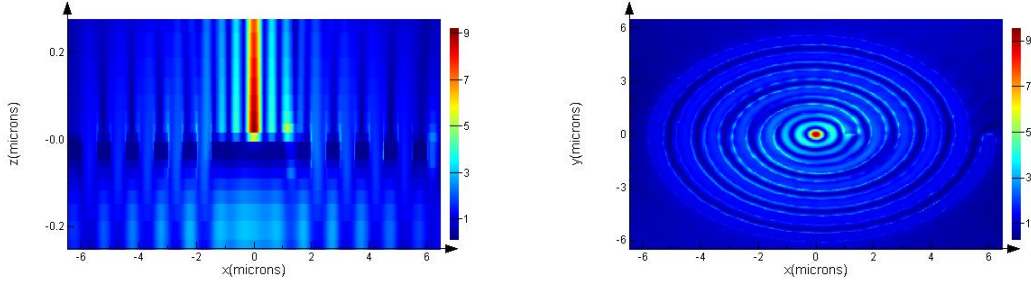


Figure 26: Magnitude of the electric field in a plane perpendicular to the surface (left) and parallel to the surface (right), for the optimized spiral plasmonic lens for  $\lambda_{exc} = 1030 \text{ nm}$ .

It is visible in fig.26 a small field enhancement at the Au- $\text{SiO}_2$  interface, which could represent a problem for the reliability of the structure and support. Further studies must be conducted on it to better understand the real entity of the phenomenon on the operation of the whole lens.

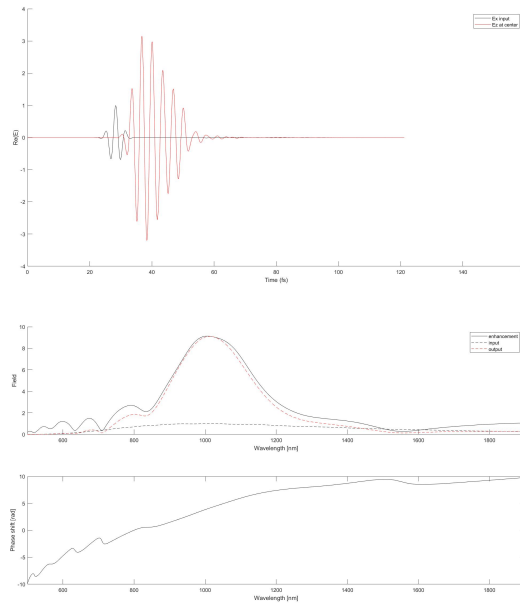


Figure 27: Top: temporal response of the spiral in transmission. Bottom: modulus of the transfer function  $|T(\omega)|$ , i.e. the field enhancement (up) and phase of  $T(\omega)$  (down).

Focusing on the temporal analysis, fig.27 shows a reduction of one order of magnitude of the field enhancement  $|T(\omega)|$  with respect to the reflection configuration. This is due to the losses occurring at the interface between the  $\text{SiO}_2$  and the gold film and during the propagation of the electromagnetic energy on the opposite face to the area where the circularly polarized laser is impinging. Same consideration as for the reflection set-up can be advanced for the relation concerning the maximum field enhancement and photocurrent density as functions of the FWHM of the input intensity.

Also if presenting a visible reduction of the maximum field enhancement achievable, this value could result enough to stimulate the multiphoton photoemission from the center of the plasmonic lens. Therefore, allowing to exploit the main advantage of this configuration, i.e. the reduction of complexity for the laser alignment.

### 3.1.3 Field Enhancement vs $\theta$

The last interesting simulation analysis that must be mentioned is relation between the frequency-dependent field enhancement and the impinging angle  $\theta$ , performed for  $1030\text{nm}$  in reflection. These study was conducted to understand how the incident angle  $\theta$  whit which the laser is impinging on the cathode can influence the final extraction of electron bunches in the DC electron gun set-up (appendix A). The simulations were run for  $\theta = 0^\circ, 2.5^\circ, 5^\circ$ .

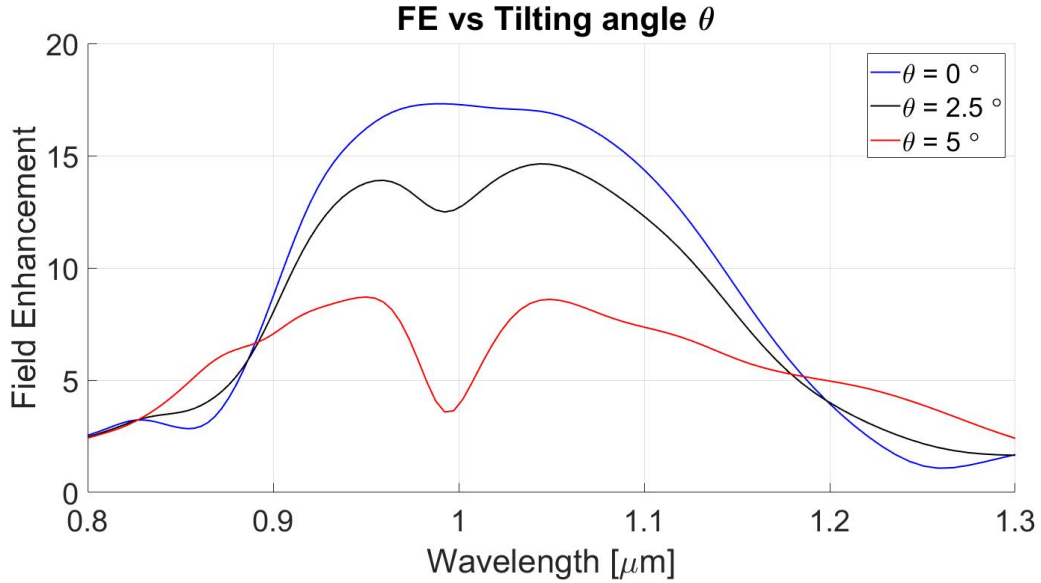


Figure 28: Spectral distribution of the field enhancement as a function of the tilting angle  $\theta$

The increase of the tilting angle  $\theta$  has mainly two effects on the frequency-dependent field enhancement achievable: the maximum enhancement is attenuated and a gap start to form centered close to  $\lambda_{exc} = 1 \mu\text{m}$ . Both the two effects can be explained by the phase delay introduced on the propagation of each couple of SPPs coming from opposite direction by the difference in path due to the tilting angle. Indeed, for  $\theta = 0^\circ$  all the couple of SPPs coming from opposite direction have the same phase. Therefore, they start to propagate at the same moment and ideally arrive at the same time at the center of the spiral pattern, interfering constructively. As soon as  $\theta$  starts to increase, one of the two SPPs of each pair will couple to the grating with a time delay, leading to an interference not any more in the center and not any more constructive: in the hypothesis of constant propagation velocity, the phase shift can lead to destructive interferences. Actually, this is what is happening to the SPPs excited by a wavelength  $\lambda_{exc} = 1 \mu\text{m}$ .

Summarizing, attention must be paid to the angle of incidence of the laser on the photocathode, since some plasmonic modes can be inhibited, decreasing the probability of multiphoton photoemission.

## 4 Nanofabrication

The fabrication process concerns only the archimedean spiral pattern for the reflection configuration, since the DC-gun set-up is currently working in this modality (see Appendix A).

Due to the nanometric dimensions of the plasmonic lens, classic photolithography is out of usage, since it is limited by diffraction effects. The most important fabrication techniques that can be exploited are:

- Electron Beam Lithography (EBL) ;
- Focused Ion Beam (FIB).

As already demonstrated in previous works [12, 44], the FIB introduces a lot of imperfections on the quality of the flat surface that must be obtained for the central plateau of the pattern. The sputtered surface presents high roughness (see [12]), and the resulting grains act as scattering centers increasing the decoupling between SPPs and photon. Essentially, as soon as the surface plasmon polariton encounters a scattering center during the propagation, it becomes radiative, emitting the electromagnetic energy in form of photons. Furthermore, a huge roughness is not desirable since the same grains, if too big, can act as tip-emitters, causing a high localization of the field enhancement, increasing the angular spread of the photoemission and deteriorating the quality of the emitted beam. Finally, FIB introduces also the problem of the gallium implantation, which modifies the plasmonic properties of the final photocathode.

Having this in mind, the EBL technique results to be the best choice to fabricate this lens.

The EBL is able to fabricate structures with sizes below 10 *nm*. At the same time, it is quite a complex technique which requires calibration of the dosage for the e-beam used to pattern the resist. Indeed, the electrons are focusing and then impinge on a resist. During this process, some patterns are made in order to understand what is the best dosage for the specific features that must be done, giving at the end the possibility to draw the geometry. The resist can be positive or negative, and after the exposure it must be developed (exactly as in the classical photolithographic process flow).

The EBL tool at the Molecular Foundry is the Vistec VB300 Electron Beam Lithography System. The e-beam lithography is exploited here in order to fabricate the template, part of the more general process used for plasmonic applications: the template stripping method.

### 4.1 Template stripping method

The template stripping (TS) process enables the transfer of the natural flatness of polished silicon wafer to metal films, resulting in topographic features in Angstrom sizes over large areas [21, 46, 47]. The new generation of photoemitters requires extremely smooth surfaces from where electron bunches can be extracted. The sub-nanometer flatness is a fundamental requirement since it enables the reduction of the angular spread in the multiphoton photoemission process and guarantees the reduction of defects, that can damp the propagation of the surface plasmon polaritons launched toward the center of the pattern.

The template stripping process for this specific work is schematically shown in fig.29.

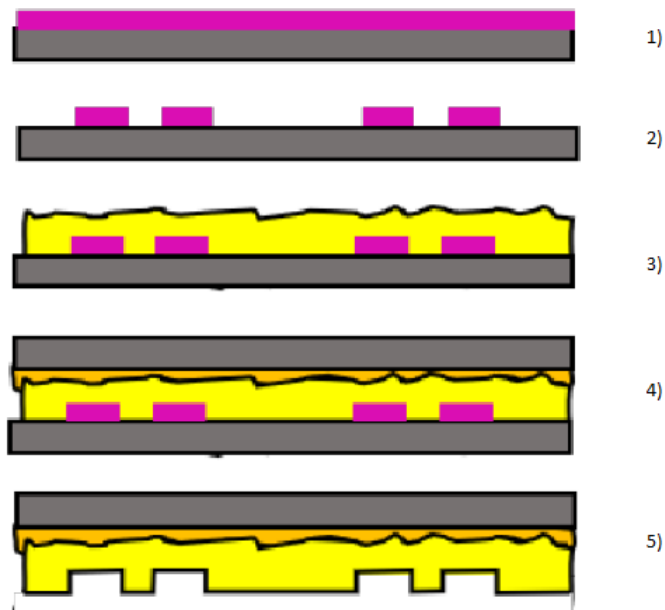


Figure 29: Schematic workflow of the Template Stripping process [12]. 1) Deposition of the resist (HSQ, 6%). 2) Exposition with EBL and development of the resist. 3) Deposition of Au with electron evaporation. 4) Deposition of the epoxy resin and of the new support, followed by the curing process of the resin. 5) Peel-off to detouch the new support and the Au film from the template.

A template is used to create a homogeneous, ultra-flat surface. A thin gold film is deposited onto the smooth template surface. Successively, an adhesion layer is added on top of the gold surface to attach a solid support onto the gold layer. Finally, the sandwich structure can be mechanically cleaved at the point of weakest adhesion. Indeed, due to the lattice mismatch between gold and the template material, the cleavage will occur at the Si-Au interface, leading to the release of the gold interface with a roughness similar to the template.

In particular, the fabrication process for the spiral plasmonic lens is:

- 90 *nm* of HSQ at 6% are patterned on a 4-inches prime wafer by means of the electron beam lithography;
- 200 *nm* of gold are deposited through electron evaporation on the template surface;
- epoxy resin is deposited on top of the gold surface and to bond it with the new support, made of prime silicon. The curing process of the epoxy resin follows its deposition;
- removal of the template through a peel-off process.

#### 4.1.1 Electron beam lithography

The first step in the whole process is the deposition and patterning of the template. Due to the sizes of the nanostructure, very high resolution is required. In order to satisfy this requirement, hydrogen silsesquioxane (HSQ) is exploited as electron beam resist [18, 50, 51]. HSQ is a nega-

tive e-beam resist, made by an inorganic polymer-type material. When exposed to electron beam irradiation, it undergoes a process of cross-linking, consisting in a scission of Si-H bonds, leading to an amorphous structure silicon dioxide. HSQ is deposited through a carrier solvent of methylsobutylketone (MIBK), achieving features smaller than  $10\text{ nm}$  [18, 51]. Essentially, the exposure and development of the HSQ layer leads to the negative pattern of the archimedean spiral structure, on which the gold film will be deposited through evaporation. A mask is required in order to define the geometry of the pattern, which must take into account the nature of the resist. The mask is made by means of the KLayout software with the following parameters:

- pitch =  $750\text{ nm}$  ;
- width =  $\text{pitch}/2 - 2\% \text{ pitch}/2$  ;
- starting radius =  $900\text{ nm}$  ;
- $N = 5$  turns.

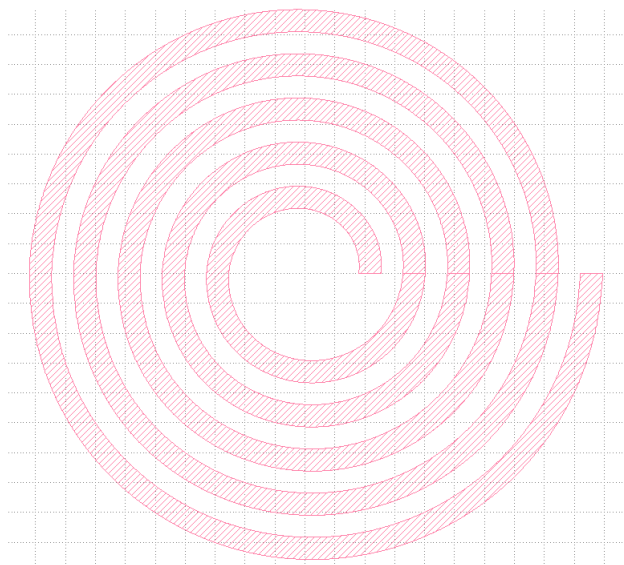


Figure 30: KLayout pattern for the plasmonic lens mask.

The width is defined subtracting the 2% of the nominal value since the electron beam is characterized by a gaussian shape, for which the edges of the features are subjected to alterations depending on the exposure dosage and the relative time [5]. The right dose is found after after different trials, for the desired profile.

All the fabrication processes are performed inside cleanroom classes 1000 and 100, starting with a 4-inches prime silicon wafer. The wafer is cleaned using acetone and isopropyl alcohol (IPA), since the final result will depend on the cleanness of the template. Subsequently, 6% HSQ is spinned at  $2000\text{ rpm}$ , forming the  $90\text{ nm}$  thick HSQ layer. The e-beam exposure and successive development will give the desired profile for the future structure. Six different doses are tested, whose dimensions are measured by scanning electron microscopy (SEM) with the in-lens mode.

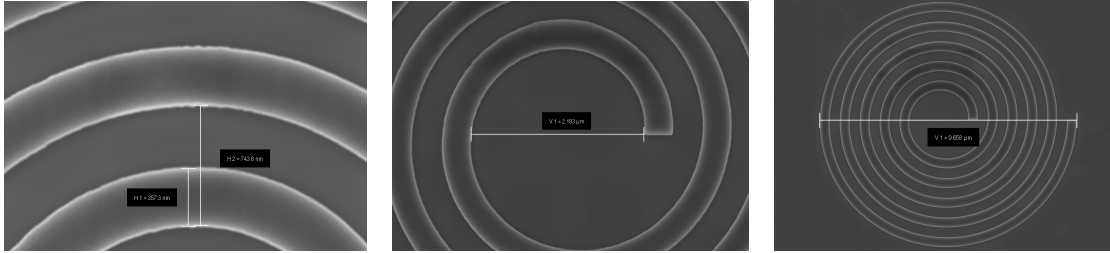


Figure 31: HSQ template made with EBL process. The images are taken with SEM system, exploiting the in-lens mode, enabling the detection of secondary electrons of type SE1. These electrons are emitted from the first layer of the surface, due to the interaction of the primary e-beam with the sample. Therefore, they contain important information about the surface of the template, enhanced by the use of low energy primary electron ( $3\text{ kV}$  in this case).

Measurements of the flatness of the template are performed through Bunker AFM Icon tool, present at the Molecular Foundry, used in Soft-Tapping mode.

#### 4.1.2 Gold film

The archimedean spiral pattern is obtained through the evaporation of gold onto the template. The gold layer is directly evaporated onto the template in order to exploit the poor adhesion at the Au-Si interface, enabling the mechanical cleavage of the template.

The thickness of the evaporated gold film is  $200\text{ nm}$  to avoid that the tail of the surface plasmon polaritons perpendicular to the direction of propagation at the bottom of the grooves will get in contact with the epoxy resin. In such a condition, the epoxy could start to burn, ruining the plasmonic lens itself.

The gold film deposition is performed under high vacuum condition ( $10^{-6}\text{ torr}$ ) through an electron beam evaporator. The structures are still visible with an optical microscope.

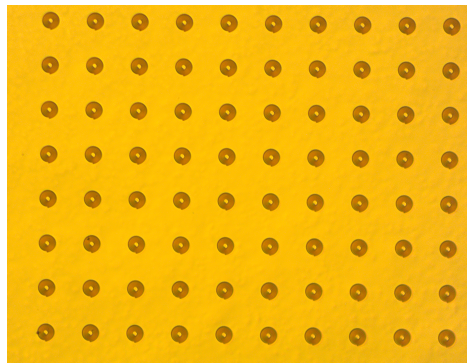


Figure 32: Gold film evaporated onto the template.

No adhesion layer is exploited in this step of the whole fabrication process. The aim is to exploit the poor adhesion between the Si and Au film to better perform the successive mechanical cleavage through a peel-off process.

### 4.1.3 Epoxy resin deposition

The successive step is the bonding of the patterned gold film to a new support, made of a prime silicon wafer piece. Again, the new support must be cleaned with IPA, in order to guarantee a good bonding. There are some constraints that limit the choice of the epoxy resin used for this specific application. This resin must satisfy different requirements:

- ability to work under ultra-high vacuum ( $10^{-11} \text{ torr}$ ) without outgassing, following the NASA standards;
- it must present good thermal and electrical conductivity;
- it must work as glue guaranteeing good adhesion between the gold and the new substrate.

The first requirement is due to the fact that the photocathode will be inserted inside a vacuum chamber of beamline, forming the DC-gun (present at the Building 2 at the Lawrence Berkeley National Laboratory, in the Advanced Light Source Division). The electrical conductivity is required to guarantee the possibility to supply an acceleration voltage inside the DC-gun to the extracted electrons toward a YAG-screen and a Faraday cup. A good thermal conductivity will increase the reliability of the photocathode. If the resin used does not allow a heat-flow, there is the risk to melt the gold film (depending on the laser power).

The choice falls on the EPO-TEK H20E epoxy resin. This is a two component resin, where one of the two components is filled of Silver. The curing process consists in inserting the resin inside the oven for 15 *minutes* at a temperature of  $120^\circ\text{C}$ . During the cure, the epoxy experiences a sort of crystallization during which the silver nanoparticles are kept in contact and a conductive path is formed. The curing temperature is chosen also to be under the eutectic reaction temperature between gold and silicon ( $363 \pm 2^\circ\text{C}$ ) [4], in this way avoiding the rapid diffusion of gold into silicon. Indeed, such a condition would destroy the smoothness of the surface between gold and the substrate and suppressing the ability to strip the gold film from the template.

The resin must be deposited as smallest as possible amount on the back of the structure, in order to avoid the alterations arising after the curing step. Due to the mismatch in coefficient of thermal expansion between gold and the epoxy, some mechanical stress can be introduced on the gold film, modifying the morphology and then the plasmonic properties of the lens. A solution for this problem could be to grow a thicker gold film, increasing the robustness of the spiral structures and to isolate the atomically flat surface from possible mechanical scratches. For this reason, some tests were conducted to grow  $1 - 2 \mu\text{m}$  thick gold film by means of electroplating, using the already deposited  $200 \text{ nm}$  thick film as seed. The experiments showed the poor reliability of the process since the seed starts to detouch from the template as soon as the voltage is applied, exactly due to the poor adhesion between silicon-based template and the gold film. Therefore, no film remains where to deposit the epoxy for the new support.

### 4.1.4 Peel-off process

The final step of the whole fabrication process is the cleavage of the template through the peel-off procedure. The mechanical separation can occur thanks to the poor adhesion between the Si-HSQ template and the Au film.

The procedure can be done after the cure of the epoxy resin. Indeed, once the two component are heated inside the oven and glue the new support, the mechanical cleavage can be performed. The peel-off is performed in two different conditions linked to the deposition of the epoxy:

- manual epoxy deposition with the use of a stick;
- epoxy deposition through a hydraulic press system.

The two different tests are performed to study the difference in terms of uniformity in the deposition of the epoxy resin on the whole sample.

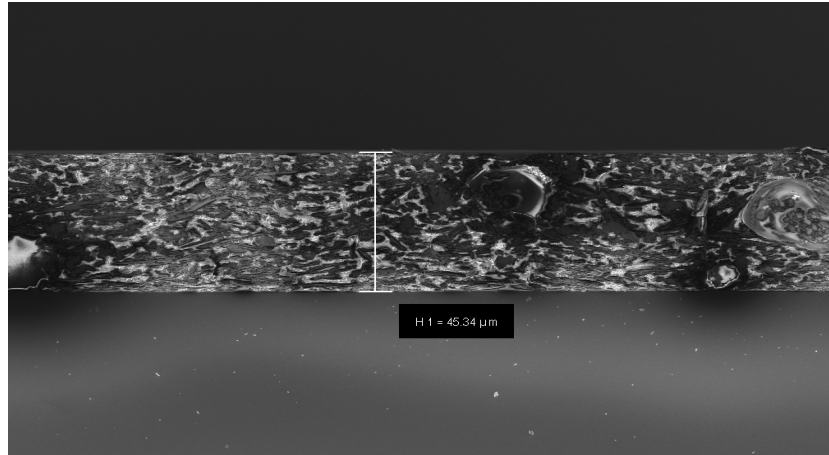


Figure 33: Cross section of the final structure. The deposition is performed here by hand. On top the gold film; in the middle the epoxy resin layer with a measured thickness of  $45 \mu m$ ; on the bottom the new support made of prime silicon.

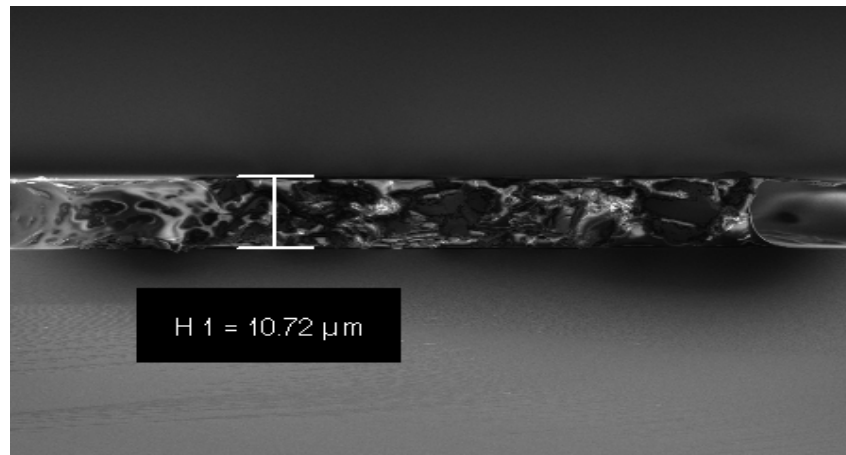


Figure 34: Cross section of the sandwich structure, with the deposition performed through the hydraulic press. The final thickness results to be close to  $10 \mu m$ .

Fig.33 shows a cross section taken with the SEM of the sandwich structure where the deposition is performed manually. The final thickness is of about  $45 \mu m$  of the epoxy resin. On the other hand, fig.34 show the cross section of sandwich structure resulting from the use of the hydraulic press. The pressure is of the orders of  $200 \text{ psi}$ , while the temperature of the plates is established to be  $140 \text{ }^\circ\text{C}$ , to guarantee a temperature as closest as possible to  $120 \text{ }^\circ\text{C}$  for the curing process. The tests are conducted with the same amount of epoxy deposited on the back of the gold film. As it is shown, the press leads to a reduction of the final thickness of the epoxy ( $10 \mu m$ ), since it is spread in a wider region than what happens with the manual deposition.

Focusing on the interface between the gold film and the cured epoxy, a difference in terms of adhesion can be noticed.

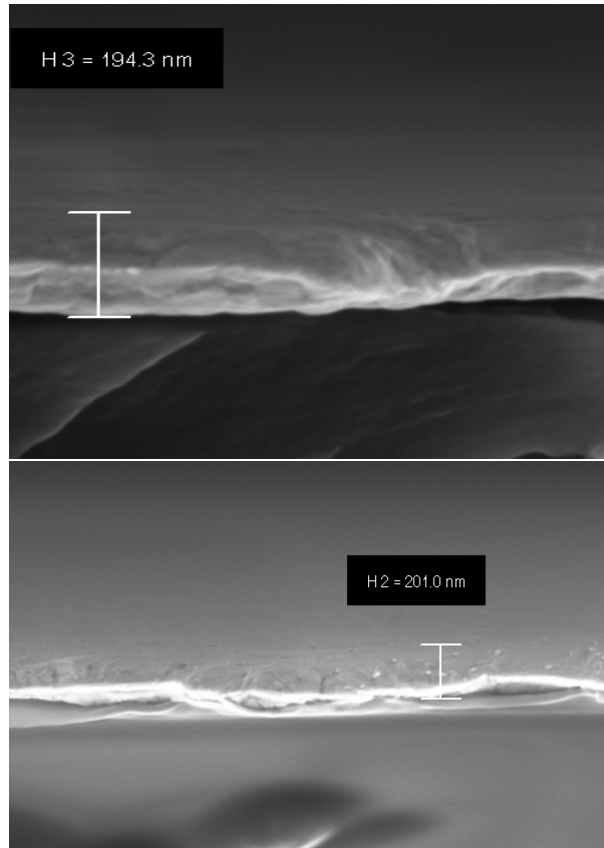


Figure 35: SEM image of the interface between the gold film and the cured epoxy. The deposition of the resin performed manually (top) shows less adhesion at this interface than the deposition performed with the press (bottom).

In both the SEM images, it is visible how the high precision of the e-beam evaporator, by means of which 200 nm of gold were deposited on the template.

The SEM image relative to the manual deposition of the resin shows a tiny black region at the interface between gold and epoxy, from where no secondary electrons are detected due to absence of epoxy, indicating a weaker adhesion than that one shown for the hydraulic press deposition. Indeed, here secondary electrons are detected also at the interface, showing simultaneously a better uniformity of the resin.

Summarizing, the deposition through the press can guarantee some improvements in terms of uniformity and better adhesion between gold and epoxy. Unfortunately, this method present the main limitation to make more difficult to perform the peel-off procedure. Indeed, it is observed that more resistance is experienced with the razor blade to peel off the gold structures from the template, increasing the probability to scratch the final spirals. This effect can be explained by simultaneous use of pressure and high temperature. On the other hand, the applied pressure together with high temperature led also to adhesive and cohesive failures, indicating in this case a weak bond strength of the epoxy with the new substrate, reducing the reliability of the process.

In the adhesive failure, the portion of gold onto which the epoxy is deposited remains attached to the template, while in the cohesive failure the gold is not transferred at all on the new support [13]. Both the failures are due to the incomplete cure of the epoxy itself. Indeed, here the high temperature is supplied directly by the two plates of the hydraulic press, not directly in contact with the sandwich structure. Therefore, the temperature cannot be applied on the whole area as uniform as with the oven, used instead for the first method of deposition.

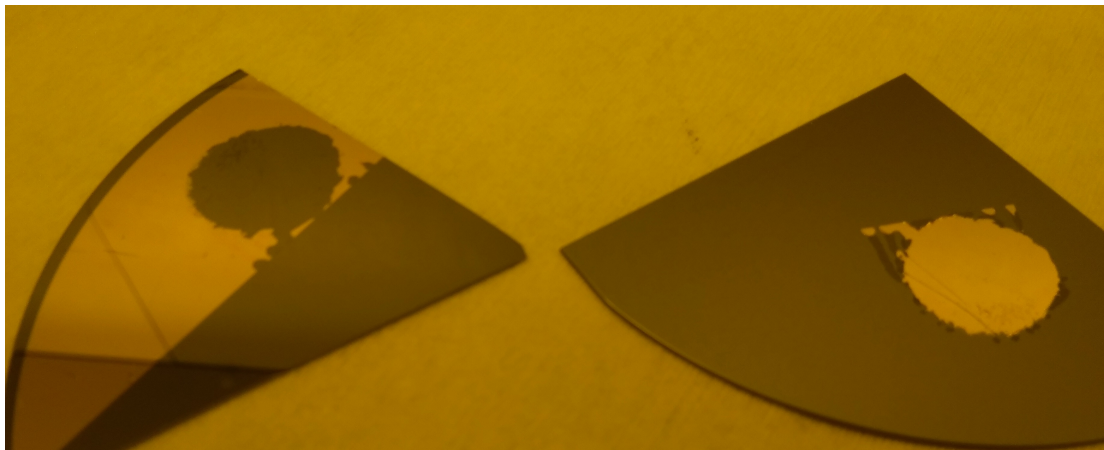


Figure 36: Template and gold film after the peel-off process.

Fig.36 show the template (on the left) and the patterned gold film (on the right) after the peel-off process. In particular, the image refers to the deposition of the epoxy manually. As it is visible, all the gold onto which the resin is deposited is completely removed from the template and transferred to the new support. The transfer is made possible thanks to the optimized value of temperature and relative interval of time for what concerns the epoxy curing process, performed inside the oven. Among the different tests performed,  $120^{\circ}C$  for  $15\text{ min}$  shows the highest transfer efficiency, reducing the probability of both adhesive and cohesive failures, thanks also to the uniform spatial distribution of the high temperature inside the oven.

## 4.2 Spiral nanostructure

Summarizing, the technique shown until now presents different advantages for the fabrication of the new generation of photoemitters:

- the use of EBL enables to fabricate nanometric templates with very high precision;
- the template stripping procedure enables to create flat surface with a roughness of the order of Angstrom;
- the template stripping enable the storage of the sandwiched structure without inducing damage or contamination to the gold surface. A fresh gold surface can be cleaved on demand from the sandwiched precursor;
- all the fabrication steps can be performed in a highly controlled environment represented by the cleanroom;

AFM measurements show a highly flat surface of the central plateau of the structure, with a r.m.s roughness of  $0.3\text{ nm}$ . Again, this new generation of photoemitter require to be as flatter as possible

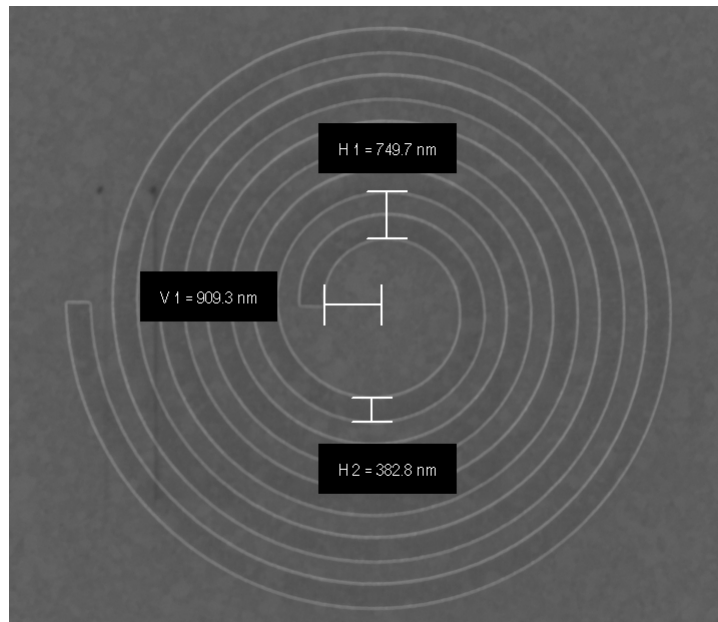


Figure 37: Final structure after the whole process fabrication.

to guarantee small angular spread in the photoemission process, reducing in this way the source transverse emittance of the electron bunch, used as a probe in future UED applications.

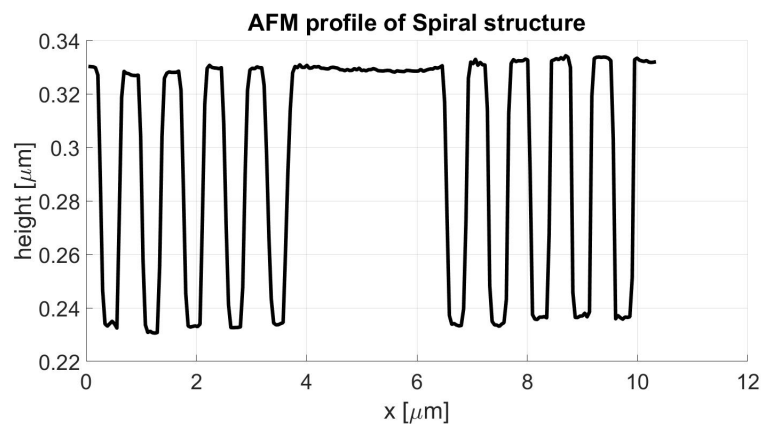


Figure 38: Depth profile of the spiral structure after the peel-off process.

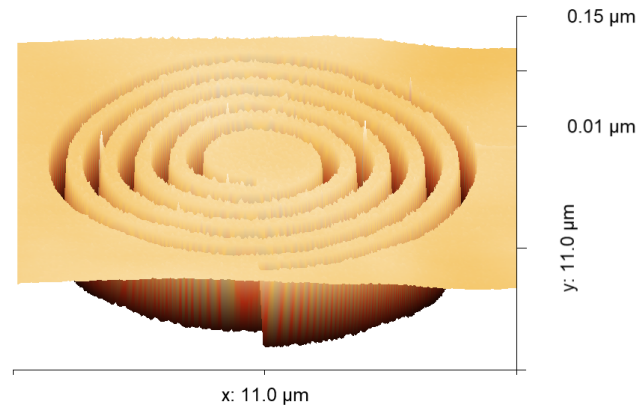


Figure 39: 3D depth profile of the final spiral structure.

The AFM depth profile show an average depth of  $90\text{ nm}$ , the resulting value of the optimization through the FDTD simulations.

## 5 Cathodoluminescence Spectromicroscopy: the reverse process

Among the possible characterization techniques used to study the plasmonic properties of metallic nanostructures, cathodoluminescence (CL) results to be one of the most interesting, offering the opportunity to resolve plasmons spectrally and spatially. Moreover, the different mechanisms of radiation excited by the primary e-beam are able to emit coherent light in the far field, leaving the possibility to further perform an angle-resolved analysis. If implemented with the right optics, a CL set-up will give the possibility to access the full polarization state of the light emission, i.e. the Stokes parameters as a function of the emission angle. In nanophotonic applications, polarization plays a fundamental role together with the directionality, in determining the interaction between the emitters and the nanostructures.

In this chapter, both CL measurements conducted on the nanofabricated spiral plasmonic lens and the FDTD simulations are presented and compared. The aim of these studies is to show the plasmonic properties of this new plasmonic lens, paying particular attention on the full polarization state of the relative far field cathodoluminescence emission.

The results will give an insight of how the plasmonic lens must be excited by the laser to fully exploit its focusing ability.

### 5.1 Theoretical background

Cathodoluminescence spectromicroscopy is a characterization technique working in contactless mode where light emitted by the sample under electron excitation is collected. One of the main advantages of this method is the ability to reach nanometric resolution without the spurious effects due to the modifications produced by the presence of a probe in the region near the sample, as in the case of near-field scanning optical microscopy (NSOM). Indeed, an electron beam is focused on the sample, leading to the excitation of different mechanisms able to emit light [9, 16]. The simultaneous involvement of radiative mechanisms is enabled by the interaction of the primary electrons with the matter, where the moving electron can be described as broadband electromagnetic source. Indeed, the spectral extent of excitation is determined by the interaction time of the electron with the sample, which is typically less than  $1\text{ fs}$ . The dimensions of the focused e-beam so as the extent of the evanescent field about the electron trajectory guarantee an interaction resolution below  $20\text{ nm}$ , depending on the beam energy. Both coherent and incoherent light can be emitted under electron excitation, giving important information about the material composition and electronic structure of the sample under investigation.

For what concerns plasmonic structures, the light emission is essentially given by the broadband generation of SPPs, where the plasmon polaritons propagate radially outward from the nanometric excitation spot and couple out to light through the grating [9, 12, 16].

In the case of the spiral, the main concept behind the choice of this characterization technique is that the light out-coupling occurs through the same grating equation that describes the conversion of circularly polarized incident laser into SPPs, i.e. the *reverse* process. The same idea is behind the CL analysis made for the bull's eye structure [12].

CL is typically performed in adapted SEMs using  $1 - 50\text{ keV}$  beams, with the possibility to record spectra for every pixel of a given image.

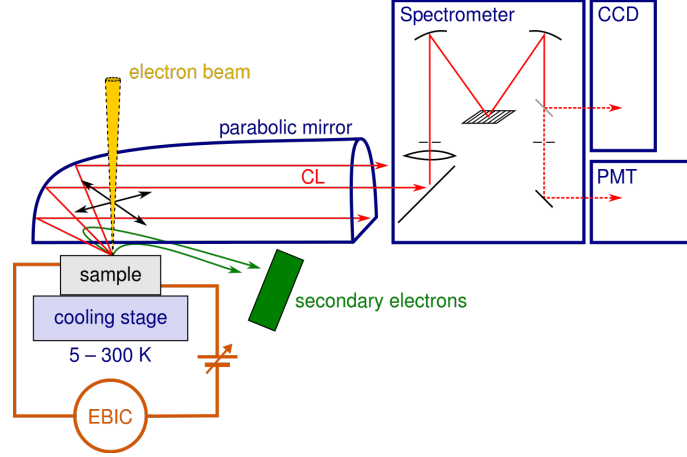


Figure 40: Schematic CL set-up, exploiting the SEM system.

The primary electron beam passes through the entrance hole in the parabolic mirror and impinges onto the sample. The structure emits light upon excitation, which in turn is reflected by the parabolic mirror and is directed toward a spectrometer, enabling the spectral analysis of the sample under investigation. Achieving precise alignment of the parabola focus and the beam path with the nanostructure is essential for collecting reproducible and well-calibrated CL data [9].

## 5.2 Cathodoluminescence Characterization

The CL measurements are performed at the Molecular Foundry with a modified Zeiss Gemini SUPRA 55 SEM. Inside the vacuum chamber, the sample is positioned at the focal point of a horizontal Al parabolic mirror with 1 mm focal length. A 10 keV e-beam is focused onto the sample and the emitted light is collected by the parabolic mirror over a wide angle range (0-80 from the normal direction) and over the entire visible spectrum and beyond. The spiral pattern is positioned with a tilting angle of 26 degrees to avoid the escape of the highly directed, normal emitted light through the entry hole in the Al mirror.

The measurements are composed of two parts. The first part consists in a scanning CL spectromicroscopic analysis, where the spectral and spatial characteristics of the surface plasmon interferences and possible resonances in the spiral patterned plasmonic lens are probed. The second part focuses on the angular distribution and the full polarization state of the CL emission, to better understand the interaction between SPPs and the emitted light.

### 5.2.1 CL spectroscopy of the plasmonic interference

In CL imaging mode, the electron beam is raster scanned over the central plateau of the fabricated spiral plasmonic lens, and a full CL emission spectrum is collected at each beam position. For this reason, it is used here to speak about CL spectromicroscopy. All the spectra are obtained by focusing the reflected light from the mirror onto a multi-mode optical fiber with 200  $\mu\text{m}$  diameter and then dispersing it using a spectrometer consisting of an Acton 2300i monochromator (150 line/mm, 500-nm blazed grating) and Andor Newton electron-multiplied CCD. The software developed to control the experiment is the open-source ScopeFoundry software module [1], available online. The dark current is subtracted and the spectra are normalized by the instrument response over the measured wavelength range.

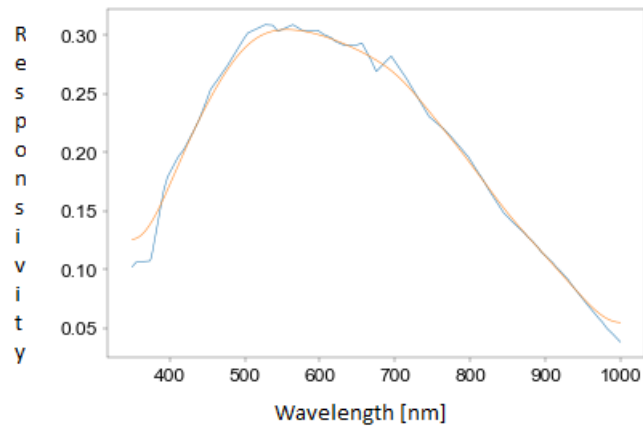


Figure 41: Instrument response of the CCD. The blue line is the response processed with MATLAB software. The red line is the corresponding fitting, made to avoid the introduction of spurious peaks in the final spatially averaged CL spectrum.

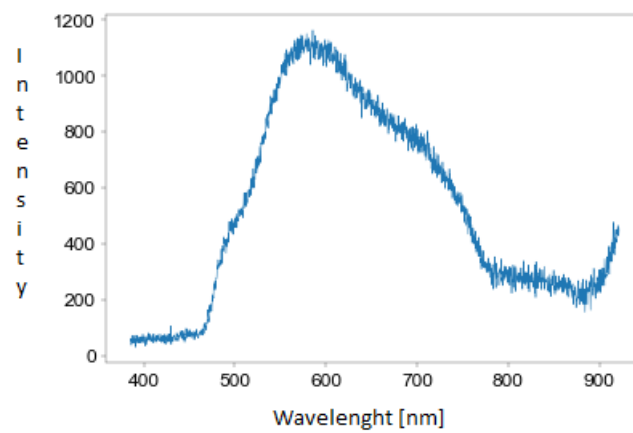


Figure 42: Corrected data for the spatially averaged CL emission spectrum, relative to region within  $65 \text{ nm}$  of the central plateau of the spiral plasmonic lens.

Fig.42 shows the corrected data for the average CL emission spectrum, computed considering only the region within  $65\text{ nm}$  of the central plateau of the spiral plasmonic lens. It is important to notice the extent of the spectral range on which the CL emission spans: this is due to the satisfaction of the grating equation by all the SPPs generated by the broadband excitation represented by the primary e-beam. Indeed, each SPP mode can couple to light for a specific emission angle, and nearly all the emission angles are collected by the Al parabolic mirror (0-80 degrees).

A huge emission peak is present close to  $550\text{ nm}$ , due to the radiative mechanism represented by the interband transition in gold starting from that wavelength [35]. A relative small emission peak is present for  $800\text{ nm}$ , for which the structure is designed to give a high enhancement of the field in the reverse process. This behaviour could be explained if a comparison with the bull's eye is taken into account (see [12]). For the bull's eye lens, designed to work at  $800\text{ nm}$ , the average CL spectrum presents a peak in the emission close to this wavelength. Here, the resonance plays a very important role, enabling a greater field enhancement with respect to the spiral lens (as seen in chapter 3). To be more precise, the resonance is here defined as the simultaneous constructive interfering of different couples of SPPs arriving from opposite directions, occurring at the center of the central plateau. Moreover, the central plateau acts as a resonant cavity, such that the field enhancement is further improved by the continuous reflections occurring at the edges of the plateau. This is not the case of the archimedean spiral pattern.

A cavity is said to be resonant for a specific wavelength, when the following condition is satisfied:

$$2L_{eff} = m\lambda_{exc} \quad m = 1, 2, 3... \quad (44)$$

$L_{eff}$  is the effective length of the cavity. The resonance occurs when the round trip distance travelled by the electromagnetic wave is equal to an integer number of the corresponding wavelength  $\lambda_{exc}$ . While in the bull's eye lens, the effective diameter of the central plateau is constant for each possible propagation direction of the inward propagating SPPs, for the archimedean spiral lens this round trip distance changes for each different direction of propagation. Indeed, the radius of the central flat surface increases linearly with the  $\theta$  angle, therefore only few specific directions will satisfy the resonance condition for a given wavelength (in this case  $800\text{ nm}$ ). In other words, reflections will occur only at specific positions, while for the bull's eye in all the positions at the groove edges thanks to its geometrical symmetry. This is the reason why it is not expected to see a huge enhancement in the hyperspectra measured in the CL imaging mode for the spiral plasmonic lens.

In the hyperspectral imaging, a three-dimensional CL intensity datacube with x-position, y-position, wavelength coordinates is collected. In other words, the entire emission spectrum for each pixel where the primary e-beam in raster scanning is measured.

To better understand the role played by the resonance in the archimedean spiral pattern, it is worth to study therefore the spatial profile of the plasmonic interferences occurring at the central plateau for different wavelengths.

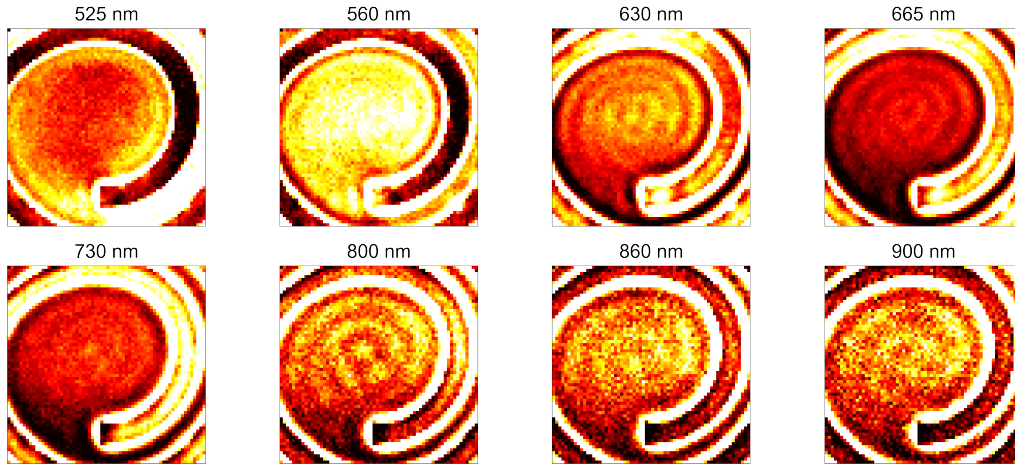


Figure 43: CL spatial maps of the lens. The maps are obtained from the spectromicroscopy dataset by intergrating over Gaussian wavelength bands with  $2\sigma = 10 \text{ nm}$ . Each map is labeled with its corresponding center wavelength.

The spatial maps for all the different wavelengths are shown applying a virtual Gaussian bandpass filter with  $2\sigma = 10 \text{ nm}$  to the entire dataset. It is possible in this way to visualize these maps over narrow spectral bands as a function of the primary beam position (fig.43). As already mentioned for fig.42, the interband transitions in gold start to arise close to  $550 \text{ nm}$ , representing here the main radiative mechanism. Indeed, for  $\lambda = 560 \text{ nm}$  the emission occurs more or less uniformly from all the region considered. Some interference patterns can be seen looking at higher wavelengths closer to  $800 \text{ nm}$ , without presenting an important CL light emission at the center of the plateau.

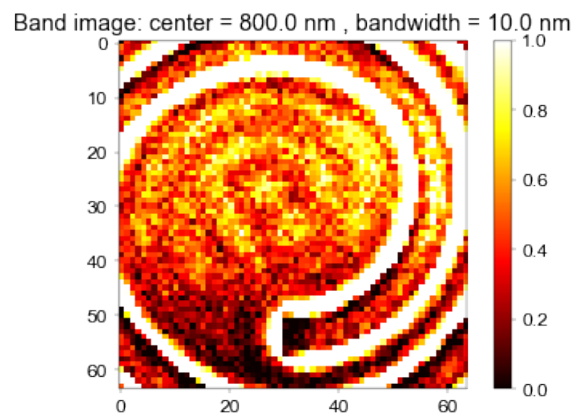


Figure 44: CL spatial map for  $\lambda = 800 \text{ nm}$ . The map shows an almost cylindrical spatial profile of the emission, with the intensity at the center comparable with the emission concentric rings. This can be attributed to the small role played by the resonances in this kind of plasmonic lens.

For  $800 \text{ nm}$ , the spatial map shows a cylindrical distribution with a maximum in the center. This profile results similar to what is observed for the bull's eye lens at the same wavelength, where the distribution is close to a zero-order Bessel function. The main difference is the relative intensity

at the central focal spot with respect to the other emission points: the spiral presents a peak in the center, with a lower contrast with respect to the other cylindrical local maxima, compared to the bull's eye. This can be again attributed to the less effective role of the resonances. Moreover, an asymmetry is present at the right lower position of the central focal spot, due to the intrinsic asymmetry of the spiral lens.

From what seen until now, one could not expect a real field enhancement localized in the center of the spiral, instead shown with the FDTD simulations, being the final aim of this plasmonic lens for focused photoemission applications. But it is important to notice that the CL profiles do not exactly correspond inversely to the achievable field enhancement expected upon laser excitation of the lens. Indeed, the CL emission maps show the *relative probability* of excitation of SPPs out-coupling to the light as a function of the e-beam position, together with the SPP generation rate by the e-beam itself. In other words, there is not exactly a correspondence one-to-one between CL emission and field enhancement, but the differences listed above must be taken into account. What can be said with certainty is that the center of the spiral result to be one of the most favorable points where constructive interferences can take place, enabling multiphoton photoemission.

Other interesting features of the CL emission maps are present in fig.43,44. At the groove edges, the emission intensity is the highest one due to the more effective radiative decoupling between the photons and the localized surface plasmons (LSPs). LSPs absorb a lot of energy as the primary e-beam scan in these zones, and then decouple at the Au-air interface acting as oscillating dipoles. In other words, the edges are strong scattering sites. But in order to be effectively excited, complex polarizations must be used under laser illumination (see Appendix [12]). Therefore, with the same argument of [12], it can be still expected to have the highest field enhancement and consequent photoemission under laser illumination at the center of the spiral lens, when the polarization considered is *circular* (this will be the matter of discussion for the second part of the CL measurements).

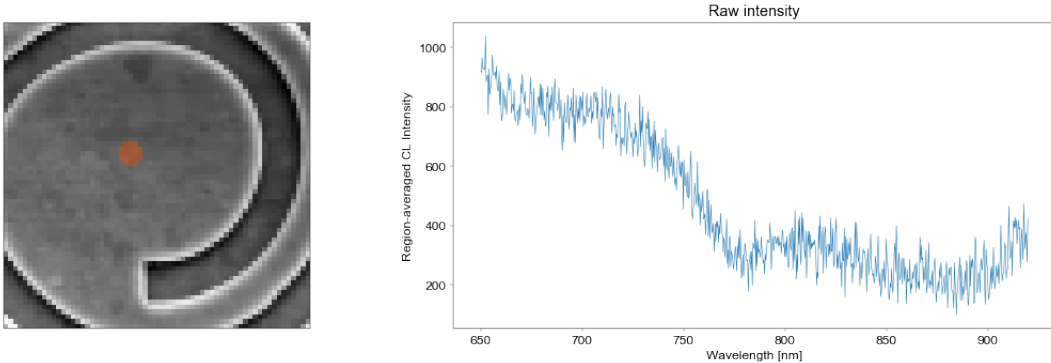


Figure 45: CL spectrum relative to the pixel labeled by the orange point. A mask is applied on the dataset in order to compute the average spectrum with respect the region indicated by the point.

Finally, fig.45 shows the average CL emission spectrum relative to the region labeled with the orange circle. A small peak in the spectrum is visible closed to  $800\text{ nm}$ . The reasons advanced for thess results are the same explained so far in this paragraph.

### 5.2.2 Angle-resolved CL imaging polarimetry

The second part presents the measurements relative to the angle-resolved CL emission polarimetry. In particular, the aim is to show that the structure is able to emit light normal to its surface with

a high degree of *circular polarization*, demonstrating that the most efficient photon-plasmon coupling can be reached with a circularly polarized illumination for  $800\text{ nm}$ . Here, both the FDTD simulations and the measurements for the 5-turns archimedean spiral plasmonic lens are described. The far field CL emission is taken into account, where Fourier imaging is exploited. Since the far field of the emission is the Fourier transform of its spatial profile at the sample, it is possible to infer the radial extent of the photon-plasmon coupling.

The far field CL emission is obtained positioning the primary e-beam at the center of the spiral. With the integration of the right optics to the SEM set-up, it is possible to angle-resolve the full polarization state of the far field CL emission.

The parabolic mirror brings the emission to infinity focus, where it is filtered by a bandpass filter centered at  $800\text{ nm}$  with  $40\text{ nm}$  bandwidth and then is magnified and imaged onto a Thorlabs DCC3260M CMOS camera.

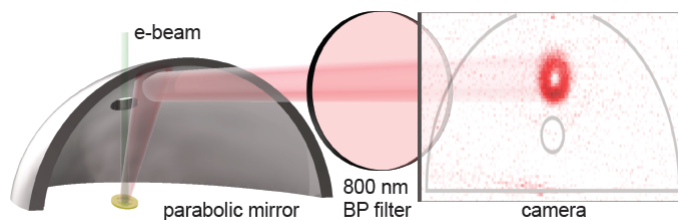


Figure 46: Schematic plot of the far field CL set-up [12]. To perform CL imaging polarimetry, the integration of rotating-plate polarimeter in the detection path is required.

If the mirror is well-focused, each point in the CMOS camera corresponds to light reflected off a single point of the Al parabolic mirror and corresponds to a unique emission angle described by a zenithal angle  $\theta$  running from  $0^\circ$  to  $90^\circ$  ( $0^\circ$  is normal to the surface) and an azimuthal angle  $\phi$  running from  $0^\circ$  to  $360^\circ$  (where the paraboloid vertex is at  $180^\circ$ ) [9, 36].

CL imaging polarimetry can be performed thanks to the integration of a rotating-plate polarimeter in the detection path of the angle-resolved CL set-up, following the same modus operandi of [36].

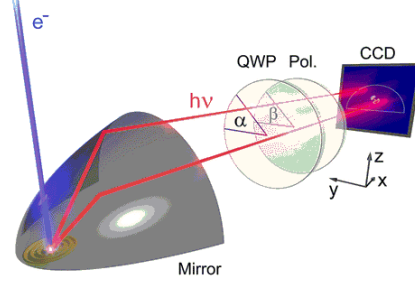


Figure 47: CL imaging polarimetry set-up [36]. The intergration of a QWP and a linear polarizer is shown. In the current experimental set-up, the sample is tilted of  $26^\circ$ . The bandpass filter centered at  $800\text{ nm}$  is not depicted here.

The full polarization state of the CL emission can be known once the Stokes parameters as a function of the emission angle are defined. The Stokes vector is a general representation of the polarization state of the light. It can be used for incoherent, partially or completely polarized light. Moreover, the effect of an optical system on the polarization of light can be determined by constructing the Stokes vector for the input light and applying the Mueller calculus, to obtain the Stokes vector of the light leaving the system. In particular, the Stokes vector is defined in the following way:

$$\vec{S} = \begin{bmatrix} S_0 \\ S_1 \\ S_2 \\ S_3 \end{bmatrix} = \begin{bmatrix} I_{0^\circ} + I_{90^\circ} \\ I_{0^\circ} - I_{90^\circ} \\ I_{45^\circ} - I_{135^\circ} \\ I_{RHC} + I_{LHC} \end{bmatrix} \quad (45)$$

$S_0$  represents the overall intensity of the emitted light;  $S_1$  represents the difference of intensity transmitted by a linear x-polarizer and a linear y-polarizer;  $S_2$  the difference of intensity transmitted by a  $45^\circ$  and  $-45^\circ$  oriented linear polarizers;  $S_3$  the difference in intensity transmitted by a right-handed circular (RHC) polarizer and a left-handed circular (LHC) polarizer.

Some important relations exist among the various Stokes parameters. In the most general case,

$$S_0^2 \geq S_1^2 + S_2^2 + S_3^2 \quad (46)$$

While the last three Stokes parameter can be not null only if the light is at least partially polarized, the first Stokes parameter is always different from zero, unless the trivial condition in which no light source is present. Therefore, if the Stokes vector is given, it is possible to know also the degree of polarization:

$$g = \frac{\sqrt{S_1^2 + S_2^2 + S_3^2}}{S_0} \quad (47)$$

In a straightforward way, it is also possible to define one of the most fundamental quantities for the current analysis, i.e. the *degree of circular polarization* (DOCP):

$$DOCP = \frac{S_3}{S_0} \quad (48)$$

In principle, the Stokes parameters can be measured experimentally positioning along the detection path of the angle-resolved CL set-up three elements: a bandpass filter centered at  $800\text{ nm}$  with  $40\text{ nm}$  bandwidth; a linear polarizer (LP) whose polarization axis orientation can be changed; a quarter-wave plate (QWP). The role of the first element is to eliminate any spectral component far from  $800\text{ nm}$ . It must be always present on the detection path. The second element enables the determination of the first three Stokes parameters. The third element must be always coupled with two different configurations of the linear polarizer, such that  $I_{RHC}$  and  $I_{LHC}$  can be separately determined (a schematic example of the required integration of these optics is shown in fig.47). Therefore, it is measured the intensity transmitted by six different settings of the polarizer: LP at  $0^\circ$ , LP at  $90^\circ$ , LP at  $45^\circ$ , LP at  $135^\circ$ , QWP with the fast axis at  $45^\circ$  coupled with a LP at  $0^\circ$  before, and with a LP at  $90^\circ$  after.

For each measurement, 30 one-second exposures of the CCD are acquired and averaged. At the beginning, background image obtained blanking the beam is acquired under the same conditions and successively subtracted from the ON-beam images. After, each pixel in the image is mapped to an emission angle, and the signal is normalized by the solid angle collected by the pixel to give an intensity map. Finally, the measured far field is then corrected for tilt and rotation of the sample with respect to the mirror.

In the following, the measured intensities for the six different settings are analyzed. For sake of simplicity, each specific polarization is compared with the relative orthogonal one. All these measurements are performed for different spirals, showing almost an identical behaviour.

The first two polarizations considered are related to the use of the linear polarizer with the polarization axis at  $0^\circ$  and  $90^\circ$ .

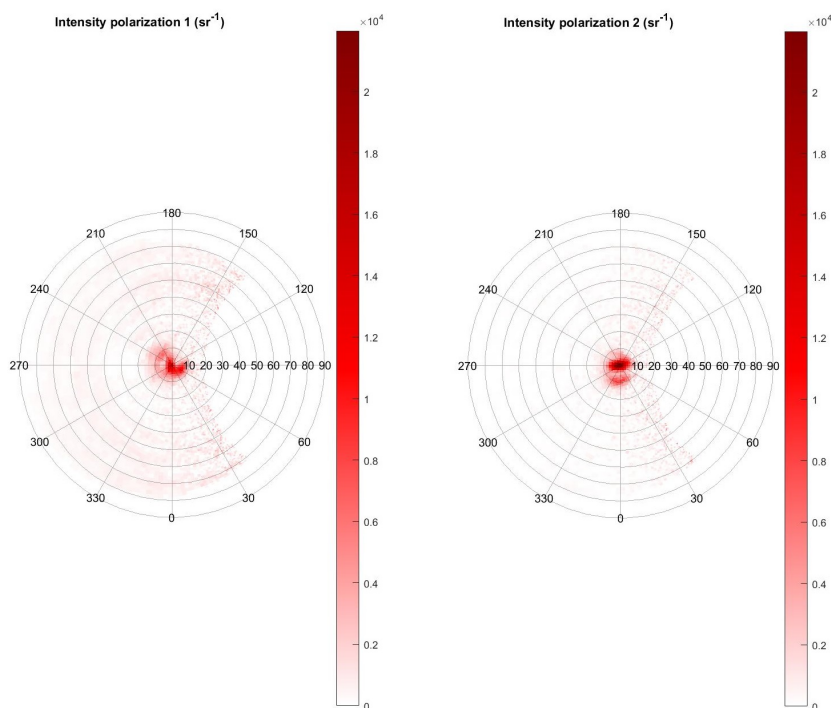


Figure 48: Left: far field CL emission with linear polarizer at  $0^\circ$ . Right: far field CL emission with linear polarizer at  $90^\circ$ . The orthogonality is visible looking at the shape of the CL emission.

The two far field CL emissions result to present complementary shapes, due to the fact they are characterized by opposite polarization. While the emission on the right presents a vertical distribution, i.e. the azimuthal angle  $\phi$  assumes values closed to  $0^\circ$  and  $180^\circ$ , with a huge intensity peak for a zenithal angle  $\theta \leq 5^\circ$ , the emission on the left is distributed more horizontally ( $\phi$  closer to  $90^\circ$  and  $270^\circ$ ), with a smaller intensity for the same range of values of the zenithal angle  $\theta$ . The same analysis can be carried out for the other couples of orthogonal polarizations.

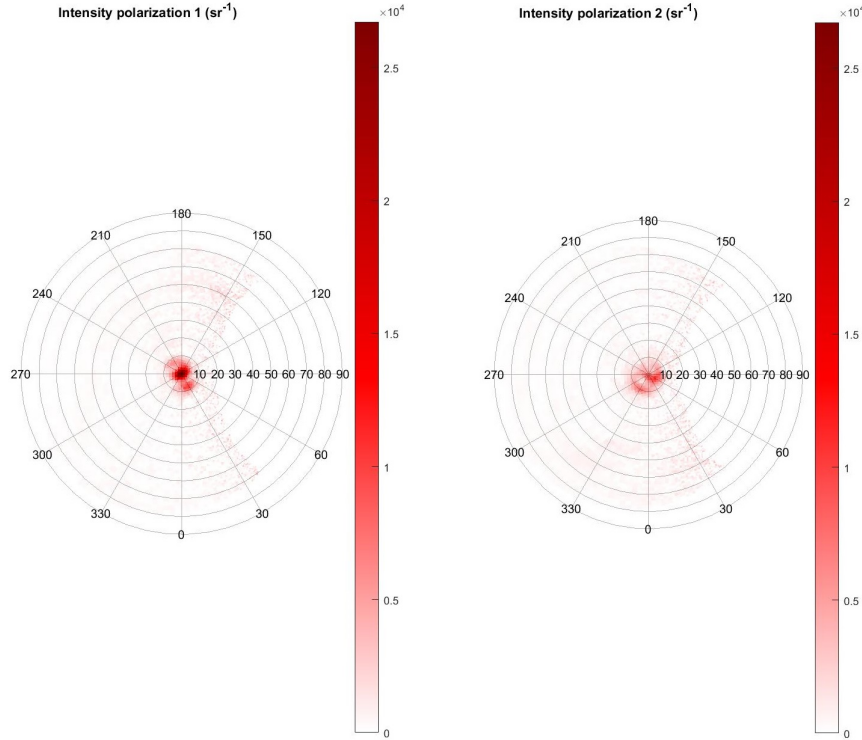


Figure 49: Left: far field CL emission with linear polarizer at  $45^\circ$ . Right: far field CL emission with linear polarizer at  $135^\circ$ .

In fig.49, the emission on the left is distributed in such a way that  $\phi$  is closer to  $60^\circ$  and  $210^\circ$ , with a huge peak for  $\theta \leq 5^\circ$ , while the emission on the right present an intensity distribution for  $\phi$  is closer to  $150^\circ$  and  $330^\circ$ , with a smaller intensity peak for the same range of  $\theta$ . It is worth to notice that the simultaneous presence of an intensity peak for the emission angle in both the two orthogonal polarization distributions suggests the presence of a circular polarization. Indeed, the circular polarization can be described as the superposition of two orthogonal linear polarizations ( $0^\circ$ - $90^\circ$  or  $45^\circ$ - $135^\circ$ ), with a time delay of  $\pi/2$ . Therefore, both the two linear components are present. The same can be said for the right-handed and left-handed circular polarizations. Their detection is performed integrating the QWP at  $45^\circ$  in the detection path, before the LP (see fig.50). If a circular polarization is present, as the light meets QWP, it is converted in a vertical or horizontal linear polarization depending on its chirality, due to the phase delay introduced between the ordinary and extraordinary axis at the QWP. Once the circular polarization is converted in linear one, light will arrive or not on the CMOS camera (after having passed through the bandpass filter), depending on the orientation of the polarization axis of the LP considered.

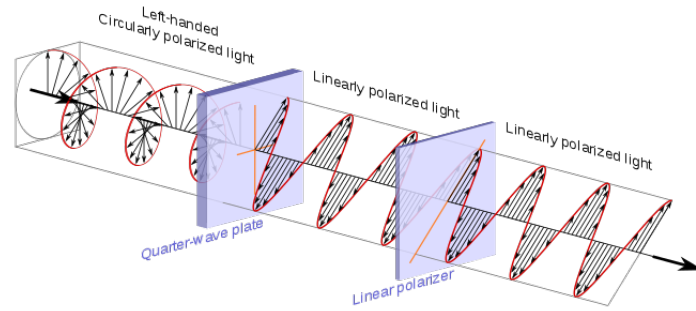


Figure 50: Schematic image of the detection of circularly polarized CL emission.

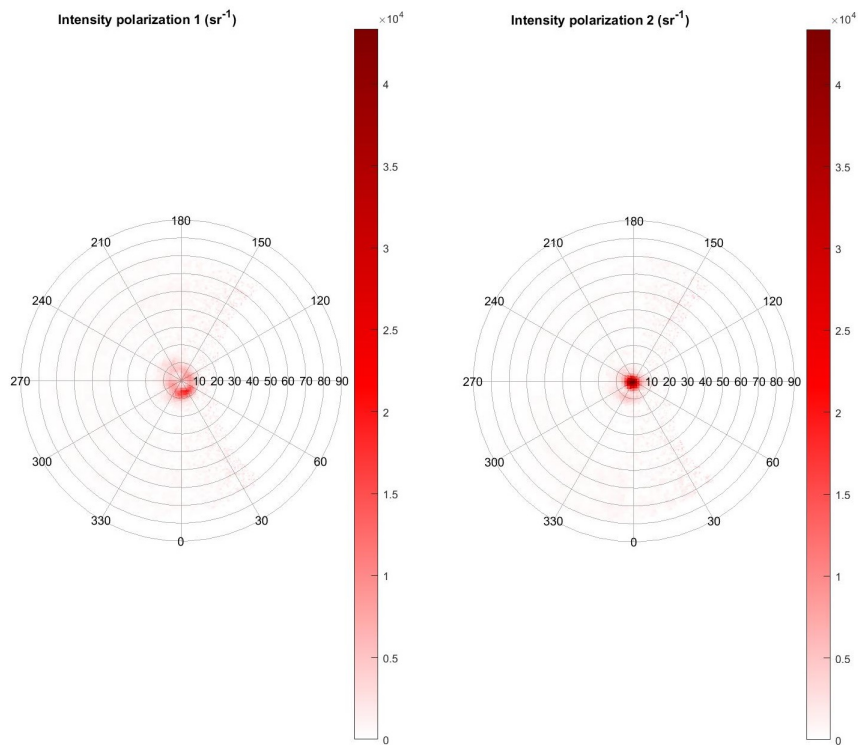


Figure 51: Left: far field CL emission with QWP having the fast axis oriented at  $45^\circ$  respect to the horizontal line of the parabolic mirror, coupled with a LP at  $90^\circ$ . Right: far field CL emission obtained with the same QWP coupled with a LP at  $0^\circ$ .

The two distributions result again orthogonal, as expected. In particular, the CL emission on the right presents a huge intensity peak for  $\theta \leq 5^\circ$ , with a uniformity for the azimuthal angle  $\phi$ . On the contrary, the CL emission on the left shows an intensity distribution with a donut shape, with a minimum for  $\theta \leq 5^\circ$ . This means that the spiral lens is essentially emitting normal to its surface a specific circular polarization (LHC or RHC). It is therefore expected to have a high degree of circular polarization.

The alignment of the optics is of fundamental importance in this experimental set-up, since a misalignment can distort the intensity distributions, making all the data unuseful for the final purpose of the current analysis.

The quality of the alignment can be checked by summing up the couples of orthogonal polarizations and comparing them among each other. If the optics alignment is well performed, ideally all these total intensities must be the same, i.e. same shape and values for the different emission angles. Indeed, each couple (LP at  $0^\circ$ - $90^\circ$ , LP at  $45^\circ$ - $135^\circ$  and QWP at  $45^\circ$  plus LP at  $0^\circ$  and  $90^\circ$ ) forms a complete basis, able to represent the far field CL emission coming from the plasmonic lens excited with the primary e-beam impinging in the center of the spiral. In other words, the total intensity distribution is ideally unique, and we have three basis to represent it.

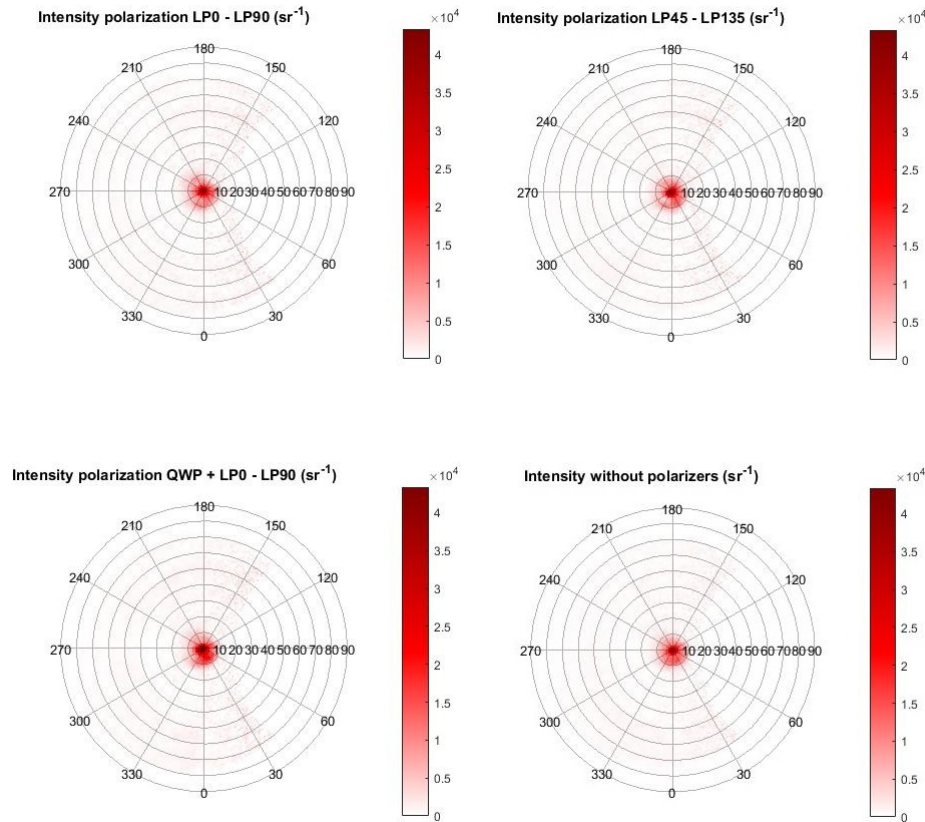


Figure 52: Comparison of the different total intensities.

Fig.52 shows the different total intensities. They present almost the same shape, meaning that

all the different optics are well positioned along the detection path, going from the Al parabolic mirror to the CMOS camera. On the contrary, they present not exactly the same values of intensity, but some of them result to be attenuated. This phenomenon is due to the fact that the different measurements are performed in different times. The 10 keV primary e-beam introduces some distortions on the flat surface of the central plateau for each new measurement, leading to a weakening of the emitted light. In particular, the measurement were performed in the following timeline: first, QWP plus LP, second LP at 0° and 90°, third, LP at 45° and 135°, finally, total intensity measured with just the bandpass filter centered at 800 nm. This explains why the total intensity without polarizers results to be the weakest one. Theoretically, each added optics introduces some losses of the whole signal. Therefore, among the four intensities, the last should result the brightest one. The non-idealities of the technique are beyond this counter-intuitive phenomenon.

Finally, it is interesting to notice that the emission angle  $\theta$  found is approximately close to 5°, that correspond to the grating equation:

$$\theta = \sin^{-1} \left( \frac{k_{spp} - m \frac{2\pi}{d}}{k_0} \right) \quad (49)$$

where  $m$  is the grating order,  $k_0 = 2\pi/\lambda_{exc}$  and  $k_{spp}$  the SPP wavevector. The theoretical value computed for  $k_0 = \frac{2\pi}{800} 10^9 \text{ m}^{-1}$ ,  $k_{spp} = \frac{2\pi}{783} 10^9 \text{ m}^{-1}$  and  $d = 750 \text{ nm}$  and  $\lambda_{exc} = 800 \text{ nm}$  is  $\theta \simeq 4.5^\circ$ , showing good agreement with the experimental results.

All the measurements presented until now were performed for different spiral lenses, characterized by the same geometrical dimensions defined in chapter 3 and 4, with some degrees of tolerance.

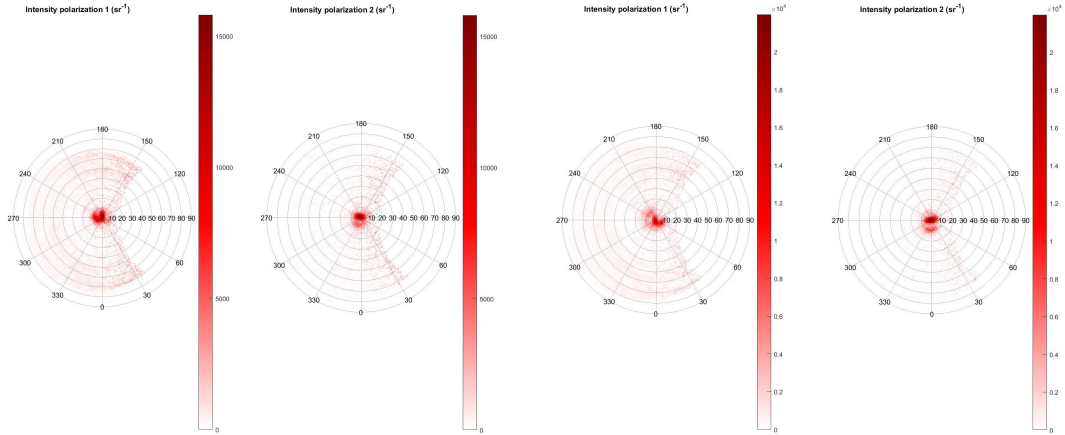


Figure 53: Intensity comparison with LP at 0° and 90° for two spiral plasmonic lenses fabricated in the same way.

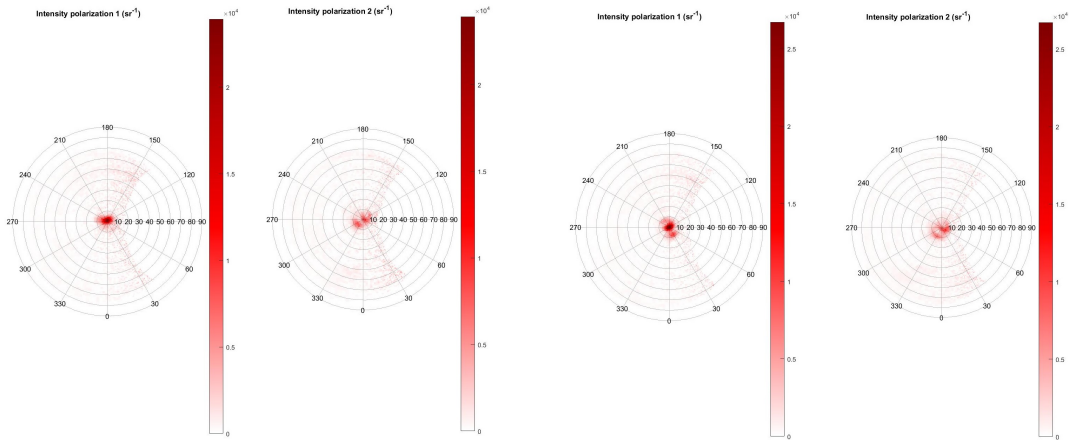


Figure 54: Intensity comparison with LP at  $45^\circ$  and  $135^\circ$  for two spiral plasmonic lenses fabricated in the same way.

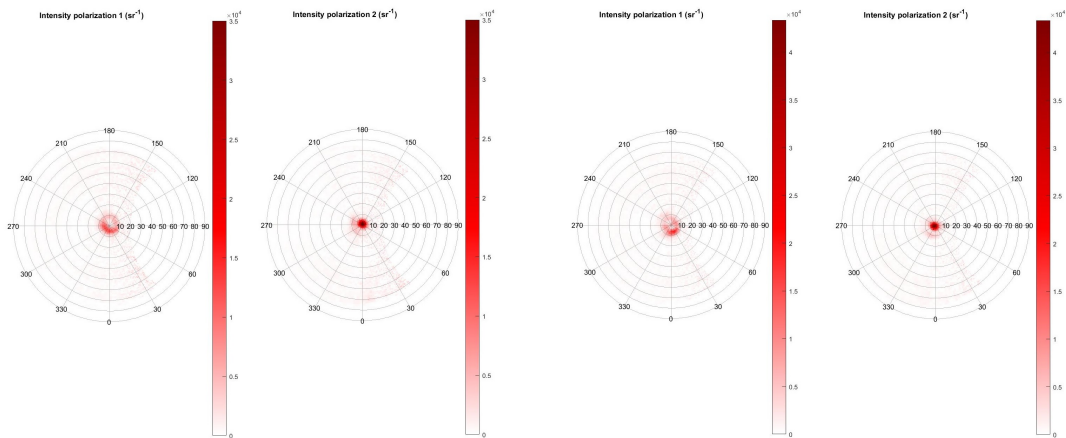


Figure 55: Intensity comparison with QWP at  $45^\circ$  plus LP at  $0^\circ$  and  $90^\circ$  for two spiral plasmonic lenses fabricated in the same way.

Fig.53,54,55 show some differences in terms of intensity values than in the shape. These differences can be attributed to the tolerances and variations related to the fabrication process of the two plasmonic lenses. The most important thing that must be evidenced is that they present almost the same shapes for all the six different settings, enabling us to confirm the robustness of the fabrication process used for the nanostructures.

With all these data, it is possible to determine important figures of merit like the DOCP. We are essentially interested in DOCP since we want to know if the structure is able to emit circularly polarized light normal to the flat surface due to the photon-plasmon coupling. If this is the case, this will mean that the most effective way to exploit this coupling in the reverse process is to use a circularly polarized laser, impinging normally to the plasmonic lens (see Appendix for the DC-gun set-up, where the lens must be mounted). In this way, we will be able to fully exploit the lens and its focusing ability, fundamental for multiphoton photoemission applications as in UED.

To improve the confidence about the validity of the measurements, FDTD simulations were performed and compared with the experiments.

The CL process is numerically modeled with the FDTD Lumerical solver, where the  $10\text{keV}$  primary e-beam at the center of the spiral was defined using a series of dipoles normal to the surface. As already stated above, an electron can be seen as a broadband evanescent field source. Therefore, the different dipoles were delayed in phase to create a propagating, localized source of electric field. The electron velocity is directly related to this phase delay. In this way, it is possible to simulate a current density dependent both on time and the vertical spatial coordinate  $z$  [6]:

$$\vec{J}(t, z) = -ev\hat{z}\delta(z - vt)\delta(x - x_0)\delta(y - y_0) \quad (50)$$

$e$  is the elementary charge,  $v$  is the electron velocity,  $\hat{z}$  the unit vector,  $x_0$  and  $y_0$  the coordinates of the lateral position of the beam (set to 0 in the Lumerical code). Thanks to this design, the resulting electric field produced by the series of dipoles is decaying laterally, and vanishes within few nm in the metal. In this way, no field is directly coupling to the grooves, but the simulated CL emission is only due to the generation, propagation and outcoupling of the SPPs. Moreover, a raised-cosine filter was used in the simulations to avoid the abrupt appearance and disappearance of the electric field. The filter had the aim to gradually increase and decrease the amplitude of the generated electric field at the starting and ending dipoles in time.

Different quantities were monitored with Lumerical, to compare with the experimental results.

Fig.56,57 shows the FDTD simulated and experimentally measured emitted CL power versus the  $\theta$  angle, respectively. It is interesting to see the agreement for the emission angle relative to the highest peak of the emitted power (close to  $5^\circ$ ). Furthermore, they present almost the same trend in the whole range of values of  $\theta$ . The value of the simulated power results quite small, due to the position of the monitor during the simulations, far from the sample surface.

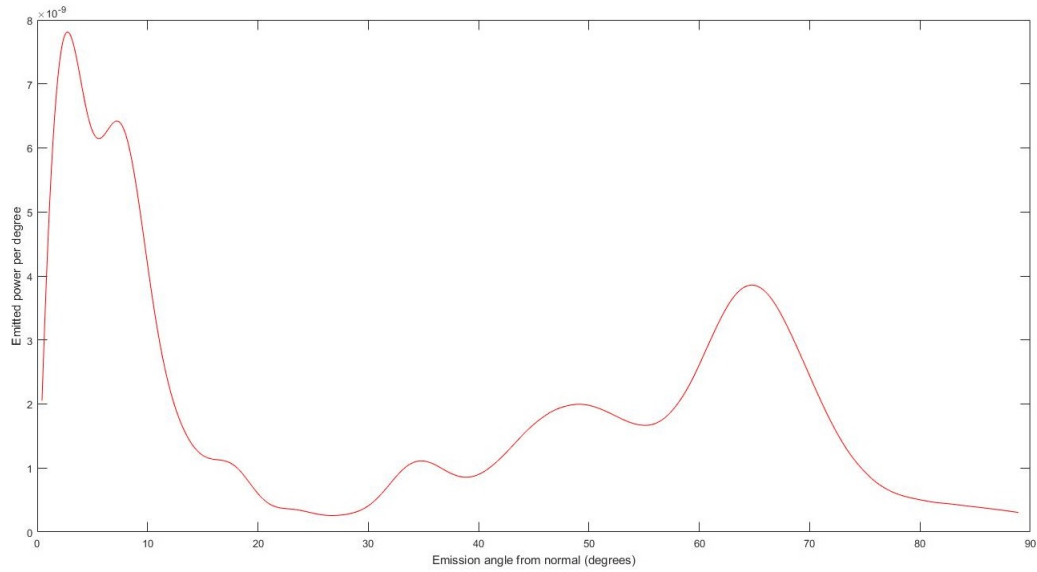


Figure 56: FDTD simulated emitted CL power per degree vs the zenithal angle  $\theta$ .

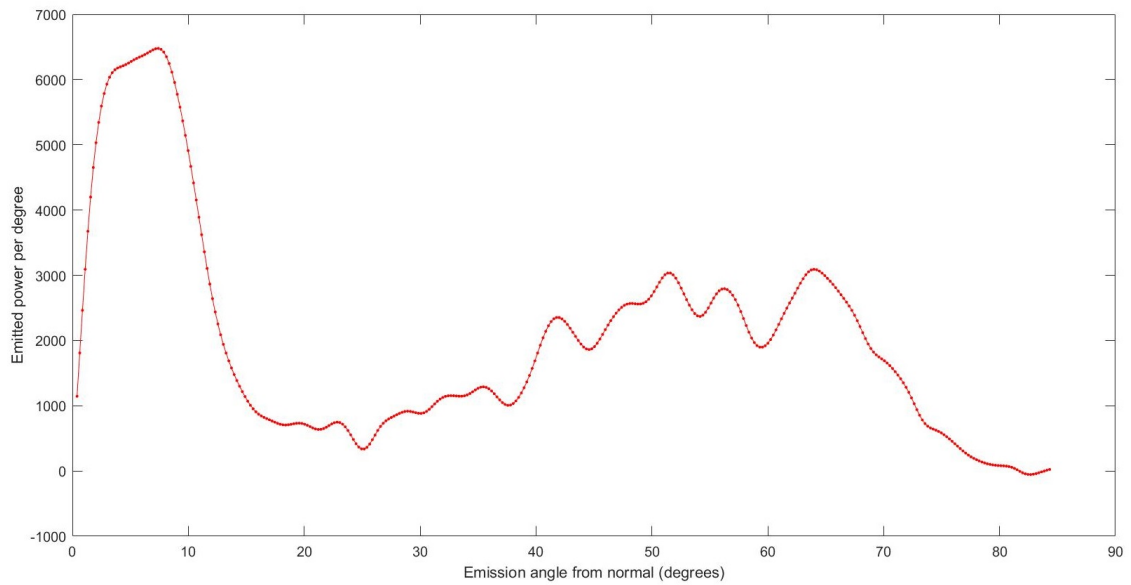


Figure 57: Experimental emitted CL power per degree vs the zenithal angle  $\theta$ .

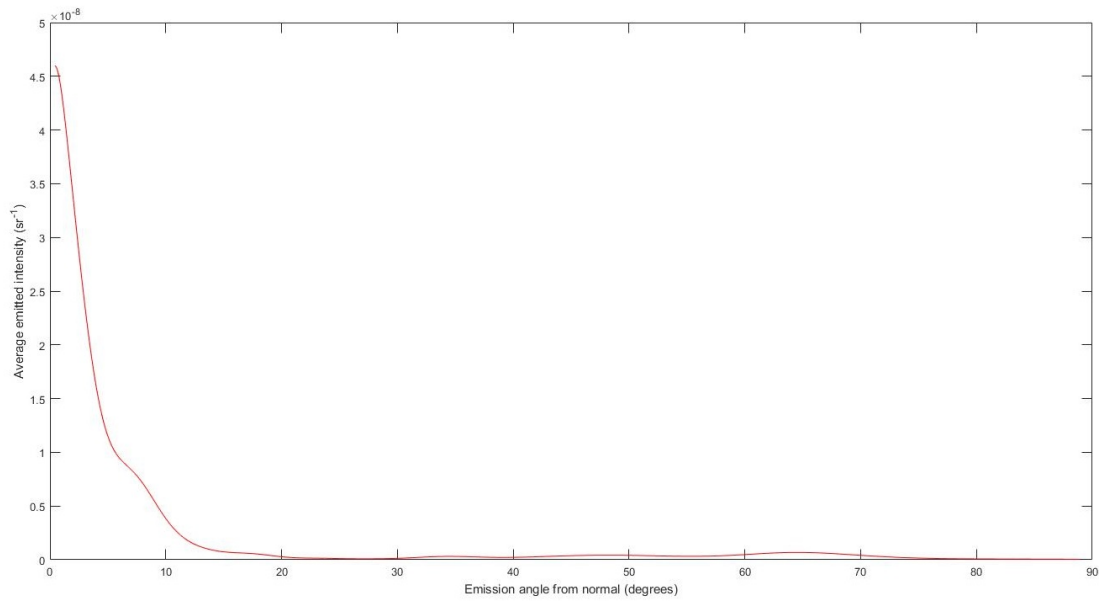


Figure 58: Average CL emission intensity simulated with FDTD Lumerical solver.

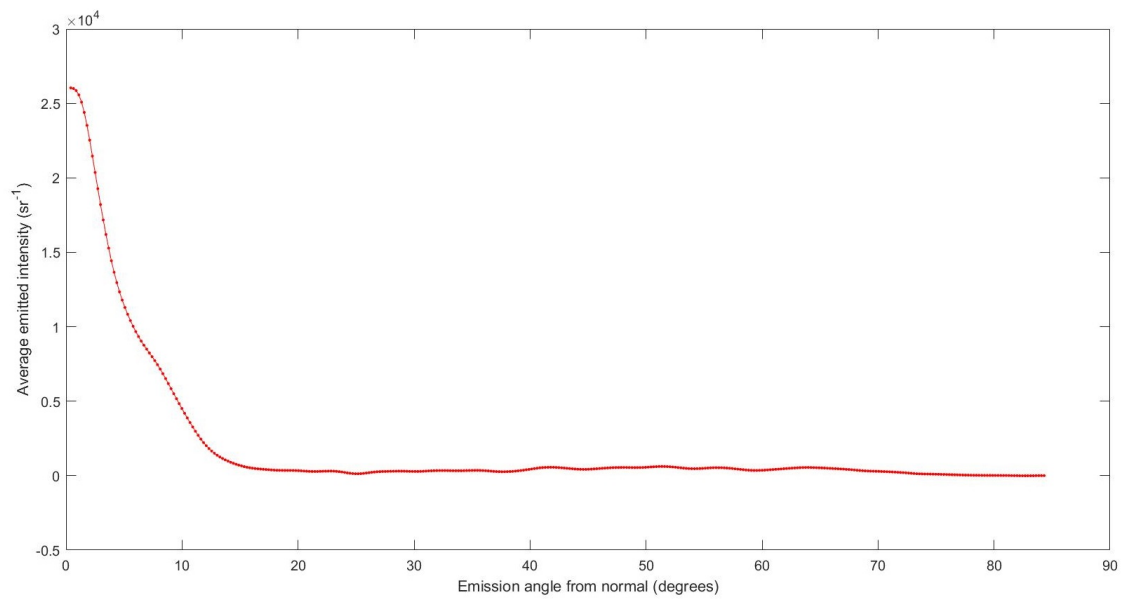


Figure 59: Average CL emission intensity measured with the CL set-up.

A good agreement can also be seen for what concerns the average emitted intensity per degree of the  $\theta$  angle between FDTD simulations and experiments (fig.58,59).

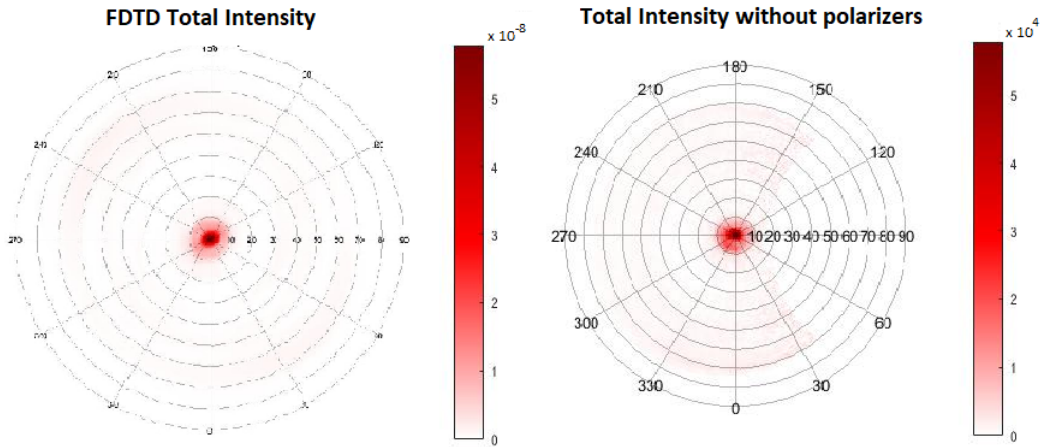


Figure 60: Left: FDTD simulated CL emission distribution. Right: Experimental CL emission distribution, obtained with only the bandpass filter along the detection path.

Fig.60 shows the intensity distributions for CL emission simulated with Lumerical and the measured data. They present the same shape but with a different orientation with respect the azimuthal angle  $\phi$ . This is due to the fact FDTD simulations were run with a different disposition of the spiral pattern with respect to the FDTD monitor considered, without reproducing the exactly angular relation present for the experimental set-up, between spiral, mirror and CMOS camera. Anyway, the shape confirm the good agreement between the simulated and experimentally found distributions.

Finally, the DOCP is computed for both FDTD simulations and experimental data.

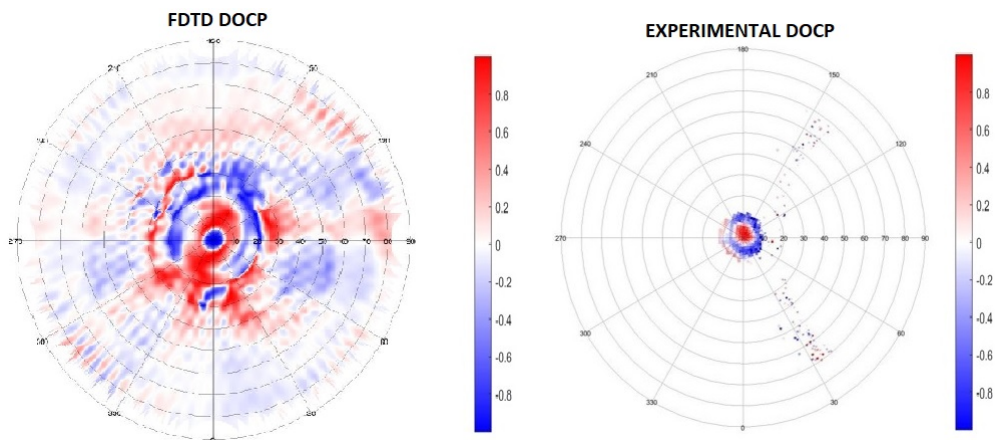


Figure 61: Left: DOCP of the FDTD simulated CL emission. Right: DOCP of the experimental CL emission.

It is important to notice that in the experimental DOCP, the CL emission coming from a zenithal

angle  $\theta \leq 5^\circ$  present a high DOCP, whose chirality is the opposite of the spiral plasmonic lens under investigation. For what concerns the comparison between the FDTD simulations and the experimental results, the two DOCPs present the same shape, but different orientation with respect to the azimuthal angle  $\phi$ , and opposite chirality of the circular polarization. Again, the reason is linked to the relative position of the spiral, on one hand, with respect to the frequency monitor in Lumerical, and on the other hand, with respect to the mirror and the CMOS camera. Moreover, the FDTD simulations were performed considering a spiral pattern of the same geometrical dimensions of the fabricated one, but with opposite chirality. This finally explains the major differences. Therefore, apart from these, it is possible to confirm again the good agreement between the FDTD simulations and the experimental data.

The most important result on which it must be paid attention is that the CL emission coming from the structure with a normal direction to the flat surface presents a high degree of circular polarization. This means again that working in the opposite condition, i.e. illuminating the plasmonic lens with a laser, the most effective photon-plasmon coupling will occur if the laser presents a circular polarization, always with a chirality opposite to the spiral one.

## 6 Conclusions

This work developed at the Molecular Foundry (LBNL) focused on the design, fabrication and characterization of a new plasmonic lens for the new generation of photoemitters. In particular, the project aimed to fabricate a structure able to focus the impinging electromagnetic light in a sub-wavelength nanometric spot at its center. The plasmonic structure bases its focusing ability on the interference of surface plasmon polaritons propagating inward toward the center of the lens. Their excitation occur thanks to a coupling between a circular polarized pulsed laser and the spiral grating, able to supply the required extra-momentum.

This focusing ability is mandatory to satisfy the requirements on the quality of the electron bunches used as pulsed probes for ultrafast electron diffraction. Essentially, the emission occurs from a flat surface, reducing the angular spread of the extracted electrons, and the relative emission area is drastically reduced thanks to the focus of the electromagnetic energy by means of the surface plasmon polaritons. These 2D standing waves allow to concentrate the light beyond the diffraction limit, reaching and overcoming the threshold for non-linear optical phenomena as the multiphoton photoemission, occurring at high intensity regimes. There exists an intensity threshold after which the multiphoton absorption present higher yield than the single-photon process, increasing the final quantum yield usually very low for metals in the UV range [34].

One structure has been studied for the present work, in two different configurations: the spiral plasmonic lens in reflection and transmission configuration. This works follows the way paved by A.Polyakov, D.Durham and F.Riminucci at the Molecular Foundry for the design and the fabrication for new photoemitters for UED applications.

The spiral allows to focus the light at its center if the laser is circularly polarized. This point is of fundamental importance since it is main reason behind this work. Indeed, the bull's eye structure [12, 44] requires a radially polarized laser to be fully exploited. Therefore, the laser alignment is a crucial experimental step, made difficult by the fact that the photocathode must be mounted inside a vacuum chamber. Requiring only for a circular polarization makes easier the focus of the laser on the metal photocathode, which is still able to focus electromagnetic energy in a region smaller than 200 nm.

Once designed and optimized, the lens was fabricated with the template stripping (TS) process, guaranteeing a flat surface of the central plateau of the spiral with a roughness of the orders of the Angstrom (3 Å). Different procedures were tested with the TS process to understand the possibilities for improvements of the quality of the final structure. In this works, the overall best reliability resulted to be given by the manual deposition of epoxy resin, followed by the curing inside the oven.

The fabricated spiral plasmonic lenses were finally characterized through atomic force microscopy (AFM) and cathodoluminescence (CL). In particular, the far field analysis of the CL light emission showed interesting results about the light-plasmon coupling occurring at the center of the pattern, evidencing the need to use a circular polarization for the excitation of the surface plasmon polaritons to fully exploit the focusing ability of this plasmonic lens.

### 6.1 Future perspectives

Further studies will concern both the fabrication and characterization of the realized spiral structures. In particular:

- chemical peel-off process: it is performed inside a solvent, reducing the probability of mechanical stress or scratches introduced during the mechanical cleavage of the template;
- test of this photocathode inside the DC electron gun experimental set-up built during the

work at the LBNL;

- improvement of the DC electron gun set-up;
- test of the photocathode under high repetition rate [14] and ultrafast laser pulses [34] for UED experiments;
- fabrication of the spiral plasmonic lens in transmission configuration with the FIB system.

## APPENDICES

### A Experimental set-up: DC-gun beamline

The present work looks for the fabrication of a new generation of photoemitters, with particular attention for UED applications. For this purpose, the final test bench for the spiral plasmonic lens is to implement it in a DC electron gun set-up to verify the photoemission properties of the fabricated photocathode.

During this work, a DC electron gun beamline was built in Building 2 at the Advanced Light Source (ALS) Facility (LBNL) with this aim.

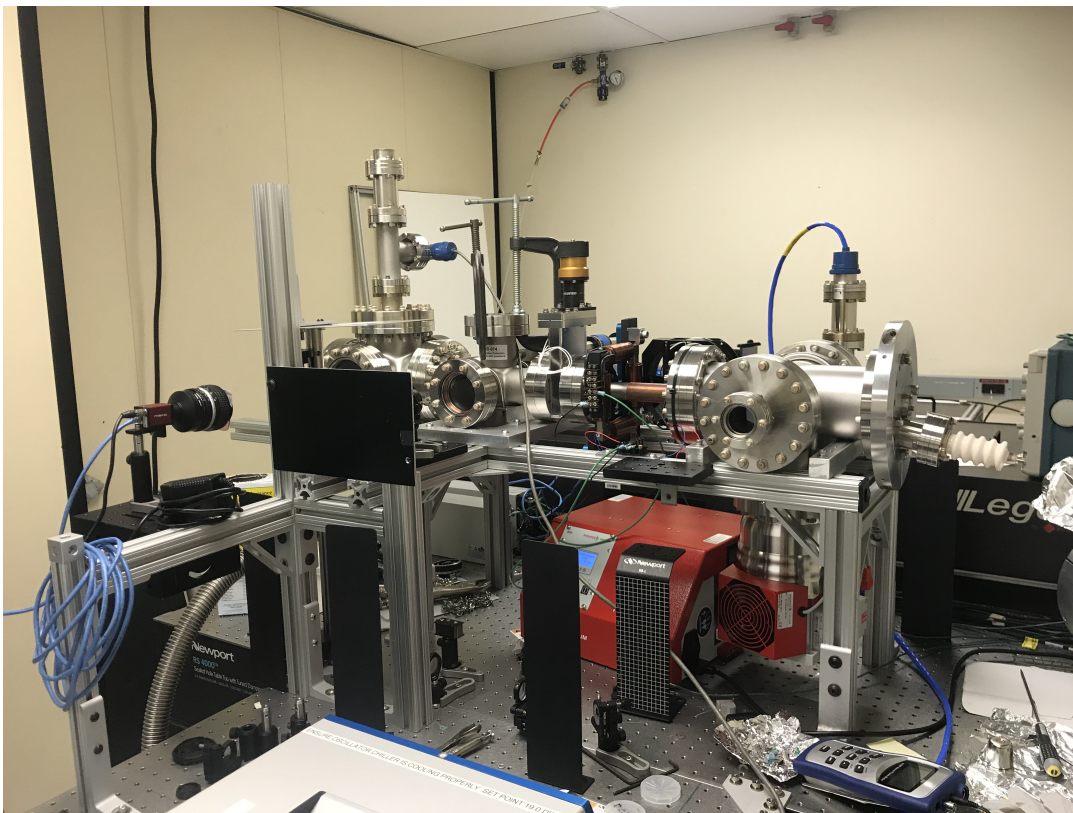


Figure 62: DC electron gun beamline in Building 2 at the ALS Facility.

Fig.62 shows the whole DC electron gun set-up. The entire beamline works in ultra-high vacuum (UHV) conditions. The pulsed laser enters inside the vacuum chamber through a sapphire window and electrons should be produced from the DC photocathode (for the first photoemission tests, a flat piece of copper was used) and accelerated by the electric field. If extracted, electrons will be focused by a solenoid and deflections of their trajectory can be applied by means of dipole magnets. Then, the detection of photoemission is performed through a YAG scintillator screen and a Faraday cup, positioned at the end of the beamline.

## A.1 Vacuum chamber

Working in UHV conditions is of fundamental importance for two main reasons in this experimental set-up. The first reason is to avoid the breakdown condition at the electron gun, whose probability increases for the presence of contaminants. The second one is to guarantee a long enough mean free path to the extracted electrons and reduce the scattering probability to perform the detection. The UHV condition ( $10^{-7}$  torr) is reached with a compression pump to obtain the medium or high vacuum, followed by activation of a turbomolecular pump (HiCUBE 80 ECO PFEIFFER) to maintain the ultra-high vacuum. An ion gauge pump is connected directly to the electron gun chamber as well. Moreover, all the coupling between components need to be hermetically sealed.

## A.2 DC electron gun

The first and main component of the present set-up is the DC electron gun.

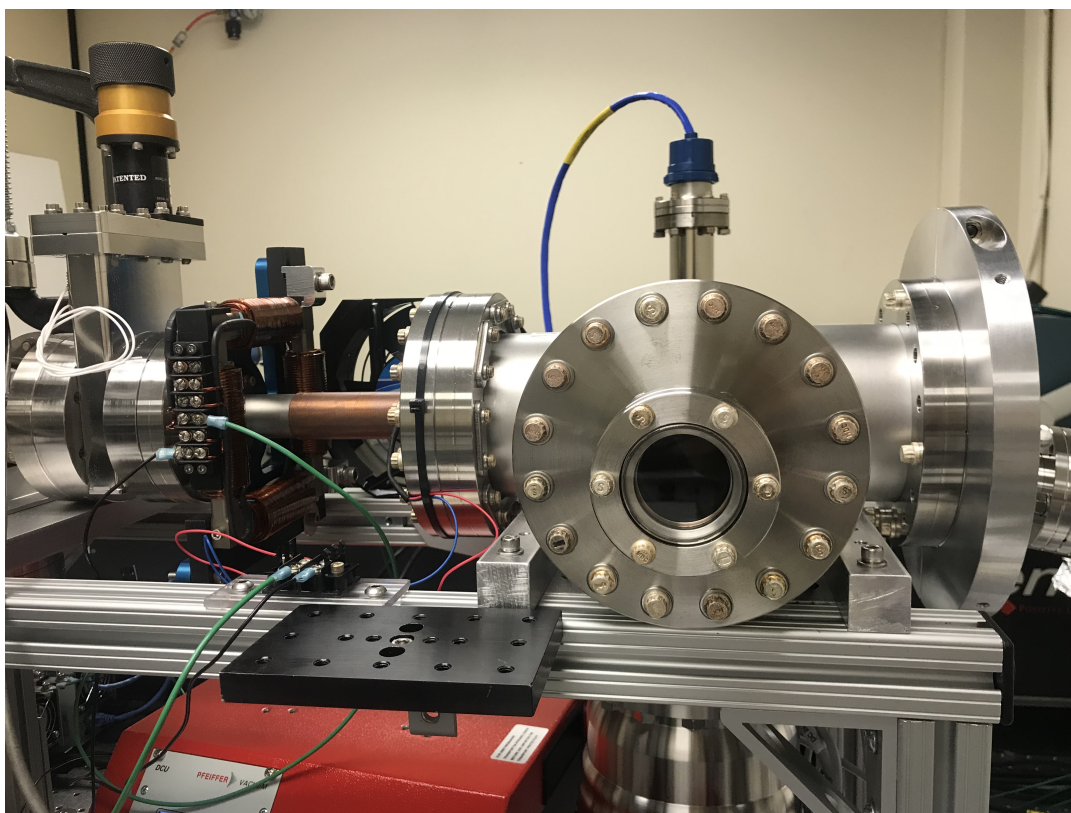


Figure 63: The photocathode is positioned inside this vacuum chamber. In blue, the electrical connection for the ion gauge pump, used to maintain UHV conditions.

The photocathode is a flat piece of copper and is connected to a high voltage supply, set to  $20\text{ kV}$ , while the anode is grounded through a direct connection to the vacuum chamber.

As already mentioned in chapter 2, the photoemission process for the extraction of electrons is based on the photoelectric effect, which can be described with tree-step model (see chapter 2). The photocathode is front illuminated by the pulsed laser and electrons should be extracted and accelerated by the DC voltage supply.

### A.3 Laser system

The laser used to illuminate the photocathode is Laser Quantum with a central wavelength of  $\lambda_0 = 800\text{ nm}$  working in mode-locke with a bandwidth extent from  $680\text{ nm}$  to  $940\text{ nm}$ , and a power of  $323\text{ mW}$ .

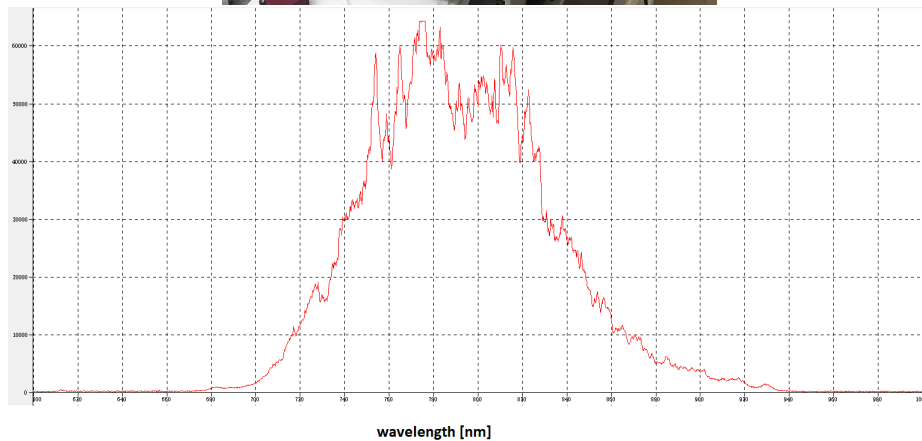
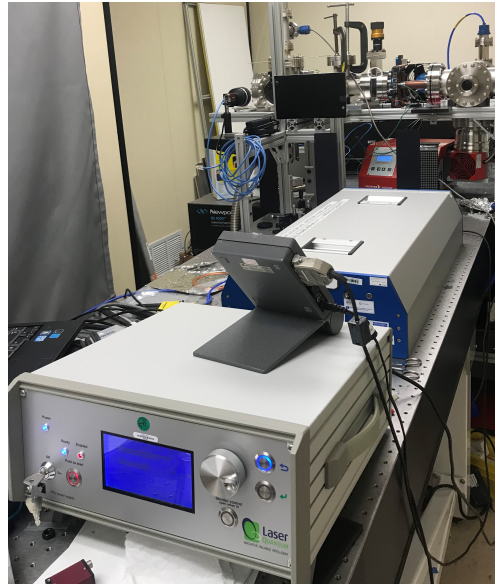


Figure 64: Top: Laser and optical table of the set-up. Bottom: spectrum of the femtosecond pulsed laser.

Integration of polarizer in the laser path must be performed to obtain a circular polarization when the spiral plasmonic lens will be tested.

### A.4 Focusing and deflection: the solenoid and the steering magnets

As it is shown in fig.63, the extracted electrons will enter inside the solenoid to be focused toward the detection chamber, since it acts as a magnetic lens. It is positioned between the electron gun and dipole magnets. To better understand this how a solenoid acts as a lens, let us focus on a

simple scheme.

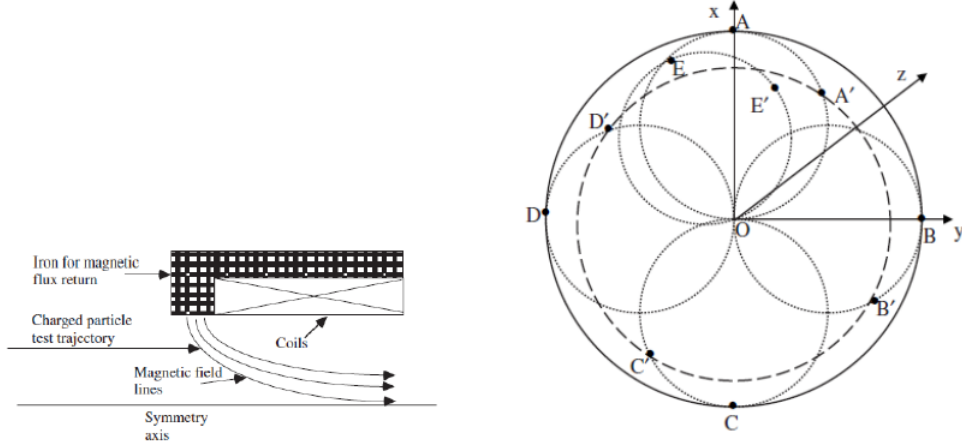


Figure 65: Left: section of the entrance of the solenoid [41]. Right: entrance of the solenoid and possible trajectories of the electron [24].

The electron will pass from a region where there is a no magnetic field to another one when the field is uniform (inside the solenoid). While it is entering, it will encounter a transition region (fig.), where a fringe field is present. Supposing that the  $z$ -axis is the propagation direction of the electron beam, along which the electron bunches are accelerated, the paraxial approximation can hold, i.e.  $p_z \gg p_\perp$  [41]. Defining  $z = 0$  at the entrance of the solenoid of length  $L$ , the magnetic field in cylindrical coordinates will be given by:

$$B_z = B_0[u(z) - u(z - L)] \quad (51)$$

$$B_\theta = 0 \quad (52)$$

$$B_r = -\frac{r}{2}B_0[\delta(z) - \delta(z - L)] \quad (53)$$

where  $u(z) = 1$  for  $z > 0$  and  $u(z) = 0$  for  $z \leq 0$ .  $B_\theta = 0$  comes from the cylindrical symmetry of the solenoid. The electrons result to have an azimuthal velocity equals:

$$\Delta v_{theta} = r_0 \frac{eB_0}{2\gamma m} = r_0 \omega_L \quad (54)$$

with  $r_0$  being the distance from the  $z$ -axis,  $e$  the elementary electron charge,  $B_0$  the magnitude of the magnetic field inside the solenoid pointing in the  $z$  direction,  $\gamma$  the Lorentz factor for relativistic particles,  $m$  the electron mass at rest and  $\omega_L$  the Lamour frequency, that is half of the cyclotron frequency. The rotation occurs in a helix with radius

$$R_c = \frac{r_0}{2} \quad (55)$$

When the electron will leave the solenoid, it will be characterized by a radial velocity and the beam will be focused. The focal length for the general case is given by:

$$\frac{1}{f} = \frac{e^2}{4\gamma^2 m^2 v_z^2} \int B^2 dz \quad (56)$$

Assuming a uniform magnetic field  $B_z$  inside the solenoid with  $N$  windings and with length  $L$  in the propagation direction, it can be written

$$B_z = \frac{\mu_0 I N}{L} \quad (57)$$

with  $\mu_0$  magnetic permeability in the vacuum and  $I$  the current passing through the solenoid. In this condition, the focal length of this magnetic lens results to be:

$$f = \frac{4L\gamma^2 m^2 v_z^2}{e^2 \mu_0^2 I^2 N^2} \quad (58)$$

Once focused, the electron bunches can be deflected changing their trajectory to reach the YAG scintillator screen and Faraday cup through the dipole magnets, positioned outside the vacuum chamber. Depending on the direction and modulus of the current, the electron beam will be deflected vertically and/or horizontally.



Figure 66: Steering magnets for the deflection of the electron trajectory.

The steering magnets consist of four coils each, disposed in two sets of parallel coils. The coils pointing in the same direction are connected in series and the resulting magnetic field in the center is used to manipulate the electron beam.

## B Lumerical

Lumerical represents a fundamental tool to simulate how the structure under investigation behaves when it interacts with electromagnetic wave. One of the possibilities Lumerical offers to solve electromagnetic problems is based on the Finite-Difference-Time-Domain (FDTD) method. It is used to solve Maxwell's equations both in time and space [42, 17], enabling to study the evolution of the electromagnetic fields in structures like the bull's eye and the spirals.

Lumerical is equipped of its own scripting language with which it possible to create and manipulate objects, together with the relative properties. Solving Maxwell's equations is performed inside the simulation box, delimited by the orange square (see fig.67), where the electromagnetic values are computed. The orange thick perimeter defines instead where the boundary conditions are applied and computed. Lumerical provides different types of boundary conditions, depending on the specific structure and analysis must be conducted. Moreover, material properties like the refractive index as a function of the wavelength and other optical paramteres are directly provided by Lumerical through the material database, based on experimental data. There is also the possibility to import new material parameters inside Lumerical domain.

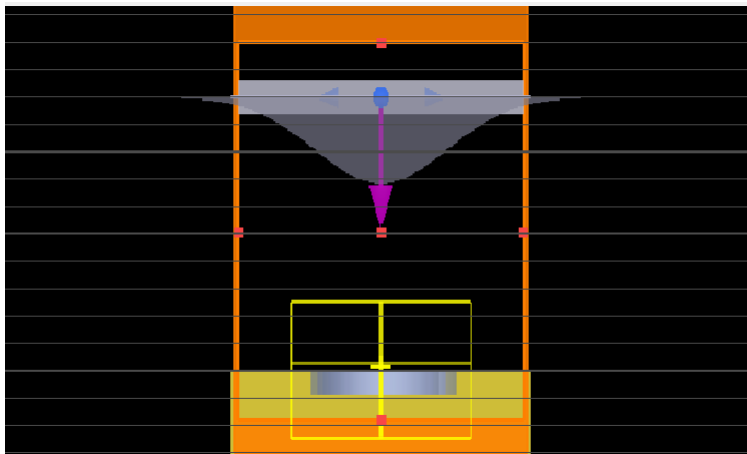


Figure 67: Example of Lumerical structure. The simulation box is defined by the orange perimeter, inside which boundary conditions are applied. The gaussian-shaped object represents the electromagnetic wave impinging on the nanostructure. The yellow square represents the a monitor.

### B.1 Spiral Script

Due to the curved nature of the spiral, the structure must be scripted through a series of geometrical approximations based on the use of primitive figures already provided by Lumerical. To be more precise, the spiral pattern is based on a piecewise polygonal approximation, where primitive rectangles are positioned one consecutive to each other, rotating with respect to the center of the pattern and going farer from that point, following a linear relation with the increasing angle  $\theta$ .

The groove are considered made of air, indicated with the material 'Etch' on Lumerical material database. The substrate is made of gold with a thickness of  $500\text{ nm}$ , and the optical properties taken from [23].

```

# add the substrate
addrect;
set("name","substrate");
set("x span",20e-6);
set("y span",20e-6);
set("z max",0);
set("z min",-0.5e-6);
set("material",metal);

# use one polygon per ring
for (i=1:n rings) {

# inner layer
# define vertex locations of polygon object
r(1:resolution/2)=linspace(start radius,start radius+thickness in+thickness out,resolution/2);
r((resolution/2+1):resolution)=linspace(start radius+thickness in*2+thickness out,start radius+thickness
in,resolution/2);
theta(1:resolution/2)=linspace(0,2*pi,resolution/2);
theta((resolution/2+1):resolution)=linspace(2*pi,0,resolution/2);
vertices(1,1:resolution)= r*cos(theta);
vertices(2,1:resolution)= r*sin(theta);

# add polygon object and set properties
addpoly;
set("name","loop A "+num2str(i));
set("vertices",vertices);
set("material",etch);
if(get("material")=="Object defined dielectric")
set("index",index in);
set("z max", 0);
set("z min",-z span);

# change start radius for next ring
start radius=start radius+thickness in+thickness out;
}

```

The resolution indicates the number of primitive rectangles used for the polygonal approximation. The matrices called  $r$  and  $theta$  are exploited to define the vertices of each rectangle. The script above refers to the reflection configuration. For what concerns the creation of the structure, the transmission configuration differs only for the definition of two substrates, one made of gold where the grooves are milled, and the other one made of  $SiO_2$  constituting the support of the plasmonic lens.

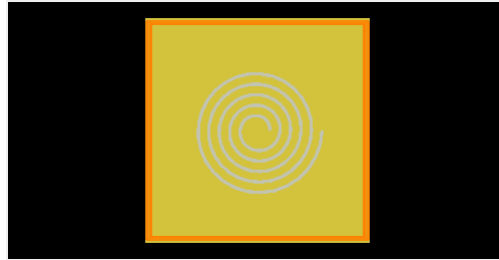


Figure 68: Spiral created with Lumerical script language.

```
#add substrate of gold
addrect;
set("name","substrate");
set("x span",20e-6);
set("y span",20e-6);
set("z max",0);
set("z min",- z span);
set("material",metal);
```

```
# add the new support of silica
addrect ;
set("name","glass");
set("x span",20e-6);
set("y span",20e-6);
set("z max",- z span);
set("z min",- z span - 5e-6);
set("material",glass);
```

Due to the asymmetric nature of the spiral, no reduction of the computational cost can be performed, like for the bull'eye structure [44], where the symmetry allows to run the FDTD simulations in a smaller region of the whole structure, without losing the any important aspects of the physics behind.

## Bibliography

- [1] E S Barnard. *Scopefoundry: A python platform for controlling custom laboratory experiments and visualizing scientific data*. 2015. URL: <http://www.scopefoundry.org/>.
- [2] C. N. Berglund and W. E. Spicer. “Photoemission studies of copper and silver: Experiment”. In: *Physical Review* 136.4A (1964). ISSN: 0031899X. DOI: 10.1103/PhysRev.136.A1044.
- [3] Christopher W. Berry, Mohammad R. Hashemi, and Mona Jarrahi. “Generation of high power pulsed terahertz radiation using a plasmonic photoconductive emitter array with logarithmic spiral antennas”. In: *Applied Physics Letters* 104.8 (2014). ISSN: 00036951. DOI: 10.1063/1.4866807.
- [4] Shirly Borukhin and Boaz Pokroy. “Formation and elimination of surface nanodefects on ultraflat metal surfaces produced by template stripping”. In: *Langmuir* 27.22 (2011), pp. 13415–13419. ISSN: 07437463. DOI: 10.1021/la203596p.
- [5] Stefano Cabrini and Satoshi Kawata. *Nanofabrication handbook*. 2012, pp. 1–504. ISBN: 9781420090536. DOI: 10.1201/b11626.
- [6] Pratik Chaturvedi et al. “Imaging of plasmonic modes of silver nanoparticles using high-resolution cathodoluminescence spectroscopy”. In: *ACS Nano* 3.10 (2009), pp. 2965–2974. ISSN: 19360851. DOI: 10.1021/nn900571z.
- [7] Cong Chen et al. “Distinguishing attosecond electron-electron scattering and screening in transition metals”. In: *Proceedings of the National Academy of Sciences of the United States of America* 114.27 (2017), E5300–E5307. ISSN: 10916490. DOI: 10.1073/pnas.1706466114.
- [8] Weibin Chen et al. “Experimental confirmation of miniature spiral plasmonic lens as a circular polarization analyzer”. In: *Nano Letters* 10.6 (2010), pp. 2075–2079. ISSN: 15306984. DOI: 10.1021/nl100340w.
- [9] Toon Coenen et al. “Cathodoluminescence microscopy: Optical imaging and spectroscopy with deep-subwavelength resolution”. In: *MRS Bulletin* 40.4 (2015), pp. 359–365. ISSN: 08837694. DOI: 10.1557/mrs.2015.64.
- [10] David H. Dowell and John F. Schmerge. “Quantum efficiency and thermal emittance of metal photocathodes”. In: *Physical Review Special Topics - Accelerators and Beams* 12.7 (2009), pp. 1–10. ISSN: 10984402. DOI: 10.1103/PhysRevSTAB.12.074201.
- [11] Lee A. DuBridge. “Theory of the energy distribution of photoelectrons”. In: *Physical Review* 43.9 (1933), pp. 727–741. ISSN: 0031899X. DOI: 10.1103/PhysRev.43.727.
- [12] Daniel B. Durham et al. “Plasmonic lenses for tunable ultrafast electron emitters at the nanoscale”. In: (2019), pp. 1–14. arXiv: 1907.02190. URL: <http://arxiv.org/abs/1907.02190>.
- [13] Innovative Epoxy and Adhesive Solutions. “Epoxy Adhesive Application Guide”. In: *Brochure* (2012), pp. 10–19. URL: [www.EPOTEK.com](http://www.EPOTEK.com).
- [14] D. Filippetto and H. Qian. “Design of a high-flux instrument for ultrafast electron diffraction and microscopy”. In: *Journal of Physics B: Atomic, Molecular and Optical Physics* 49.10 (2016), pp. 1–23. ISSN: 13616455. DOI: 10.1088/0953-4075/49/10/104003.
- [15] R.H. Fowler. “Photoelectric sensitivity”. In: *Physical Review* 38 (1931), p. 107.
- [16] F. J. García De Abajo. “Optical excitations in electron microscopy”. In: *Reviews of Modern Physics* 82.1 (2010), pp. 209–275. ISSN: 00346861. DOI: 10.1103/RevModPhys.82.209.
- [17] Stephen D. Gedney. *Introduction to the Finite-Difference Time-Domain (FDTD) method for electromagnetics*. Vol. 27. 2011, pp. 1–250. ISBN: 9781608455225.
- [18] A. E. Grigorescu et al. “10 nm lines and spaces written in HSQ, using electron beam lithography”. In: *Microelectronic Engineering* 84.5-8 (2007), pp. 822–824. ISSN: 01679317. DOI: 10.1016/j.mee.2007.01.022.

- [19] Qingrui Guo, Chi Zhang, and Xinhua Hu. “A spiral plasmonic lens with directional excitation of surface plasmons”. In: *Scientific Reports* 6 (2016), pp. 1–7. ISSN: 20452322. DOI: 10.1038/srep32345. URL: <http://dx.doi.org/10.1038/srep32345>.
- [20] Zhongyi Guo et al. “Review of the functions of archimedes’ spiral metallic nanostructures”. In: *Nanomaterials* 7.11 (2017). ISSN: 20794991. DOI: 10.3390/nano7110405.
- [21] Martin Hegner, Peter Wagner, and Giorgio Semenza. “Ultralarge atomically flat template-stripped Au surfaces for scanning probe microscopy”. In: *Surface Science* 291.1-2 (1993), pp. 39–46. ISSN: 00396028. DOI: 10.1016/0039-6028(93)91474-4.
- [22] Lumerical Solutions Inc. available online. URL: <https://www.lumerical.com>.
- [23] P.B. Johnson and R.W. Christy. “Optical-Constants Of Noble-Metals Phys. Rev. B 6(12), 4370–4379 (1972).” In: *Physical Review B* 1318.1970 (1972), pp. 4370–4379.
- [24] Vinit Kumar. “Understanding the focusing of charged particle beams in a solenoid magnetic field”. In: *American Journal of Physics* 77.8 (2009), pp. 737–741. ISSN: 0002-9505. DOI: 10.1119/1.3129242.
- [25] Yi-Chieh Lai et al. “Plasmonic Archimedean spiral modes on concentric metal ring gratings”. In: *Optics Express* 24.13 (2016), p. 15021. DOI: 10.1364/oe.24.015021.
- [26] Gilad M. Lerman, Avner Yanai, and Uriel Levy. “Demonstration of nanofocusing by the use of plasmonic lens illuminated with radially polarized light”. In: *Nano Letters* 9.5 (2009), pp. 2139–2143. ISSN: 15306984. DOI: 10.1021/nl900694r.
- [27] Jie Li et al. “Plasmonic focusing in spiral nanostructures under linearly polarized illumination”. In: *Optics Express* 22.14 (2014), p. 16686. DOI: 10.1364/oe.22.016686.
- [28] Yunfei Luo et al. “Subdiffraction nanofocusing of circularly polarized light with a plasmonic cavity lens”. In: *Journal of Materials Chemistry C* 7.19 (2019), pp. 5615–5623. ISSN: 20507526. DOI: 10.1039/c9tc00499h.
- [29] Luth. *Solid Surfaces, Interfaces and Thin Films*. ISBN: 9783319107554.
- [30] Stefan a Maier. *Fundamentals and Applications Plasmonics : Fundamentals and Applications*. Vol. 677. 1. 2004, p. 10. ISBN: 9780387331508. DOI: 10.1016/j.aca.2010.06.020. arXiv: 0405528 [cond-mat]. URL: <http://elib.tu-darmstadt.de/tocs/95069577.pdf>.
- [31] Kevin M Mcpeak et al. “Plasmonic Films Can Easily Be Better: Rules and Recipes Supporting Information 1. Characterization”. In: (). URL: [https://pubs.acs.org/doi/suppl/10.1021/ph5004237/suppl%7B%5C\\_%7Dfile/ph5004237%7B%5C\\_%7Dsi%7B%5C\\_%7D001.pdf](https://pubs.acs.org/doi/suppl/10.1021/ph5004237/suppl%7B%5C_%7Dfile/ph5004237%7B%5C_%7Dsi%7B%5C_%7D001.pdf).
- [32] Junjie Miao et al. “Plasmonic Lens with Multiple-Turn Spiral Nano-Structures”. In: *Plasmonics* 6.2 (2011), pp. 235–239. ISSN: 15571955. DOI: 10.1007/s11468-010-9193-0.
- [33] P. Musumeci et al. “Laser-induced melting of a single crystal gold sample by time-resolved ultrafast relativistic electron diffraction”. In: *Applied Physics Letters* 97.6 (2010). ISSN: 00036951. DOI: 10.1063/1.3478005.
- [34] P. Musumeci et al. “Multiphoton photoemission from a copper cathode illuminated by ultrashort laser pulses in an rf photoinjector”. In: *Physical Review Letters* 104.8 (2010). ISSN: 00319007. DOI: 10.1103/PhysRevLett.104.084801.
- [35] Robert L. Olmon et al. “Optical dielectric function of gold”. In: *Physical Review B - Condensed Matter and Materials Physics* 86.23 (2012), pp. 1–9. ISSN: 10980121. DOI: 10.1103/PhysRevB.86.235147.
- [36] Clara I. Osorio et al. “Angle-Resolved Cathodoluminescence Imaging Polarimetry”. In: *ACS Photonics* 3.1 (2016), pp. 147–154. ISSN: 23304022. DOI: 10.1021/acsp Photonics.5b00596.
- [37] P. L.E.M. Pasmans et al. “Extreme regimes of femtosecond photoemission from a copper cathode in a dc electron gun”. In: *Physical Review Accelerators and Beams* 19.10 (2016), pp. 1–12. ISSN: 24699888. DOI: 10.1103/PhysRevAccelBeams.19.103403.

- [38] A. Polyakov et al. “Plasmon-enhanced photocathode for high brightness and high repetition rate X-ray sources”. In: *Physical Review Letters* 110.7 (2013), pp. 1–5. ISSN: 00319007. DOI: 10.1103/PhysRevLett.110.076802.
- [39] A. Polyakov et al. “Plasmonic light trapping in nanostructured metal surfaces”. In: *Applied Physics Letters* 98.20 (2011), pp. 6–9. ISSN: 00036951. DOI: 10.1063/1.3592567.
- [40] Aleksandr N. Polyakov. “Plasmon Enhanced Photoemission”. In: (2012).
- [41] J. Rosenzweig. *Fundamentals of beam physics*. Vol. 41. 09. 2004, pp. 41–5351–41–5351. ISBN: 0198525540. DOI: 10.5860/choice.41-5351.
- [42] Dennis M. Sullivan. *Electromagnetic Simulation Using the FDTD Method*. 2010. DOI: 10.1109/9780470544518.
- [43] Accelerator Technology, Applied Physics Division, and Lawrence Berkeley. “Master Thesis in Nanotechnology Engineering Design and fabrication of nanoplasmonic photocathodes for ultrafast electron diffraction”. In: (2018).
- [44] Accelerator Technology, Applied Physics Division, and Lawrence Berkeley. “Master Thesis in Nanotechnology Engineering Design and fabrication of nanoplasmonic photocathodes for ultrafast electron diffraction”. In: (2018).
- [45] Politecnico Torino, Lawrence Berkeley, and Filippo Ciabattini. “Plasmonic structures for high brightness electron sources”. In: ().
- [46] Nicolas Vogel, Julius Zieleniecki, and Ingo Köper. “As flat as it gets: Ultrasoother surfaces from template-stripping procedures”. In: *Nanoscale* 4.13 (2012), pp. 3820–3832. ISSN: 20403364. DOI: 10.1039/c2nr30434a.
- [47] Emily A. Weiss et al. “Si/SiO<sub>2</sub>-templated formation of ultraflat metal surfaces on glass, polymer, and solder supports: Their use as substrates for self-assembled monolayers”. In: *Langmuir* 23.19 (2007), pp. 9686–9694. ISSN: 07437463. DOI: 10.1021/la701919r.
- [48] Qiwen Zhan. “Evanescent Bessel beam generation via surface plasmon resonance excitation by a radially polarized beam”. In: *Optics Letters* 31.11 (2006), p. 1726. ISSN: 0146-9592. DOI: 10.1364/ol.31.001726.
- [49] Baifu Zhang et al. “Chiral plasmonic lens with Archimedes-spiral distributed nanoslits”. In: *Journal of Nanophotonics* 13.02 (2019), p. 1. DOI: 10.1117/1.jnp.13.026008.
- [50] Zhiqiang Zhang et al. “Improving the adhesion of hydrogen silsesquioxane (HSQ) onto various substrates for electron-beam lithography by surface chemical modification”. In: *Microelectronic Engineering* 128 (2014), pp. 59–65. ISSN: 01679317. DOI: 10.1016/j.mee.2014.05.027. URL: <http://dx.doi.org/10.1016/j.mee.2014.05.027>.
- [51] Min Zhao et al. “Study of process of HSQ in electron beam lithography”. In: *2010 IEEE 5th International Conference on Nano/Micro Engineered and Molecular Systems, NEMS 2010* (2010), pp. 1021–1024. DOI: 10.1109/NEMS.2010.5592584.